Titre: Title:	Étude des propriétés microstructurales et rhéologiques de suspensions non-aqueuses d'argile
Auteur: Author:	Christophe Mobuchon
Date:	2008
Type:	Mémoire ou thèse / Dissertation or Thesis
Référence: Citation:	Mobuchon, C. (2008). Étude des propriétés microstructurales et rhéologiques de suspensions non-aqueuses d'argile [Thèse de doctorat, École Polytechnique de Montréal]. PolyPublie. https://publications.polymtl.ca/8123/

UNIVERSITÉ DE MONTRÉAL

ÉTUDE DES PROPRIÉTÉS MICROSTRUCTURALES ET RHÉOLOGIQUES DE SUSPENSIONS NON-AQUEUSES D'ARGILE

CHRISTOPHE MOBUCHON

DÉPARTEMENT DE GÉNIE CHIMIQUE

ÉCOLE POLYTECHNIQUE DE MONTRÉAL

THÈSE PRÉSENTÉE EN VUE DE L'OBTENTION

DU DIPLÔME DE PHILOSOPHIAE DOCTOR (Ph.D.)

(GÉNIE CHIMIQUE)

AVRIL 2008

Your file Votre référence
ISBN: 978-0-494-41755-3
Our file Notre référence
ISBN: 978-0-494-41755-3

UNIVERSITÉ DE MONTRÉAL

ÉCOLE POLYTECHNIQUE DE MONTRÉAL

Cette thèse intitulée :

ÉTUDE DES PROPRIÉTÉS MICROSTRUCTURALES ET RHÉOLOGIQUES DE SUSPENSIONS NON-AQUEUSES D'ARGILE

présentée par : MOBUCHON Christophe

en vue de l'obtention du diplôme de : Philosophiae Doctor

a été dûment acceptée par le jury d'examen constitué de :

M. FAVIS Basil D., Ph.D., président

M. CARREAU Pierre J., Ph.D., membre et directeur de recherche

Mme HEUZEY Marie-Claude, Ph.D., membre et codirectrice de recherche

M. FRADETTE Louis, Ph.D., membre

M. BOUSMINA Mosto Mostapha, Ph.D., membre

''Lire c'est bien, mais il est mieux d'aller voir''

Ella Maillart (1903-1997)

REMERCIEMENTS

Je tiens en premier lieu à exprimer toute ma gratitude envers le Professeur Pierre J. Carreau, mon directeur de recherche, et la Professeure Marie-Claude Heuzey, ma codirectrice de recherche, pour m'avoir à nouveau accueilli en toute confiance dans leur groupe de recherche. Je leur suis reconnaissant d'avoir éclairé par leur compétence, et leur gentillesse les travaux engagés. Je tiens également à les remercier pour leur patience à toute épreuve à la veille des conférences.

J'exprime mes sincères remerciements au Professeur Jan Vermant du département de Génie Chimique de l'université de Leuven sans qui une partie de ce travail n'aurait pu être concrétisée. Je remercie les étudiants de son groupe de recherche de m'avoir guidé tout au long de ma visite, et tout spécialement Naveen Krishna Reddy pour avoir donné suite aux mesures expérimentales.

Je voudrais également remercier le Professeur Gerry Fuller du département de Génie chimique de l'Université de Stanford de m'avoir encouragé sur la voie des mesures optiques, et pour son accueil lors de mon séjour à Palo Alto.

Je tiens à souligner les soutiens techniques d'Allen Glasman, spécialiste technique de la compagnie TA Instruments, lors de la mise au point des mesures oscillatoires en deux dimensions, du Dr. Nicolas Tran-Khanh et du Dr. Marc Thibault de l'Institut de Génie

Biomédical de l'École Polytechnique de Montréal pour leur expertise lors des mesures en microscopie confocale à balayage laser, du Dr. Hojatollah Vali et du Dr. Kelly Sears du département de médecine dentaire lors des mesures en microscopie électronique.

Je remercie le Professeur Mosto Mostafa Bousmina du département de Génie Chimique de L'Université Laval, et le Professeur Michael Buschmann de l'Institut de Génie Biomédical de l'École polytechnique pour m'avoir offert l'accès à leurs équipements.

Je remercie la société Rio Tito Alcan pour l'octroi d'une bourse de recherche et de la Société Européenne de Rhéologie (A.E.R.C.) et de la Society of Rheology (S.O.R.) pour l'octroi de bourses de congrès.

Je remercie également les membres du jury : le Professeur Basil Favis d'avoir accepté la présidence, et les Professeurs Mosto M. Bousmina et Louis Fradette de m'avoir fait l'honneur de passer en revue ces travaux en tant que membres du jury.

Je remercie chaleureusement Jêrome Lohézic et Emmanuel Bedo pour leur implication au projet durant leur stage de fin d'étude ainsi que les encouragements répétés de leur Professeur Gilles Ausias du laboratoire de Génie Mécanique et Matériaux de l'Université de Bretagne Sud.

Mes remerciements sont également adressés à toute l'équipe du C.R.E.PEC, de l'École Polytechnique de Montréal dont je garderai de très bons souvenirs. Je remercie tout particulièrement l'aide de Diane Héroux lors des démarches administratives, et de Mélina Hamdine lors des mesures rhéologiques, ainsi que mes amis dont notamment Karen et sa bonne humeur, Nick et les kilomètres de course à pied passés ensemble, et Mazimilano de nous avoir fait rêver au soleil d'Italie.

Je remercie ma famille de m'avoir toujours encouragé à poursuivre en recherche. Finalement, j'adresse une proche pensée à ma bien aimée, Tamara, et à tous mes anges gardiens qui ont su être là quand j'en avais besoin.

RÉSUMÉ

Les phyllosilicates ou silicates lamellaires se composent de feuillets dont les dimensions nanométriques leur confèrent des propriétés colloïdales. L'état de dispersion des nano-feuillets en suspension est alors gouverné par des forces colloïdales répulsives et attractives susceptibles de créer des structures multi-échelles. En milieu non-aqueux, la connaissance de la nature des structures en présence et de leur évolution sous écoulement suscite un intérêt grandissant depuis l'avènement des nanocomposites.

L'objectif principal de cette étude a été de relier les propriétés viscoélastiques linéaires et non linéaires de suspensions non-aqueuses de phyllosilicate à leurs propriétés structurales. Il fut posé suite à la première observation réalisée au début de cette étude. Contre toute attente, il a été constaté que les propriétés viscoélastiques linéaires et non linéaires des suspensions non-aqueuses de phyllosilicate dépendent fortement de l'histoire d'écoulement. Des techniques expérimentales inusitées ont alors été employées pour caractériser l'état de dispersion des feuillets. L'état d'orientation du phyllosilicate a été quantifié par des mesures de dichroïsme, et grâce à une nouvelle méthode non destructive reposant sur l'écoulement oscillatoire linéaire étendu en deux dimensions (2D-DAOS). La distribution spatiale à l'échelle microscopique du phyllosilicate a été suivie dans l'espace réciproque avec la diffusion de lumière en deux dimensions, et observée directement avec la microscopie confocale à balayage laser.

La première contribution notoire apportée par ces techniques est d'avoir révélé la nature microscopique et auto-similaire des structures des suspensions non-aqueuses de

phyllosilicate. La microscopie confocale à balayage laser a permis d'observer directement les microstructures et de confirmer leur nature fractale par la mesure de leur distance caractéristique à différentes fractions volumiques. Le comportement pseudo-solide des propriétés viscoélastiques linéaires de ces suspensions a donc été attribué à la présence d'un réseau d'agrégats de feuillets de nature fractale en masse.

Sous écoulement, le comportement rhéofluidifiant de ces suspensions s'explique principalement par l'évolution de la taille caractéristique de leur microstructure. Elle diminue avec la vitesse de cisaillement d'une haute à une faible valeur plateau. Cette évolution structurelle est attribuée à une agrégation réversible induite par écoulement. Elle s'accompagne d'une orientation progressive de leur microstructure dans le plan de vorticité selon la direction d'écoulement. Une fois le plateau de viscosité atteint, l'évolution de la distribution spatiale des agrégats s'accompagne d'une augmentation de l'anisotropie dans le plan du gradient de cisaillement.

Suite à un pré-cisaillement, l'absence de relaxation de l'anisotropie induite par écoulement est explicitement montrée avec des mesures de 2D-SAOS, tandis qu'aucune relaxation structurelle à l'échelle microscopique n'a été observée en microscopie confocale à balayage laser. Le comportement thixotrope de ces suspensions implique alors des réarrangements limités à l'échelle nanoscopique. Les microstructures sous écoulement persistent donc au repos sous la forme de microstructures métastables. Ces études ont permis d'éclaircir l'effet de l'histoire d'écoulement sur les propriétés viscoélastiques linéaires et non linéaires de ces suspensions.

ABSTRACT

Phyllosilicates or layered silicates consist of individual layers with nanometric dimensions. In static fluids without external forces, attractive and repulsive colloidal forces acting between the colloidal layers lead to their self-organization on multiple length scales. Under flow, a wide range of complex rheological behaviors, including shear-thinning behavior and transition from fluid-like to solid-like behavior leading to thixotropic phenomena, is expected from structural evolution. Recently, layered silicates have attracted great interest as nanoscale fillers for reinforcement of polymers (PNCs) motivating the investigation of the structural properties of non-aqueous layered silicate suspensions.

At the origin of this study, the linear and nonlinear viscoelastic properties of non-aqueous layered silicate suspensions were observed to depend on flow history. Hence, the ultimate aim of this work was to establish relationships between their rheological behavior and their structural properties. The picture of their inner structure has been achieved using a combination of light scattering techniques and advanced rheometric and microscopy measurements. The flow-induced orientation of the phyllosilicate has been quantified optically using linear dichroism measurements, and mechanically using a newly developed non-destructive method based on two-dimensional small amplitude oscillatory shear flow (2D-SAOS). The spatial distribution at the microscopic scale of the phyllosilicate has been inferred from small angle light scattering (SALS) patterns and directly observed using confocal laser microscopy (CLSM).

The combination of these techniques allowed highlighting the microscopic and self-similar nature of non-aqueous phyllosilicate suspensions. The solid-like properties of these suspensions were consequently ascribed to the presence of space-filling networks made of mass fractal clusters. Under flow, the shear-thinning behavior of these suspensions was explained by the shear rate dependency of the microstructure characteristic length scale. By increasing the shearing amplitude, the characteristic length scale of the non-equilibrium microstructures was shown to decrease from high to low plateau values. This structural evolution with the shearing amplitude was attributed to a reversible shear-induced aggregation. Limited structural orientational changes were also observed in the vorticity plane with anisotropy and orientation that developed in the same range of shear rate as the shear-thinning behavior of the suspensions. Upon cessation of flow, the lack of orientational recovery was explicitly shown with the 2D-SAOS experiments, while the lack of structural recovery at the micro-scale was observed in CLSM. The thixotropic behavior of these suspensions is therefore due to local rearrangements at the nano-scale. The non-equilibrium structures were actually shown to persist upon cessation of flow leading to different metastable structures. This work has allowed us to elucidate the effect of the flow history on the linear and nonlinear viscoelastic properties of these suspensions.

TABLE DES MATIÈRES

LISTE DES TABLEAUX

LISTE DES FIGURES

LISTE DES SYMBOLES

Alphabet latin

A	anisotropie des clichés de diffusion de lumière, amplitude de la fonction de Bessel du $m^{ième}$ degré, surface occupée par la phase dispersée des images de microscopie confocale à balayage laser
a_{eff}	taille des particules primaires à la base des agrégats de nature fractale
B	indice de loi de puissance suivie par γ^0 avec ϕ
d	diamètre d'une particule, entrefer de la géométrie en rhéométrie, dimension euclidienne
D_r	coefficient de diffusion en rotation
D_f	dimension fractale
f	fonction de structure
G	module élastique du modèle structural
G'	module de conservation
G'_i	module de conservation initial
G'_0	module de conservation aux faibles fréquences
G'_∞	module de conservation final
$G'_\parallel$	module de conservation en superposition parallèle
$G'_\perp$	module de conservation en superposition orthogonale

$G''_{\perp}$	module de perte en superposition orthogonale
G''	module de dissipation visqueuse
h	entrefer de la géométrie en rhéométrie
I	intensité en diffusion de lumière
I_{DC}	intensité continue en dichroïsme
$I_{m\omega}$	intensité de la $m^{ième}$ harmonique
J_m	fonction de Bessel du $m^{ième}$ degré
k_1, k_2, k_3, k_4	constantes cinétiques du modèle structurale
k_B	constante de Boltzmann
K_{eff}	constante d'élasticité inter-macroscopique
K_l	constante d'élasticité intra-macroscopique
K_0	constante d'élasticité entre les particules primaires à la base des agrégats de nature fractale
K_{ξ_c}	constante d'élasticité macroscopique
m	exposant de la loi de puissance suivie par ξ_0 avec $\dot{\gamma}_i$, exposant des formes exponentielles
M	masse des agrégats de nature fractale
M_0	masse des particules primaires à la base des agrégats de nature fractale
n	indice de réfraction, indice de loi de puissance suivie par G'_0 avec ϕ, indice de loi de puissance de la viscosité en régime permanent

n'	partie réelle de l'indice de réfraction
$\Delta n'$	biréfringence
n''	partie imaginaire de l'indice de réfraction
$\Delta n''$	dichroïsme
p	rapport de forme d'une particule
P	distribution de ξ
Pe, Pe_i	nombre de Péclet, nombre de Péclet lors du pré-cisaillement
q	vecteur de diffusion
r	composante en coordonnées cylindriques
t	temps, indice de loi de puissance suivie par σ^0 avec ϕ
t_{rest}	temps de relaxation suite à un pré-cisaillement
T	température, couple
T_R	rapport de Trouton
T_{ref}	température de référence pour les lois d'échelle
v	champ de vitesse, vitesse angulaire en rhéométrie rotationnelle
v_x, v_y, v_z	composantes du profil de vitesse
U	potentiel d'attraction
V	volume
w	constante du modèle structural
x, y, z	composantes en coordonnées rectangulaires
x	dimension fractal du squelette élastique des agrégats de nature fractale

z	composante en coordonnées cylindriques

Alphabet grec

α	indice de loi de puissance suivie par G' avec le rapport K_I/K_{ξ_c}
β	constante
γ	déformation en cisaillement
γ^0	déformation limite de linéarité, amplitude de déformation en cisaillement oscillatoire en deux dimensions
γ_z^0	amplitude de déformation selon z
γ_θ^0	amplitude de déformation selon θ
$\gamma_r, \gamma_\theta, \gamma_z$	déformations en coordonnées cylindriques
$\gamma_{\sigma^+_{max}}$	déformation en cisaillement au pic de contrainte
$\dot{\gamma}$	taux de cisaillement
$\dot{\gamma}_i$	taux de pré-cisaillement
$\dot{\gamma}_{ir}$	taux de pré-cisaillement de référence pour les lois d'échelle
$\dot{\gamma}_f$	taux de cisaillement final
δ	angle de déphasage
δ_z	angle de déphasage de la déformation selon z
δ_γ	angle de déphasage de la déformation
δ_θ	angle de déphasage de la déformation selon θ
ζ	facteur de glissement pour σ_0

η	viscosité en cisaillement
η_0	viscosité caractéristique du modèle structural
κ	facteur de glissement pour G'_0
λ	longueur d'onde
λ_0	temps caractéristique du modèle structural
μ	viscosité newtonienne
μ_0	viscosité limite
ξ	distance entre deux pixels d'intensités supérieures au seuil d'intensité d'une même colonne ou d'une même ligne d'une images de microscopie confocale à balayage laser, fonction de structure, paramètre de structure du modèle structure
ξ_c	taille moyenne des agrégats
ξ_l	paramètre de structure du modèle structural aux l'échelles inférieures au micron
ξ_m	paramètre de structure du modèle structural à l'échelle macroscopique
ξ_0	dimension moyenne de la corrélation spatiale des images en microscopie confocale à balayage laser
σ	contrainte
σ^-	contrainte transitoire lors d'une augmentation de $\dot{\gamma}$
σ^+	contrainte transitoire lors d'une diminution de $\dot{\gamma}$

σ_{∞}^{+}	contrainte à l'équilibre en régime transitoire
σ_e	contribution élastique à la contrainte
σ_0	seuil de contrainte
σ_v	contribution visqueuse à la contrainte
σ_z	contrainte selon z
σ_θ	contrainte selon θ
τ, τ_1, τ_2	temps caractéristiques
ϕ	fraction volumique
ϕ_g	fraction volumique à la transition vitreuse
ϕ_{ref}	fraction volumique de référence pour les lois d'échelle
$\phi_{z\theta}$	angle de la déformation oscillatoire dans le plan (z,θ)
χ	angle d'orientation du dichroïsme
ω	fréquence de la pulsation

CHAPITRE 1 - CONCEPTS ET REVUE DE LA LITTÉRATURE

1.1. Introduction et objectif de l'étude

Les phyllosilicates ou silicates lamellaires sont formés de feuillets d'argile d'une épaisseur de l'ordre du nanomètre (Grim 1968, Rossman et Carel 2002). Ils sont couramment utilisés comme additifs lors de la formulation de nombreuses suspensions industrielles, telles que les produits céramiques, les peintures, les encres, les émulsions, et les fluides de forage (Jones 1983, Patel *et al.* 2006). Ils représentent un élément-clé dans le contrôle de leur comportement rhéologique en leur conférant, entre autres, un caractère thixotrope accompagné d'un seuil de contrainte.

Plus récemment, leur potentiel en tant que charge pour la préparation de nano-composites de polymères a suscité un intérêt considérable depuis qu'Okada *et al.* (1997) leurs ont attribué des propriétés remarquables comparées à celles des macro-composites de polymères conventionnels. Les nano-composites contenant de faibles fractions massiques de phyllosilicates ($\leq$ 5 wt. %) se distinguent de leur matrice de polymère par une amélioration de la plupart de leurs propriétés telles que leurs résistances mécaniques, aux solvants, aux chocs thermiques, au feu, ainsi que des propriétés barrières améliorées, et une plus grande stabilité dimensionnelle (Ray et Okamoto 2003).

Les propriétés des suspensions et des nanocomposites de phyllosilicates sont intimement liées à l'état de dispersion de leurs feuillets. En milieu non-aqueux, la

dispersion des feuillets sous-entend une modification organophile de leur surface naturellement hydrophile. Selon l'affinité entre la matrice et le phyllosilicate qui en résulte, trois échelles de dispersion sont communément distinguées. L'absence d'interactions favorables entre la matrice et le phyllosilicate se traduit par la présence d'agglomérats à l'échelle macroscopique. Une diffusion limitée de la matrice entre les feuillets préserve leur cohésion à l'échelle d'une dizaine de feuillets. Finalement, une dispersion à l'échelle nanoscopique est atteinte lorsque la diffusion de la matrice est telle, que les nano-feuillets sont exfoliés, c.-à-d. dispersés individuellement. Les propriétés les plus remarquables sont attendues lors de l'exfoliation qui maximise les surfaces interfaciales. L'interprétation des propriétés des suspensions et des nanocomposites de phyllosilicates reposent le plus souvent sur cette seule description de l'état de dispersion qui se limite à considérer la seule distance moyenne entre les feuillets. Une représentation complète de l'état de dispersion des feuillets doit inclure leur distribution spatiale et d'orientation. Afin d'appréhender leur éventuelle organisation multi-échelle, elle doit être étendue de l'échelle nanoscopique à l'échelle macroscopique, et ainsi aboutir à une description fidèle de la structure formée par les nano-feuillets argileux.

L'objectif principal de ce travail a été de corréler le comportement rhéologique de suspensions non-aqueuses de phyllosilicates à l'état de dispersion de leurs feuillets. Dans un premier temps, l'étude minutieuse de leurs propriétés viscoélastiques linéaires et non-linéaires a permis de mettre en évidence le rôle crucial joué par l'histoire d'écoulement sur l'état de dispersion des feuillets. Suite à un écoulement de

cisaillement, il est montré que les suspensions non-aqueuses de phyllosilicates atteignent différentes structures métastables selon l'amplitude du pré-cisaillement. La nature et l'origine des structures métastables sont ensuite établies grâce à des techniques inédites de mesure de leur anisotropie et de la distribution spatiale de leurs feuillets.

Dans ce premier chapitre, la structure cristallographique et les propriétés des phyllosilicates sont tout d'abord présentées. Elles permettront de mieux distinguer leurs spécificités et d'appréhender la problématique de leur dispersion en milieu non-aqueux. Une vue d'ensemble des connaissances actuelles du comportement rhéologique des suspensions non-aqueuses de phyllosilicates est ensuite donnée afin d'appuyer la pertinence des travaux engagés. Ils sont présentés sous la forme de trois articles (en anglais). Le premier article dresse le portrait rhéologique d'une suspension non-aqueuse et non-polaire de phyllosilicate organophile. Il met en évidence le rôle primordial joué par l'histoire d'écoulement sur les propriétés viscoélastiques linéaires et non linéaires. Le second et le troisième articles s'attachent ensuite à établir l'origine de l'influence de l'histoire d'écoulement en reliant les propriétés rhéologiques de suspensions de phyllosilicate à leurs propriétés structurales.

1.2. Structures et propriétés des phyllosilicates

Les phyllosilicates privilégiés pour la réalisation de suspensions et de nanocomposites appartiennent au groupe des smectites. La montmorillonite, l'hectorite et la saponite sont les smectites les plus couramment employées. L'attrait de ces phyllosilicates

réside dans leur aptitude au gonflement, c.-à-d. à la séparation des feuillets, conférée par leur structure cristallographique. La structure et les propriétés de cette famille de minéraux sont présentées par la suite.

1.2.1. Structures cristallographiques

Comme le nom l'indique, les phyllosilicates (du grec, phyllon, une feuille) ou silicates lamellaires sont des silicates dont leurs motifs élémentaires tétraédriques $[SiO_4]^{4-}$ (Figure 1.1a) forment des feuillets élémentaires $[Si_2O_5]^{2-}$ (Figure 1.2). Ces feuillets élémentaires tétraédriques se condensent avec des octaèdres d'oxydes métalliques (Figure 1.1b) et forment ainsi des feuillets dans un rapport 1:1, c.-à-d. un feuillet élémentaire de tétraèdres de silice condensé avec un feuillet élémentaire d'octaèdres d'oxyde métallique, 2:1 ou 2:1:1, c.-à-d. un feuillet élémentaire octaédrique adjacent à un feuillet 2:1 (Figure 1.3) (Grim 1968, Rossman et Carel 2002). Lors de ces condensations, les atomes d'oxygènes octaédriques non partagés avec les feuillets élémentaires tétraédriques deviennent des groupes hydroxyles. Ces atomes ont en effet pour seuls ligands les cations octaédriques qui ne les équilibrent pas. Ils ont alors en moyenne une déficience en charge d'un électron qui se voit compenser avec l'atome d'hydrogène. Les phyllosilicates 1:1 ont donc à la surface d'une des deux faces de leurs feuillets des groupes hydroxyles. Ces groupes hydroxyles vont lier fortement les feuillets 1:1 entre eux via des liaisons hydrogènes avec les atomes d'oxygènes des feuillets élémentaires tétraédriques d'une face adjacente.

Les phyllosilicates 1:1 et 2:1 se distinguent par l'occupation de leurs sites octaédriques. Contrairement aux sites tétraédriques, tous les sites octaédriques ne sont pas forcément occupés. Les phyllosilicates sont dits dioctaédriques lorsque deux de leurs sites octaédriques sur trois sont occupés et trioctaédriques lorsque tous leurs sites sont occupés. Les phyllosilicates 2:1:1 ne présentent pas cette particularité. Les cations présents dans les sites octaédriques comme ceux des sites tétraédriques donnent lieu à des substitutions isomorphes. Les atomes de silicium des couches tétraédriques peuvent être remplacés par exemple par des ions Al^{3+}. De la même façon, les atomes métalliques des couches octaédriques peuvent être remplacés par des ions de valence inférieure. Il en résulte pour les phyllosilicates 2:1 un déficit de charge compensé par la présence entre les feuillets de cations, c.-à-d. d'ions compensateurs, qui permettent de contrebalancer la charge négative des feuillets. Les ions compensateurs de ces phyllosilicates possédant leur substitution isomorphe dans la couche octaédrique sont moins fortement liés aux feuillets et plus facilement hydratables. L'effet du déficit de charge est en effet écranté par la couche tétraédrique, ce qui confère à ces phyllosilicates des interactions interfoliaires plus faibles. Les substitutions isomorphes se produisant dans les phyllosilicates 1:1 ne donnent quant à eux pas de déficit de charge. Aucun ion compensateur ne vient alors séparer les feuillets fortement liés par des liaisons hydrogènes. Seuls les phyllosilicates 2:1 vont alors être en mesure de présenter des propriétés de gonflement.

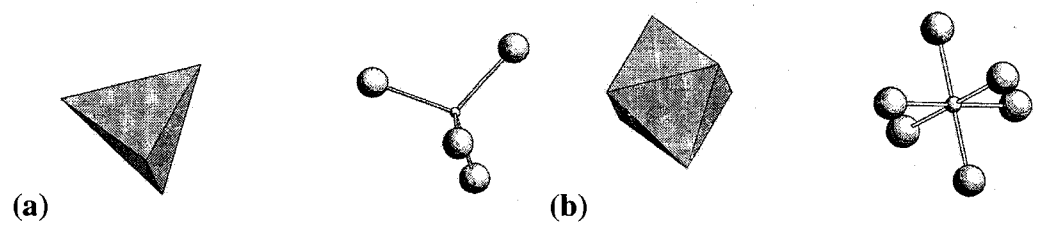

Figure 1.1 : Tétraèdre (a) et octaèdre (b) et leur arrangement atomique correspondant à la base de la structure des silicates (Rossman et Carel 2002).

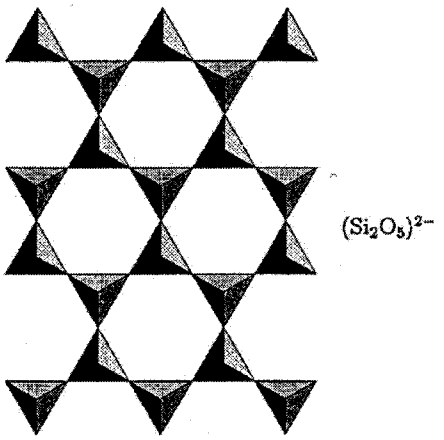

Figure 1.2 : Structure hexagonale en feuillet élémentaire des phyllosilicates (Rossman et Carel 2002).

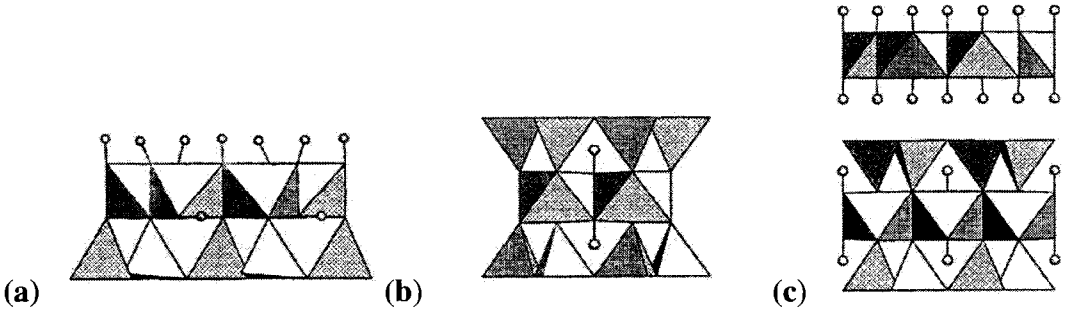

Figure 1.3 : Vues latérales des structures majeures des phyllosilicates : 1:1 (a), 2:1 (b), 2:1:1 (c); Les cercles représentent la position des groupes hydroxyles (Rossman et Carel 2002).

Le Tableau 1.1 (Le Pluart 2002) présente une synthèse appliquée aux phyllosilicates 2:1 des classifications proposées par le comité international de Classification et de Nomenclature des Minéraux argileux en 1966 et par Mering et Pedro (1969). Elles reposent sur la structure du feuillet, la charge du feuillet, le nombre d'atomes métalliques en couche octaédrique, la localisation des substitutions et le type de cations compensateurs. Il apparaît que les propriétés, c.-à-d. la charge des feuillets et la localisation des substitutions, de la montmorillonite et de l'hectorite, qui appartiennent au groupe des smectites, sont telles qu'ils possèdent les propriétés de gonflement les plus intéressantes de tous les minéraux de la famille des phyllosilicates. L'emploi de ces smectites est donc privilégié pour la réalisation de suspensions et de nanocomposites.

À noter que dans la littérature la plus ancienne, le terme montmorillonite est fréquemment utilisé comme nom de groupe pour tous les phyllosilicates 2:1 qui possèdent une aptitude au gonflement. Actuellement, le terme smectite est le nom du groupe et la montmorillonite désigne un minéral qui en fait parti. De plus, pour éviter toute confusion, la plupart des minéraux doivent être désignés non seulement par leur nom, mais aussi par leur composition chimique. Par exemple, la montmorillonite peut avoir pour composition les formules suivantes : $[SiO_{10}Al^{3+}_{(2-x)}Mg^{2+}_{x}(OH)_2]$ ou

$[SiO_{10}Al^{3+}_{(2-x)}Ca^{2+}_{x}(OH)_2]$ du fait de substitutions isomorphes avec des cations compensateurs différents dans la couche d'oxyde d'aluminium.

1.2.2. Microstructure

La texture et la morphologie des smectites ne sont pas uniformes. La montmorillonite se présente sous la forme de particules souples, anisotropes, d'une longueur comprise entre 320 et 400 nm (Cadene *et al.* 2005) alors que les dimensions des particules de saponite n'excèdent par les 60 nm. Ils ont tous la particularité de présenter différents niveaux d'organisation selon l'échelle d'observation (Figure 1.4).

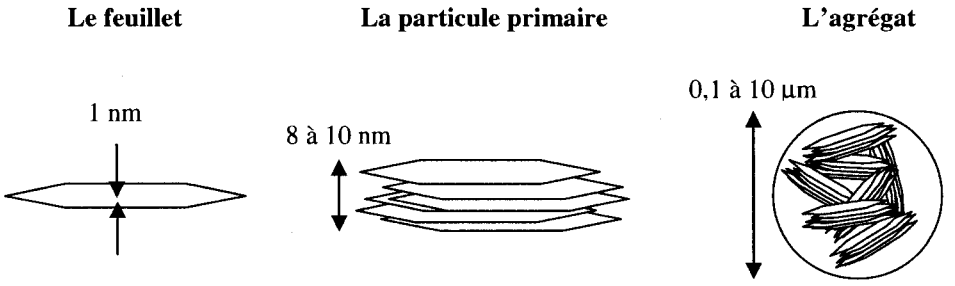

Figure 1.4 : Structures multi-échelles de la montmorillonite.

À la plus petite échelle, on distingue le feuillet tel que défini au paragraphe 1.2.1 d'une épaisseur de l'ordre du nanomètre. Une dizaine de feuillets empilés les uns sur les autres composent une particule primaire. Les feuillets d'une particule primaire sont maintenus entre eux par les forces électrostatiques attractives qu'ils développent avec leurs ions compensateurs. La distance entre les surfaces en regard de deux feuillets est appelée distance interfoliaire. À noter que l'arrangement global des feuillets, au sein d'une particule primaire de montmorillonite, est particulier. Il est dit turbostratique car

il présente un désordre dans le plan parallèle aux surfaces principales des feuillets. Ce désordre est dû aux substitutions isomorphes de type dioctaédrique de la montmorillonite (Tableau 1.1). Cette localisation des substitutions empêche en effet les cavités hexagonales (Figure 1.2) de deux feuillets adjacents de se superposer. Plus généralement, les smectites, et tout particulièrement la montmorillonite, et les vermiculites ne présentent pas une structure cristallographique bien ordonnée dans les trois directions contrairement aux micas, talc et pyrophilite. Finalement, un ensemble de particules primaires orientées dans toutes les directions forment un agrégat de taille variant de 0,1 à 10 microns.

Tableau 1.1 : Classification des phyllosilicates 2:1 (Le Pluart 2002).

Charge des feuillets	Groupe	Sous groupe	Nom	Occupation de la couche octaédrique	Localisation des substitutions	Cations compensateurs
x > 0,6	Mica dur x ≈ 2	-	Margarite	2	Tétraèdres	Ca^{2+} anhydre
			Clintonite	3		
	Mica x ≈ 1	-	Muscovite Illite	2		K^+ anhydre
			Phlogopite Biotite	3		
	Vermiculite 0,9 < x < 0,6	-	Vermiculite dioctaédrique	2		Mg^{2+}, Na^+, Ca^{2+} hydratés
			Vermiculate trioctaédrique	3		
x > 0,25	Smectite	Saponite	Saponite	3	Tétraèdres	Mg^{2+}, Na^+, Ca^{2+}, K^+ hydratés
			Hectorite	3	Octaèdres	
		Montmo-rillonite	Montmorillonite	2	Octaèdres	
			Beidellite	2	Tétraèdres	
x = 0	Pyrophylite Talc	-	Pyrophyllite	2	Aucune substitution	Aucun
			Talc	3		
			Minnesotaite			

1.2.3. Synthèse

Les phyllosilicates se distinguent par leur structure cristallographique en feuillets d'une épaisseur de l'ordre du nanomètre. Grâce aux faibles charges de leurs feuillets et à la localisation interne de leurs substitutions isomorphes, les feuillets des phyllosilicates appartenant à la famille des smectites sont séparés par des cations compensateurs permettent leur dispersion individuelle en milieu aqueux. La présence de groupes hydroxyles au sein de leurs feuillets confère en effet à leur surface une nature hydrophile.

Les pré-requis à l'exfoliation en milieu non-aqueux des phyllosilicates sont présentés et justifiés d'un point de vu thermodynamique à la section suivante.

1.3. Dispersion des phyllosilicates en milieu organique

L'idée fondamentale pour l'exfoliation des phyllosilicates en milieu non-aqueux repose sur l'intercalation, c.-à-d. la diffusion, de la matrice entre les galeries interfoliaires. L'affinité entre la matrice et le phyllosilicate joue alors un rôle crucial. Elle est le plus souvent contrôlée grâce à une modification organophile de la surface hydrophile des phyllosilicates. La méthode la plus courante de modification organophile est ici décrite brièvement et son rôle lors de l'exfoliation expliquée à partir du modèle thermodynamique de Vaia et Giannelis (1997).

1.3.1. Modifications organophiles des phyllosilicates

La méthode de modification organophile des phyllosilicates la plus couramment mise en œuvre est l'échange cationique. D'autres méthodes originales ont été développées, comme le greffage d'organosilanes et l'utilisation d'ionomères ou de copolymères à bloc (Le Pluart 2002).

L'échange cationique consiste à substituer les cations compensateurs des phyllosilicates par des cations porteurs d'une chaîne alkyle. Les cations les plus fréquemment utilisés sont les ions alkylammonium. Ils confèrent non seulement un caractère organophile aux phyllosilicates, mais augmentent également leur distance interfoliaire entre 1 et 5 nm ce qui facilite l'intercalation de la matrice organique (Lagaly 1986). De plus, ils peuvent fournir des groupes fonctionnels capables de réagir avec la matrice et même d'initier la polymérisation d'un monomère intercalé (Kojima *et al.* 1993). La longueur de la chaîne carbonée, les groupements organiques ainsi que la taille et la forme de la tête polaire du cation porteur de la chaîne alkyle, ont des influences non négligeables sur l'efficacité de l'échange, tout comme la nature du phyllosilicate. La quantité d'ions alkylammonium adsorbée augmente en effet avec la densité de charges du phyllosilicate (Tableau 1.1). Cependant dans le cas des micas, elle s'accompagne d'une forte interaction avec les feuillets et diminue par conséquent leur aptitude à l'échange cationique. Un échange cationique trop important peut également être contraignant pour la diffusion de la matrice comme c'est le cas avec les vermiculites. La diffusion du composé organique dans les galeries est en effet limitée

par un encombrement stérique trop important (Lan *et al.* 1995). Les smectites présentent encore le meilleur compromis et sont donc les phyllosilicates de prédilection pour la réalisation de suspensions et de nanocomposites. Leur aptitude à l'échange cationique est quantifiée par leur capacité d'échange cationique (CEC). Elle désigne le nombre de cations monovalents qu'il est possible de substituer aux cations compensateurs pour compenser la charge négative de 100 grammes d'argile. Elle s'exprime généralement en milliéquivalents pour 100 gramme (meq/100g; 1 meq = 96,5 Coulomb).

1.3.2. Approche thermodynamique de l'intercalation

Le modèle thermodynamique de Vaia et Giannelis (1997) décrit l'intercalation des polymères fondus entre les feuillets des phyllosilicates modifiés avec des chaînes aliphatiques et vise à prédire si l'intercalation est envisageable, et le cas échéant si elle doit résulter ou non en leur exfoliation. Il repose sur la thermodynamique statistique à l'image des travaux de Flory (1953) sur les mélanges de polymères. Selon ce modèle, la variation entropique défavorable associée au confinement des chaînes, et la variation enthalpique défavorable liée à la séparation des feuillets sont en partie compensée par l'augmentation des arrangements conformationnels des chaînes aliphatiques liée à l'augmentation de la distance interfoliaire induite par l'intercalation. La variation entropique favorable associée aux chaînes aliphatiques augmente tant que la distance interfoliaire est inférieure à leur longueur. À noter que la contribution entropique défavorable liée au confinement de la matrice diminue avec son poids moléculaire pour

finalement être négligeable dans le cas d'un solvant. Au-delà, la force motrice de l'intercalation est attendue de la part de variations enthalpiques. Pour des phyllosilicates modifiés par des ions alkylammonium, une variation enthalpique favorable est accentuée en maximisant l'intensité et le nombre d'interactions entre la matrice organique et les chaînes aliphatiques tout en minimisant les interactions non polaires entre la matrice et l'argile. Par ailleurs, des interactions favorables importantes entre la matrice et l'argile ou entre la matrice et les chaînes aliphatiques peuvent conduire à ce que les chaînes de la matrice lient les deux surfaces en regard de l'argile (Balazs *et al.* 1998, Balazs *et al.* 1999, Zhulina *et al.* 1999). Pour une telle situation, l'exfoliation n'est plus envisageable.

1.3.3. Synthèse

L'exfoliation des phyllosilicates en milieu non-aqueux repose sur la diffusion de la matrice organique entre les galeries interfoliaires, et requiert alors une modification organophile de leur surface hydrophile. La modification organophile la plus courante repose sur la substitution des cations compensateurs de l'argile par des cations porteurs d'une chaine aliphatique telle que les ions alkylammonium.

Selon le modèle thermodynamique de Vaia et Giannelis (1997), le rôle joué par le modifiant organique lors de l'exfoliation de l'argile est double. L'augmentation des arrangements conformationnels de ses chaines apporte dans un premier temps une contribution entropique favorable qui compense celle défavorable liée au confinement de la matrice, ainsi que celle enthalpique induite par la séparation des feuillets. En

compatibilisant le polymère et l'argile, il assure également une variation enthalpique favorable à l'exfoliation.

1.4. Comportement rhéologique des suspensions non-aqueuses de phyllosilicates

La connaissance du comportement rhéologique des suspensions de phyllosilicates au regard de leur état de dispersion est indispensable pour établir leur domaine d'application. Elle est de même primordiale dans le cas des nanocomposites polymère/phyllosilicate à l'état fondu afin de maîtriser leur mise en forme, et de-là leurs propriétés finales. L'exposé suivant du comportement viscoélastique linéaire et non linéaire de ces systèmes s'attache tout particulièrement à relever l'expression de l'état de dispersion de leurs feuillets. Il présente les singularités observées à ce jour de leur comportement rhéologique par rapport aux systèmes composites macroscopiques. Il reporte essentiellement les résultats rhéologiques d'études sur les nanocomposites polymère/phyllosilicate à l'état fondu. Un nombre restreint d'études du comportement rhéologique des phyllosilicates organophiles en suspension dans un solvant organique a été à ce jour publié (Jin et James 2006, King *et al.* 2007, Zhong et Wang 2003).

La nature colloïdales des phyllosilicates est tout d'abord discutée afin d'éclaircir les résultats rhéologiques présentés.

1.4.1. Nature colloïdale des phyllosilicates

Les particules colloïdales regroupent les particules dont leurs dimensions sont comprises entre le nanomètre et le micromètre (van de Ven 1989). Les feuillets des phyllosilicates sont alors de nature colloïdale de part leurs dimensions nanométriques. À ces échelles, la dispersion individuelle des particules s'accompagne de la création de surfaces interfaciales considérables, et les particules se voient soumises à des forces négligeables aux échelles macroscopiques. Pour les phyllosilicates, leur exfoliation peut conduire à la création de surfaces interfaciales de l'ordre des $700m^2/cm^3$, au regard de celles créées par les macrocomposites traditionnels, de l'ordre du cm^2/cm^3 (Krishnamoorti et Vaia 2002). En suspension dans un milieu non aqueux, l'état de dispersion des feuillets à l'équilibre est gouverné par des forces attractives et répulsives telles que le forces Browniennes, les force d'attraction de Van der Waals, les forces de répulsion liées à leur volume exclu, et éventuellement des forces induites par la présence de polymères. À noter que les forces répulsives électrostatiques sont négligeables en milieu non-aqueux. Les forces attractives de Van der Waals résultent d'interactions dipolaires et sont responsables de l'agrégation des feuillets. Son potentiel, quantifié par la constante d'Hamaker, est de courte portée, et excède les forces Browniennes pour des distances interparticulaires de l'ordre du nanomètre. Son amplitude dépend en grande partie de la différence entre l'indice de réfraction de la matrice et celui du phyllosilicate (Philipse et Vrij 1989). Le mouvement Brownien quant à lui tend à disperser aléatoirement les feuillets. Il est quantifié par des

coefficients de diffusion en rotation et en translation. Le coefficient de diffusion en rotation, D_r, se définit de la façon suivante : $D_r = 3k_BT/4\eta d^3$ avec k_B la constante de Bolztmann, T la température absolue, η la viscosité de la matrice, et d le diamètre des feuillets. Finalement, le volume exclu important des feuillets des phyllosilicates restreint leur mobilité à des faibles fractions volumiques. Par exemple, la distance moyenne entre les feuillets assimilés à des disques de 1.2 nm d'épaisseur approche les 30 nm à une fraction volumique de 4 % alors que leurs dimensions latérales est voisine de la centaine de nanomètres. Il peut alors conduire à la formation de mésophases, et plus particulièrement de phases nématiques au-delà d'une concentration critique de phyllosilicate. Au-delà de cette concentration critique, les interactions entre les volumes exclus des feuillets leur imposent une orientation commune.

Lyatskaya et Balazs (1998) ont modifié la théorie d'Onsager (1949) pour prédire la formation de phases nématiques. Ils ont ainsi adopté la forme générale de l'énergie libre proposée par Onsager pour des bâtonnets en l'adaptant pour prendre en compte la géométrie en forme de disque des phyllosilicates. Ils ont ainsi montré que les systèmes composés de disques maintiennent leur orientation isotrope à des concentrations supérieures que les systèmes composés de bâtonnets et que l'étendue de cette phase isotrope diminue rapidement avec le rapport de forme des disques. Koo *et al.* (2002) ont bien observé expérimentalement pour leur nanocomposites une transition d'une phase isotrope à une phase nématique au-delà d'une concentration volumique de 9 %. Ginzburg et Balazs (1999) ont étendu l'analyse de Lyatskaya et Balazs (1998) en considérant comme nouvelle variable d'état la fonction de distribution de densité des

disques en plus de la fonction de distribution d'orientation. Elle leur a permis de décrire plus finement la formation des mésophases en distinguant les phases smectiques et cristallines qui en plus d'une orientation privilégiée des particules sous entendent un arrangement spatial. Ces phases supplémentaires sont induites par l'anisotropie des interactions entre les particules qui est prise en compte dans leur modèle. Ils ajoutent également l'entropie en translation du polymère à l'expression de l'énergie libre via l'expression donnée par Flory-Huggins. L'entropie conformationnelle du polymère fut ajoutée par la suite par les mêmes auteurs (Ginzburg *et al.* 2000). L'énergie libre conformationnelle qui en résulte peut être interprétée comme l'interaction effective entre les particules d'argile. Les auteurs choisissent une approche numérique selon la méthode du champ moyen autoconsistant (self-consistent field theory) pour la calculer. Elle leur permet de prendre en compte l'influence de la modification de l'argile via des chaînes aliphatiques et de conjuguer à la fois les attentes à l'échelle nanoscopique, en distinguant une morphologie intercalée d'une morphologie exfoliée, et à l'échelle microscopique, en prédisant les phases isotrope, nématique et smectique des nanocomposites. Ils ont ainsi démontré les rôles déterminants joués par la longueur des chaînes aliphatiques, et l'énergie d'interaction entre le polymère et les chaînes aliphatiques sur la morphologie finale du mélange. L'attraction entre les particules d'argile diminue avec la longueur des chaînes aliphatiques et une densité excessive de ces chaînes peut empêcher l'intercalation du polymère. La prise en compte de la forte anisotropie des feuillets et de leurs interactions a permit à Balazs *et al.* (1998, 1999)

d'établir des diagrammes de phases qui prédisent la formation de phases nématiques et smectiques.

Les modèles thermodynamiques précédents renseignent sur le comportement de phase à l'équilibre. Ils ne peuvent prédirent la formation de structures sous écoulement et les structures métastables qui s'ensuivent au repos. Sous écoulement, la compétition entre les forces hydrodynamiques et les forces thermodynamiques dicte les structures hors équilibre (Russel 1987, Russel *et al.* 1989, van de Ven 1989), et ainsi le comportement rhéologique de ces suspensions. Les propriétés viscoélastiques linéaires et non linéaires des suspensions de phyllosilicates sont passées en revue à la prochaine section.

1.4.2. Propriétés viscoélastiques linéaires

Le comportement viscoélastique linéaire d'un grand nombre de nanocomposites à base de polymères fondus, incluant : poly(ε-caprolactone) (PCL) (Di *et al.* 2003, Hoffmann *et al.* 2000b, Krishnamoorti et Giannelis 1997, 2001, Kwak et Oh 2003, Maiti 2003), polyamide (Fornes *et al.* 2002), polystyrène (PS) (Hoffmann *et al.* 2000a, Lim et Park 2000, 2001, Meincke *et al.* 2003, Ren *et al.* 2003), copolymère polystyrène-polyisoprène (Krishnamoorti *et al.* 2001, Mitchell et Krishnamoorti 2002, Ren *et al.* 2000), polypropylène (PP) (Galgali *et al.* 2001, Koo *et al.* 2003, Li *et al.* 2003, Solomon *et al.* 2001), polyéthylène (PE) (Wang *et al.* 2002) et poly(butylène succinate) (Ray *et al.* 2003), et de solvant organiques (King *et al.* 2007, Li *et al.* 2003, Zhong et Wang 2003) ont été publiés à ce jour. L'observation la plus remarquable de l'ensemble de ces études est la faible dépendance en fréquence de leurs modules viscoélastiques

aux faibles fréquences. Ce comportement pseudo-solide fut reporté pour la première fois par Krishnamoorti *et al.* (1997) pour un nanocomposite exfolié PCL/montmorillonite. La transition d'un comportement liquide, c.-à-d. $G' \propto \omega^2$ et $G'' \propto \omega^1$, vers un comportement solide, c.-à-d. G' et $G'' \propto \omega^0$, est observée à des fractions volumiques de silicate lamellaire faibles inférieures à 5 % (Koo *et al.* 2003, Krishnamoorti et Giannelis 1997, Li *et al.* 2003, Lim et Park 2001, Meincke *et al.* 2003, Ren *et al.* 2000). Elle débute pour le module élastique à la même fréquence quelque soit la concentration de silicate lamellaire, tandis que pour le module visqueux, elle débute à des fréquences qui augmentent avec la concentration (Aubry *et al.* 2005, Ayyer et Leonov 2004). Le comportement pseudo-solide est exhibé à la fois par des suspensions supposées exfoliées (Hoffmann *et al.* 2000a, Koo *et al.* 2003, Krishnamoorti et Giannelis 1997, Li *et al.* 2003, Lim et Park 2001, Meincke *et al.* 2003, Wang *et al.* 2002) et intercalées (Galgali *et al.* 2001, Lim et Park 2001, Ren *et al.* 2000, Solomon *et al.* 2001). Il semble pour les nanocomposites intercalés d'autant plus prononcé que l'affinité entre le polymère et l'argile est grande. Lim *et al.* (2001) ont en effet mesuré un comportement pseudo-solide aux faibles fréquences plus marqué pour leurs nanocomposites à base d'un copolymère aléatoire polystyrène/anhydride maléique que pour leurs nanocomposites à base d'un simple polystyrène. Cependant, bien que l'intercalation de leurs deux nanocomposites soit similaire selon leurs clichés de diffraction des rayons X, une telle conclusion doit être relativisée sachant qu'une dispersion plus homogène de l'argile est observée par microscopie électronique en transmission pour leur nanocomposite à base de leur copolymère.

Une hypothèse avancée pour expliquer ce comportement pseudo-solide dans le cas des nanocomposites repose sur le confinement des chaînes polymériques. La viscosité d'un polymère augmente en effet avec son confinement qui limite la mobilité de ses chaînes. L'indifférence de l'énergie d'activation des nanocomposites avec la fraction volumique d'argile suggère d'écarter cette première hypothèse (Galgali *et al.* 2001, Kotsilkova 2002, Krishnamoorti et Giannelis 1997, Meincke *et al.* 2003, Ren *et al.* 2000, Solomon *et al.* 2001). Si le comportement pseudo-solide tenait de l'expression du confinement des chaînes polymériques, l'énergie d'activation devrait croître avec la fraction volumique d'argile. Le comportement pseudo-solide est le plus souvent attribué à la percolation des feuillets et de leurs agrégats. La faible concentration volumique de phyllosilicates (~ 1,5 vol. % avec de la MMT (Aubry *et al.* 2005)) requise pour atteindre le seuil de percolation au regard de celle requise pour un système chargé de sphères (~ 30 vol. % (Isichenko 1992)) s'explique par la forte anisotropie des particules qui limite leur rotation et la dissipation des contraintes. Lim *et al.* (2001) rappellent en effet que les suspensions de phyllosilicates atteignent le régime de concentration concentré à de faibles fractions volumiques d'argile, en raison du rapport de forme élevé des feuillets. Wang *et al.* (2002) illustrent l'importance de ce rapport de forme en observant qu'à la même fraction volumique, le comportement pseudo-solide s'accentue avec leur rapport de forme. Ils ont réalisé pour cela deux nanocomposites composés d'un même polymère (polyéthylène maléique) auquel est ajouté pour le premier de la montmorillonite d'un rapport de forme compris entre 100 et 200 et de la laponite d'un rapport de forme compris entre 20 et 30 pour le second; les deux argiles sont tous deux

modifiés de la même façon avec des ions alkylammonium. Leurs résultats s'accordent avec ceux obtenus de la même façon par Mitchell et Krishnamoorti (2002) pour leurs nanocomposites composés d'un copolymère à bloc polystyrène – polyisoprène. Ren *et al.* (2000) confirment l'hypothèse d'un réseau percolé en estimant le seuil de percolation de leur nanocomposite. À partir de considérations volumiques, ils relient la fraction volumique au seuil de percolation, W_{per}, avec le nombre moyen de feuillets par particule primaire, n_{per} de la façon suivante :

$$n_{per} = \frac{4}{3\phi}\left[\frac{W_{per}\rho_p}{W_{per}\rho_p+(1-W_{per}\rho_s)}\right]\frac{R_h}{h_a} \tag{1.1}$$

Avec ρ_p, ρ_s la densité du polymère et de l'argile, respectivement, R_h le rayon du volume hydrodynamique des feuillets et h_a leur épaisseur. Ils obtiennent une bonne corrélation entre leur prédiction et leur résultat expérimental. Tout récemment, Aubry *et al.* (2005) ont démontré que l'énergie, E, nécessaire pour briser le réseau des particules d'argile est indépendante de leur concentration. Ils définissent cette énergie de la façon suivante :

$$E = \int_0^{\gamma^0} \tau \, d\gamma = 1/2 G_0'(\gamma^0)^2 \tag{1.2}$$

Avec G'_0 le module élastique aux faibles fréquences et γ^0 la déformation à laquelle débute la zone non linéaire. Un tel comportement suggère selon eux que le comportement pseudo-solide des nanocomposites n'est pas lié à la présence individuelle des particules d'argile, mais davantage à leur présence sous forme de domaines dont leur taille caractéristique est indépendante de la concentration d'argile.

Selon les études de diffusion des rayons X aux petits angles de Bafna *et al.* (2003), de Galgali *et al.* (2004), de Kojima *et al.* (1994, 1995), de Lele *et al.* (2002), de Medellin-Rodriguez *et al.* (2001) et de Varlot *et al.* (2001), les feuillets d'argile s'orientent lors d'un écoulement de cisaillement selon la direction de l'écoulement avec leur surface principale normale au gradient de cisaillement. Leurs propriétés viscoélastiques linéaires après pré-cisaillement sont significativement plus faibles (à toutes les fréquences) que celles mesurées avant pré-cisaillement (Koo *et al.* 2003, Li *et al.* 2003). De la même façon, l'application d'un cisaillement oscillatoire de grande amplitude (LAOS) affaiblit les propriétés viscoélastiques linéaires subséquentes (Krishnamoorti et Giannelis 1997, Lim et Park 2001, Ren *et al.* 2003, Ren et Krishnamoorti 2003, Ren *et al.* 2000). L'aptitude d'un LAOS à orienter les feuillets d'argile, comme observé pour les copolymères à blocs (Gupta *et al.* 1996), a été confirmé aux faibles échelles par Ren *et al.* (2003) et Koo *et al.* (2003) par des mesures de rayons X.

Suite à un cisaillement oscillatoire de grande amplitude, Ren *et al.* (2003) ont observé pour leurs nanocomposites à base de polystyrène et de poly(isobutylène-*co*-*p*-methylstyrene) une augmentation logarithmique dans le temps du module élastique. Ils l'attribuent à la perte de l'orientation induite lors du pré-cisaillement oscillatoire. La cinétique est montrée indépendante de la température, de la dimension des particules, de la viscosité et du poids moléculaire du polymère. Ils excluent alors le mouvement Brownien du processus supposé de désorientation bien que l'échelle de temps donnée par le coefficient de diffusion en rotation pour leurs feuillets de phyllosilicate soit

comparable à celles de leurs mesures. Solomon *et al.* (2001) ont reporté la perte d'orientation pour leurs nanocomposites à base de polypropylène après un pré-cisaillement en utilisant la diffraction des rayons X. Le temps de relaxation donné par la diffraction des rayons X s'est révélé beaucoup plus rapide que celui attendu par le seul mouvement Brownien ($1/D_r$). Ils suggèrent alors que la rapide relaxation de l'orientation des feuillets est induite par la relaxation des chaines de polymère. Cette hypothèse fut rejetée par Lele *et al.* (2002) qui observèrent un temps de relaxation diminuant avec l'ajout d'un compatibilisant.

1.4.3. Propriétés viscoélastiques non linéaires

a) Régime dynamique

Le comportement non linéaire des nanocomposites est observé à de faibles déformations comme l'illustrent Krishnamoorti *et al.* (2001) pour leurs nanocomposites polystyrène/polyisoprène. La zone linéaire restreinte des nanocomposites par rapport à leur matrice seule témoigne de l'évolution sous déformation de la structure formée par les feuillets.

Tanoue *et al.* (2004) ont analysé la réponse en oscillation de leurs nanocomposites au-delà de leur zone linéaire. Ils ont pour cela appliqué les développements récents proposés par Wilhem (1998, 1999, 2002) au niveau de la rhéologie par transformée de Fourier. Elle permet de quantifier la réponse non linéaire d'un matériau soumis à un cisaillement oscillatoire de grande amplitude et repose sur l'analyse des harmoniques du signal du couple du rhéomètre. Ils ont ainsi suivi l'évolution de l'amplitude de la

troisième harmonique en fonction de l'amplitude de déformation pour leur nanocomposite à base de polystyrène.

b) Régime permanent

La viscosité en cisaillement permanent des nanocomposites diverge de celle de leur matrice en exhibant un seuil de contrainte (Krishnamoorti *et al.* 2001, Lim *et al.* 2003, Ren et Krishnamoorti 2003, Solomon *et al.* 2001). Wagener *et al.* (2003) clament que le degré d'exfoliation d'un nanocomposite est quantifiable à partir de la seule observation de sa viscosité aux faibles taux de cisaillement. L'absence de l'aspect quantitatif de leur étude invite à modérer cette affirmation tout comme l'absence de travaux dédiés à l'étude de l'influence de l'interface matrice/argile sur le comportement rhéologique de ces suspensions. Aux plus hauts taux de cisaillement, la tendance inverse est observée : la viscosité des nanocomposites de phyllosilicates se confond avec celle du polymère en suivant son comportement rhéofluidifiant. Un tel comportement s'accorde avec les études sur l'orientation des particules d'argile décrites précédemment. Il suggère en effet que les feuillets s'orientent fortement selon l'écoulement laissant le comportement du polymère dominer la rhéologie du nanocomposite.

Les observations de viscosité en cisaillement permanent rejoignent celles faites en régime dynamique. Cependant, le principe de Cox-Merz, selon laquelle la viscosité complexe équivaut à la viscosité en régime permanent pour une fréquence égale, ne s'applique pas aux nanocomposites (Krishnamoorti et Giannelis 2001, Ren et

Krishnamoorti 2003). Cet échec doit vraisemblablement s'expliquer par la différence de l'état de dispersion des feuillets lors de ces deux régimes d'écoulement.

c) Régime transitoire

Solomon *et al.* (2001, PP/PP-g-MAH/MMT), Li *et al.* (2003, PP/ PP-g-MAH/MMT), Lee et Han (2003, PC/MMT), et Letwimolnum *et al.* (2007, PP/PP-g-MAH/MMT) s'intéressent au comportement transitoire sous cisaillement des nanocomposites en vu de suivre l'évolution de leur microstructure et de leur relaxation. Ils appliquent pour cela des démarrages à différentes vitesses imposées à leurs nanocomposites. Solomon *et al.* (2001) appliquent également un second démarrage dans le sens de rotation contraire au premier après différents temps de repos.

Le pic de contrainte mesuré lors du premier démarrage est attribué à l'évolution d'orientation de la structure d'argile. Il croît avec la vitesse de démarrage (Li *et al.* 2003, Solomon *et al.* 2001) et le degré d'exfoliation (Lee et Han 2003) tandis que sa position en terme de déformation reste constante (Li *et al.* 2003, Solomon *et al.* 2001). Une tendance inverse avec le taux de cisaillement fut observée par Sepehr *et al.* (2004) pour leur suspension de fibres de verre courtes dans du polybutène (fluide newtonien inélastique) et dans un fluide de Boger (fluide newtonien élastique). L'amplitude du second pic observé lors du second démarrage augmente quant à lui avec le temps de repos (Lee et Han 2003, Li *et al.* 2003, Solomon *et al.* 2001) révélant que la structure d'argile évolue après l'arrêt d'un pré-cisaillement comme mentionné précédemment par l'étude de Ren *et al.* (2003). Il augmente de plus linéairement avec la concentration

d'argile (Solomon *et al.* 2001). Lee et Han (2003) n'observent pas cependant pour leurs nanocomposites intercalés à base de polycarbonate et d'argile non modifiée une dépendance de l'amplitude du second pic avec le temps de repos. Le temps caractéristique du mouvement Brownien est estimé par Solomon *et al.* (2001) pour leurs systèmes à plus de 2000 s. Il ne permet pas selon eux d'expliquer la désorientation de la structure d'argile qui intervient lors de leurs mesures à des temps inférieurs. Ils retiennent alors l'interaction entre les nano-feuillets comme force motrice pour leur désorientation. Tout récemment, des premiers travaux cherchant à modéliser le comportement transitoire ont été menés par Letwimolnum *et al.* (2007) et Eslami *et al.* (2007).s

La viscosité élongationnelle transitoire de nanocomposites, telle que mesurée par un rhéomètre élongationnel similaire à celui développé par Meissner (Meissner et Hostettler 1992) (RME de Rheometric Scientific : $\dot{\varepsilon} = [10^{-3}, 1]\ s^{-1}$), suit un comportement de rhéo-durcissement (Kim *et al.* 2004, Okamoto *et al.* 2001, Seong et Youn 2004). Il débute à une déformation qui augmente avec le taux de déformation contrairement aux homopolymères (Okamoto *et al.* 2001) et dépend de la morphologie du nanocomposite. À une même concentration d'argile, un tel comportement est plus prononcé pour les nanocomposites supposés exfoliés (Kim *et al.* 2004, Seong et Youn 2004). L'interface entre le polymère et l'argile qui augmente avec le degré d'exfoliation est tenue responsable par Kim *et al.* (2004) du comportement rhéopexique. Ils soulignent que l'état d'orientation de l'argile semble jouer qu'un faible

rôle dans le mécanisme rhéopexique. Ils l'observent en effet tout comme Okamoto *et al.* (2001) avant que l'orientation des particules d'argile ne soit bien définie.

Finalement, la règle de Trouton n'est pas respectée. Pour un nanocomposite compatibilisé à base d'un polypropylène et de 4 wt. % d'argile, la viscosité élongationnelle transitoire est quelque soit la déformation atteinte plus de dix fois supérieure à son homologue en cisaillement (Okamoto *et al.* 2001).

1.4.4. Synthèse

Les suspensions et nanocomposites de phyllosilicate exhibent une transition d'un comportement liquide à un comportement solide à des fractions volumiques faibles, inférieures à 5 %. Le comportement solide se traduit par une faible dépendance en fréquence des modules viscoélastiques accompagnée d'un seuil de contrainte en régime permanent. Il est attribué le plus souvent à la percolation des feuillets et de leurs agrégats. À une même fraction volumique de phyllosilicate, l'exfoliation des feuillets est donc déduite de l'augmentation des modules viscoélastiques ou du seuil de contrainte. En revanche, la diminution du module élastique suite à un écoulement en cisaillement est expliquée par l'orientation des feuillets induite par le pré-cisaillement. La diffraction des rayons X suggère en effet que les feuillets s'orientent sous écoulement selon la direction du cisaillement avec leur surface principale normale à son gradient de vitesse. Le comportement rhéofluidifiant de ces systèmes est également attribué à l'orientation des feuillets sous écoulement. Suite à un pré-cisaillement, l'augmentation dans le temps du module élastique, et la présence d'un pic de contrainte

lors d'un subséquent démarrage à vitesse imposée, sont par conséquent attribués à la relaxation de l'orientation des particules. Le mouvement Brownien est écarté comme force motrice par la plupart des auteurs au profit de l'interaction entre les nano-feuillets.

L'interprétation donnée dans les nombreuses études du comportement rhéologique des suspensions et des nanocomposites de phyllosilicate repose essentiellement sur l'orientation des feuillets ou d'empilements de feuillets et de leur percolation. Une telle interprétation doit cependant être considérée avec précautions tant la caractérisation de l'état de dispersion des feuillets est le plus souvent incomplète ou ambiguë. Elles se basent principalement sur la diffraction des rayons X et la microscopie électronique à transmission (MET). Elles ne tiennent donc pas compte de la distribution spatiale des feuillets au-delà de l'échelle nanométrique, et ainsi de leur éventuelle organisation multi-échelle. La persistance de forces attractives entre les feuillets organophiles est susceptible de donner lieu à la formation d'agrégats de nature fractale en masse. Leur percolation confèrerait également un comportement solide à ces systèmes. L'hypothèse de la formation d'agrégats de nature fractale en masse n'a pas été considérée dans la littérature pour interpréter le comportement rhéologique des systèmes non-aqueux de phyllosilicates. Elle est prise à partie tout au long de cette étude, et tout particulièrement lors de l'investigation de la distribution spatiale des suspensions non-aqueuses de phyllosilicate étudiées. L'interprétation de leur comportement rhéologique est en effet étendue au-delà du seul examen de l'état d'orientation des feuillets.

CHAPITRE 2 - SYNTHÈSE DES ARTICLES

Le premier article intitulé, « Effect of flow history on the structure of a non-polar polymer/clay nanocomposite model-system », met en évidence l'influence de l'histoire d'écoulement sur les propriétés viscoélastiques linéaires et non linéaires d'une suspension non-polaire de phyllosilicate organophile. La relaxation de l'état de dispersion de cette suspension suite à des pré-cisaillements de différentes amplitudes a été suivie en mesurant ses propriétés viscoélastiques linéaires, tandis que l'évolution de l'état de dispersion sous écoulement a été constatée en imposant des sauts de vitesse de cisaillement. Pour évaluer la cinétique de l'évolution de l'état de dispersion sous écoulement, et au repos, des équations empiriques de forme exponentielle ont été utilisées. Il est montré que suite à des pré-cisaillements de différentes amplitudes, différentes structures métastables sont atteintes au repos selon la même cinétique de recouvrement. Une plus faible amplitude de pré-cisaillement donne naissance à une structure métastable plus rigide. Il s'ensuit que le comportement aux faibles fréquences s'apparente à un comportement pseudo-solide d'autant plus prononcé que l'amplitude du pré-cisaillement est faible. L'existence des structures métastables est attribuée au volume exclu important des feuillets. Leur développement n'est pas seulement contrôlé par le mouvement Brownien mais également par les forces hydrodynamiques lors du pré-cisaillement qui permettent de surmonter les forces de répulsions liées au volume exclu. La rupture sous écoulement des structures métastables s'accompagne d'un pic de contrainte dont l'amplitude augmente avec la diminution de l'amplitude du pré-

cisaillement. Un pic de contrainte est également observé lors de la rupture des structures métastables par un écoulement de sens opposé à celui de leur pré-cisaillement. Son amplitude est alors plus faible suggérant une forte anisotropie des structures métastables.

Par la suite, les articles établissent la nature et l'origine des structures métastables. L'anisotropie induite par écoulement est dans un premier temps abordée dans un second article intitulé, « Anisotropy of non-aqueous layered silicate suspensions subjected to shear flow ». Elle est qualitativement observée par des mesures de diffusion de lumière en deux dimensions et quantifiée par des mesures de dichroïsme réalisées sous écoulement. Une nouvelle méthode non destructive reposant sur l'écoulement oscillatoire linéaire étendu en deux dimensions (2D-SAOS) a également été développée pour quantifier l'anisotropie des structures métastables. L'existence sous écoulement et au repos de microstructures de nature fractale a été déduite des clichés de diffusion de lumière. La dimension fractale constante avec la vitesse de cisaillement indique l'absence de densification sous écoulement des microstructures. Les mesures de dichroïsme ont montré que l'évolution d'anisotropie dans le plan du gradient de cisaillement et celle dans le plan de vorticité interviennent sur des plages de vitesse de cisaillement différentes. Dans le plan de vorticité, le développement de l'anisotropie selon la direction d'écoulement suit le comportement rhéofluidifiant de la suspension, et fut donc attribué à une évolution d'orientation de la microstructure. À contrario, l'anisotropie dans le plan du gradient de cisaillement s'intensifie une fois le plateau de viscosité atteint, et n'implique qu'une évolution mineure de l'angle

d'orientation. L'anisotropie induite aux hauts taux de cisaillement dans le plan du gradient de cisaillement peu être expliquée par l'évolution de la distribution spatiale des éléments constitutifs de la microstructure comme suggéré par les clichés de diffusion de lumière à deux lobes. Suite à un pré-cisaillement, l'absence de relaxation de l'anisotropie induite par écoulement est explicitement montrée avec les mesures de 2D-SAOS. Les microstructures métastables ont par conséquent la même nature anisotrope que leur contrepartie sous écoulement. En raison de l'anisotropie induite par écoulement, la réponse transitoire des suspensions impliquent à la fois des contributions de structure, c.-à-d. liée à l'évolution de la distribution spatiale des feuillets, et d'orientation. Le rôle important de la contribution d'orientation est dévoilé en comparant des démarrages à vitesses imposées de sens opposés. Elle se révèle d'autant plus importante que l'écoulement transitoire implique une rupture de la microstructure.

Le troisième article intitulé, « Structural analysis and scaling behavior of non-aqueous layered silicate suspensions », examine en détail l'évolution sous écoulement des micro-structures, en termes de distribution spatiale, d'une suspension non-polaire de phyllosilicate organophile, et d'une suspension polaire de phyllosilicate naturel. Le comportement d'échelle avec la température, la fraction volumique de phyllosilicate, et l'histoire d'écoulement de leurs propriétés viscoélastiques est dans un premier temps étudié. Des courbes maitresses de leurs propriétés viscoélastiques linéaires et non linéaires ont été obtenues en utilisant respectivement des facteurs de glissement définis selon les valeurs du module élastique aux faibles fréquences et l'amplitude du seuil de

contrainte. Selon les théories fractales, les lois d'échelle des propriétés pseudo-solides ont été attribuées à la présence de microstructures composées d'agrégats de nature fractale en masse. Des observations directes en utilisant la microscopie confocale à balayage laser a permis de confirmer leur présence et de quantifier leur distance caractéristique. Les propriétés rhéologiques similaires des suspensions polaires et non-polaires, alors que la plage des fractions volumiques pour la suspension polaire est dix fois inférieure, sont expliqués à partir du potentiel d'interaction entre les feuillets et leurs agrégats. Le potentiel d'attraction responsable de la microstructure fractale a été mis en évidence grâce à sa dépendance en température. Elle est similaire pour les deux suspensions bien que la suspension polaire présente un comportement sous écoulement non réversible avec la température. En augmentant le taux de cisaillement, la taille caractéristique des structures diminue d'une haute à une faible valeur au plateau. Cette évolution structurelle avec l'amplitude du cisaillement est attribuée à une agrégation réversible induite par écoulement. Suite à un pré-cisaillement, aucune relaxation structurelle à l'échelle microscopique n'a été observée en microscopie confocale à balayage laser. Les microstructures métastables ont donc la même taille caractéristique que leur contrepartie sous écoulement. Le comportement thixotrope de ces suspensions implique alors des réarrangements à l'échelle nanoscopique. Finalement, l'influence de l'histoire d'écoulement sur les propriétés viscoélastiques linéaires et non linéaires de ces suspensions est attribuée à la taille caractéristique de la microstructure contrôlée par la vitesse de cisaillement.

CHAPITRE 3 - ARTICLE: EFFECT OF FLOW HISTORY ON THE STRUCTURE OF A NON-POLAR POLYMER/CLAY NANOCOMPOSITE MODEL SYSTEM

Christophe Mobuchon, Pierre J. Carreau and Marie-Claude Heuzey

Center for Applied Research on Polymers and Composites (CREPEC), Chemical Engineering Department, Ecole Polytechnique, PO Box 6079, Stn Centre-Ville, Montreal, QC, Canada H3C3A7

3.1. Abstract

The effect of flow history on the linear and nonlinear viscoelastic properties of non-polar polymer nanocomposites (PNCs) has been investigated by means of a suitable model system based on a Newtonian matrix. The structural recovery of this model suspension after cessation of different pre-shear rates was monitored by measuring its linear viscoelastic properties while its structural evolution under shear flow was followed by using stepwise changes in shear rate including flow reversal measurements. To assess the kinetics of the structural evolution at rest and under flow,

---

Cet article a été présenté lors de la 3ième conférence annuelle de l'European Society of Rheology (A.E.R.C.) et publié par la revue Rheologica Acta

empirical relations of stretched exponential form were used. It is shown that for different pre-shear rates, different equilibrium structures were reached at rest but with a similar kinetics of recovery. As a result, the low frequency behavior was typical of solid-like or weak gel material, strongly dependent on the flow history. After any given shear rate under steady state, only one reversible equilibrium structure was reached after a kinetics that was dependent on the preshear history. Finally, typical flow reversal responses as observed for PNCs are reported and interpreted in light of the microstructure evolution under flow.

3.2. Introduction

Layered silicates find widespread industrial applications such as rheological modifiers in paints, inks, emulsions or pigment suspensions, adsorbent in water treatment, and more recently as drug delivery carriers for controlled release of therapeutic agents and as nanoscale fillers for reinforcement of polymers (Patel *et al.* 2006). Polymer/layered silicate nanocomposites (PNCs) have attracted great interests since Okada *et al.* (1987) developed a nylon based nanocomposite with significant improvements in tensile modulus and heat distortion with as little as 2 vol % of layered silicate. Recent studies to extend a similar achievement to a wider range of polymer matrices, including vinyl and polyolefins, have also shown an enhancement of flexural, barrier and fire retardancy properties and unusual chemical and physical phenomena, such as highly

anisotropic electrical conductivity and photoactivity when compared with conventional fillers (Ray and Okamoto 2003).

The layered silicates used in the synthesis of polymer nanocomposites belong to the same structural family than the well-known clays mica and talc, i.e. 2:1 phyllosilicates (Grim 1968, Rossman and Carel 2002). The most commonly used is the montmorillonite for which the individual layers are stacked with relatively weak electrostatic forces facilitating the dispersion of the layers. The individual clay layers can be approximated by ellipsoidal tactoids about 1.2 nm thick, 320-400 nm long and 250 nm wide for the larger ones (Cadene *et al.* 2005).

The individual dispersion of these layers, i.e. their exfoliation, can lead to a large interfacial area in polymer matrix approaching m^2/mL compared to cm^2/mL for particles of micrometer dimensions (Krishnamoorti and Vaia 2002). This large interfacial interaction between the polymer matrix and the layered silicate explains the improved mechanical and physical properties over conventional polymer composites. Despite intensive research efforts, the exfoliation of inorganic layered silicates remains a main challenge, especially in non-polar polymers. In the latter case, the incompatibility is overcome by using a coupling agent with organically modified layered silicates. Structurally, three different morphologies are achievable on the basis of the affinity between the polymer and the layered silicate: exfoliated nanocomposites as defined previously, intercalated nanocomposites, where the insertion of polymeric chains between the clay layers occurs but the stacking of layers is preserved, and

finally conventional macrocomposites in the case of immiscible systems, when the polymer does not penetrate the stack of silicate layers.

To tailor PNCs with expected properties and to control their processing, a thorough understanding of PNCs rheological behaviour with regards to the previously defined morphologies and their structural evolution is essential. In addition to the large interfacial area, the rheological behaviour is expected to be governed by two main features, i.e. the high aspect ratio of the clay layers and the effect of Brownian motion on the nanoparticles. The high aspect ratio of the clay layers, or high anisotropy, implies large excluded volumes, which results in clay restricted motion at low volume fraction, corresponding to a concentrated regime. The concentrated regime is reached when $p\phi/\pi \gg 1$, with p the aspect ratio and ϕ the volume fraction of the clay particles (Lim and Park 2001). Actually, for a collection of oriented clay particles, the mean distance between the clay particles considered as discs with a thickness of 1.2 nm approaches 30 nm at a volume fraction of 4 % compared with their lateral dimensions larger than 200 nm. It is interesting to note that due to their high aspect ratio a relative flexibility of the clay layers can also be observed (Morgan and Gilman 2003). Furthermore, due to their nanometric dimensions, these clay particles in suspension are subjected to Brownian motion, which tends to randomize their relative position and reorient the nanoparticles at rest. Under flow, the Brownian forces (and possibly other colloidal forces) are counterbalanced by the hydrodynamic forces. The relative balance between these two is expressed by the Peclet number, given by $\mathrm{Pe} = \dot{\gamma}/D_r$, where $\dot{\gamma}$ is

the shear rate and D_r the rotary diffusion coefficient. The rotary diffusion coefficient of the clay layers can be calculated as: $D_r = 3k_BT/4\eta d^3$ (Ren *et al.* 2003) where k_B is the Bolztmann constant, T the absolute temperature, η the viscosity of the matrix and d the particle diameter. The competition between the Brownian motion and the hydrodynamic forces leads to a complex reversible time-dependent rheological behaviour, which is characteristic of colloidal suspensions, i.e. a thixotropic behaviour related to changes occurring in the inner structure of the fluid such as spatial distribution and orientation (Barnes 1997).

Previous rheological studies of PNCs primarily focused on their linear rheological behaviour, and the key results are reviewed by Krishnamoorti and Yurekli (2001). The most striking observation is the solid-like behaviour, i.e. G' and $G'' \sim \omega^0$ at low silicate loadings (as low as 1.5 vol % as reported by Aubry *et al.* (2005)). This non-terminal flow behaviour has been observed for exfoliated nanocomposites (Hoffmann *et al.* 2000a, Koo *et al.* 2003, Krishnamoorti and Giannelis 1997, Li *et al.* 2003, Lim and Park 2001, Meincke *et al.* 2003, Wang *et al.* 2002). It has also been observed for intercalated PNCs (Galgali *et al.* 2001, Lim and Park 2001, Ren *et al.* 2000, Solomon *et al.* 2001), for PNCs based on polar matrices (Aubry *et al.* 2005, Hsieh *et al.* 2004, Krishnamoorti and Giannelis 1997, Lepoittevin *et al.* 2002) as well as for non-polar polymers (Hoffmann *et al.* 2000a, Koo *et al.* 2003, Li *et al.* 2003, Lim and Park 2001, Meincke *et al.* 2003, Solomon *et al.* 2001, Wang *et al.* 2002). The non-terminal flow behaviour is attributed to the formation of a percolated three-dimensional network,

which hinders the relaxation of the clay particles when subjected to small-amplitude oscillatory shear (Galgali *et al.* 2001, Mitchell and Krishnamoorti 2002, Ren *et al.* 2000). As outlined previously, the particle-to-particle distance shorter than their lateral dimensions prevents the free rotation of the particles and the stress relaxation. The relatively low silicate volume fraction (~ 1.5 vol %, Aubry et al. 2005) for which the percolation threshold is reached is strikingly different from the case of spheres (~ 30 vol %, Isichenko 1992, Ren et al. 2000, Wang et al. 2002), and is also a consequence of the high anisotropic nature of the clay particles. According to the small-angle X-ray scattering (SAXS) studies (Bafna *et al.* 2003, Galgali *et al.* 2004, Kojima *et al.* 1994, Kojima *et al.* 1995, Lele *et al.* 2002, Medellin-Rodriguez *et al.* 2001, Varlot *et al.* 2001), clay layers are oriented in shear flow with their major axis along the flow direction and their surface nearly oriented in the shear plane. The linear viscoelastic response following steady pre-shear flows is significantly weaker (at all frequencies) than those measured before pre-shear (Koo *et al.* (2003) Li *et al.* (2003)). Similarly, application of a prolonged large amplitude oscillatory shear (LAOS) affects in the same way the subsequent linear viscoelastic response (Krishnamoorti and Giannelis 1997, Lim and Park 2001, Ren *et al.* 2003, Ren and Krishnamoorti 2003, Ren *et al.* 2000). The ability of LAOS to orient the clay layers, as observed for block copolymers (Gupta *et al.* 1996), has been confirmed by Ren *et al.* (2003) and Koo *et al.* (2003) conducting ex-situ X-ray measurements.

The previous studies underline the correlation between the linear viscoelastic properties of PNCs and the microstructure induced by a well defined preconditioning. Several outstanding issues are yet to be investigated such as the evolution of the rheological response and of the clay structure during preconditioning (not reported in any of the previous studies) and the effect of preconditioning on the non-linear viscoelastic properties. Moreover, previous investigations have been restricted to a few different experimental conditions. Only one shear rate was applied by Koo *et al.* (2003, 1 s^{-1}) and by Li *et al.* (2003) while LAOS experiments have been limited to two sets of experimental conditions: a strain of 1.2 at a frequency of 1 rad/s (Krishnamoorti and Giannelis 1997, Lim and Park 2001, Ren *et al.* 2003) and a strain of 1.5 at 0.1 rad/s (Ren *et al.* 2003).

The kinetics of disorientation following LAOS preconditioning has been examined by Ren *et al.* (2003) using linear viscoelastic measurements for polystyrene and poly(isobutylene-*co*-*p*-methylstyrene) based PNCs. They observed logarithmic increases with time of the storage modulus, which did not depend significantly on the dimensions of the silicate layers, temperature, viscoelasticity and molecular weight of the polymer matrix. They concluded from these results that the disorientation process was not governed by Brownian motion. Lele *et al.* (2002) have reported the relaxation of orientation for polypropylene based PNCs following a steady pre-shear preconditioning using in situ X-ray diffraction measurements. They confirmed the conclusion of Ren *et al.* (2003), since the relaxation time scale from rheo-XRD

measurements was much faster than the expected Brownian relaxation time ($1/D_r$). Instead, they suggested that the rapid relaxation of the nanoparticle orientation was driven by the stress relaxation of the polymer matrix chains. Solomon *et al.* (2001) also observed a relaxation faster in polypropylene based PNCs than the one expected from Brownian motion. This was attributed to the attractive interactions between the clay tactoids in the quiescent structural evolution after a steady pre-shear. This last explanation was rejected by Lele *et al.* (2002) since they observed a relaxation time depending on the presence of a coupling agent (*i*-PP/maleic anhydride copolymer). Actually, the uncompatibilized PNCs at a similar clay loading exhibited slower relaxation times than the compatibilized ones.

Solomon *et al.* (2001) investigated the extent of the relaxation by conducting reversal flow measurements. They monitored the stress growth upon start-up of steady shear flow in the reverse direction following a first start-up at the same shear rate. A stress overshoot was only observed during the reverse flow when a rest time between the two consecutive experiments was sufficiently long. The reverse overshoot was explained by the reorientation and the network structure built-up during rest time. The overshoot magnitude was found to increase with rest time, but with time scales much shorter than expected from Brownian motion, leading Solomon *et al.* (2001) to the hypothesis that Brownian motion was not the driving force for the quiescent structural evolution.

Finally, fewer reports have been made on the non-linear viscoelastic properties of PNCs measured during the first start-up of steady shear flow (Lee and Han 2003, Li *et*

al. 2003, Solomon *et al.* 2001). The stress overshoot during the first start-up flow was found to increase with the applied shear rate (Li *et al.* 2003, Solomon *et al.* 2001) and the extent of clay exfoliation (Lee and Han 2003). The transient stress was found to scale with the strain, indicating that the Brownian motion did not significantly contribute to the stress response in the shear rate range investigated (0.005 to 1 s^{-1}).

In the present study, the effect of flow history on the linear and nonlinear viscoelastic properties of non-polar PNCs was carefully investigated by examining the rheological behaviour of a suitable model system based on a Newtonian matrix. At first, we present the structural recovery of this model suspension monitored by measuring the linear viscoelastic properties after cessation of different pre-shear rates. Afterwards, the structural evolution under shear flow conditions is reported for stepwise changes in shear rate including flow reversal measurements. To assess the kinetics of the structural evolution at rest and under flow, empirical relations of stretched exponential form are used.

3.3. Experimental

3.3.1. Materials and preparation methods

The layered-silicate selected for the model suspension was a montmorillonite, $M_x(Al_{2-y}Mg_y)Si_4O_{10}(OH)_2.nH_2O$, organically modified with a dimethyl dihydrogenated quaternary ammonium salt, $CH_3CH_3N^+HTHT$, where HT is a hydrogenated tallow

(Cloisite® 15A, Southern Clay Products). The specific gravity of this organophilic clay is 1.66.

The clay was added at a volume fraction of 4 % in a non-polar Newtonian fluid consisting of a blend of two miscible polybutenes, $R[CH_2CCH_3CH_3]_x[CH_2]_yR$, of different molecular mass, respectively 910 g/mol (76.4 mass %, Indopol H100, BP) and 1300 g/mol (23.6 mass %, Indopol H300, BP) with an overall viscosity of 28.5 Pa.s at 25 °C and a density of 0.89 g/mL. Under flow, the clay particles dispersed in the polybutene are, thus, not subjected to electrostatic repulsion or attraction but only to van der Waals interactions, steric forces, excluded volume effect, Brownian motion and hydrodynamic forces.

The model suspensions were prepared via ultrasonication, using pulses of 240 W during 1s every 5 s at 60 °C for 60 min. (Sonics & Materials). This was followed by a rest time in a high vacuum oven at 60 °C to remove air bubbles prior to measurements. The duration of ultrasonication was found not to affect the degree of dispersion of the suspensions as measured by the amplitude of the dynamic storage modulus plateau, and the suspension was found to be very stable over long periods of time. Other methods of incorporating the nanoclay to the polybutene were observed to strongly affect the rheological properties. However, this will not be discussed here and will be the topic of another publication. After sonication, the initially cloudy dispersions became translucid and gel-like, indicating enhancement of the dispersion degree. To investigate further the clay dispersion in the polybutene, wide angle X-ray diffraction (WAXRD) was

used. The data were collected using a Philips X'pert powder diffractometer with CuKα (λ = 1.54Å) radiation and an accelerating voltage of 50 kV/40 mA. The step size and the scanning speed were 0.025° and 2s/step respectively. While the observed gelation of the suspensions indicated exfoliation of the clay layers, their diffraction pattern (not shown here) still presented the characteristic d_{001} basal reflection peak of Cloisite 15A. This peak is indicative of the presence of stacked clay layers as confirmed by transmission electron microscopy (TEM). Figure 3.1 shows a typical TEM micrograph of the model suspension under a large magnification. The TEM micrograph was taken from a 100 nm thick, ultracryomicrotomed section of the model suspension using an Ultracut E ultracryomicrotome (Reichert & Jung) at – 80 °C. Imaging was performed with a JEOL JEM-2000FX transmission electron microscope at an accelerating voltage of 80 kV. Both individual silicate layers and thin clay tactoids can be seen from the micrograph of Figure 3.1. Therefore, clay exfoliation was not perfectly achieved, explaining the single diffraction peak observed in WAXRD. This non-homogeneous morphology is close to commonly observed dispersion states for non-polar polymer/clay nanocomposites (see for instance Li *et al.* (2003)).

Finally, with a typical value of d = 320 nm, the Peclet number is estimated to be between 10^{-1} and 10^{5} for shear rates ranging from 10^{-3} to 10 s^{-1}. This suggests that the Brownian motion must play a key role in this shear rate range. To evaluate the Peclet number, the viscosity of our suspension at high shear rate, $\eta \approx 70$ Pa.s at T = 295 K

(see Figure 3.2a), was used rather than that of the matrix, to account for the fact that our suspension is highly concentrated (Moan *et al.* 2003).

3.3.2. Rheometry

All the rheological measurements were carried out using a stress-controlled rheometer (Physica MCR 501, Anton Paar), except for the stress relaxation measurements that were performed with a strain-controlled rheometer, (ARES, Rheometric Scientific). All tests were done at 25 °C using a cone-and-plate geometry with a radius of 25 mm and a cone angle of 0.04 rad. We assumed that the particle sizes were sufficiently small compared to the gap (h) of the cone-and-plate geometry (i.e. $d/h < 0.1$). Small amplitude oscillatory shear (SAOS) frequency sweep tests were conducted in the range of 0.628 to 628 rad.s^{-1} at a fixed strain of 0.005. For stress relaxation experiments, the ARES rheometer was preferentially used since its force rebalanced torque system was more suitable for measuring the true sample response when the filters were bypassed to avoid electronic interferences from the instrument (Dullaert and Mewis 2005b, Mackay *et al.* 1992). The raw data from the ARES force rebalanced transducer were sampled every 10^{-4} s with a 12-bit data acquisition card (DAQPAd-6020E, National Instruments) and the data handling was performed using a LabVIEW routine (National Instruments). For the stepwise shear rate measurements using the MCR, the data were considered after a period of 0.04 s, time required to reach the specified shear rate within an error of less than 2 %.

The absence of slip and wall effects for the model suspension have been ascertained using a parallel plate geometry with a radius of 25 mm. The effect of the gap (varied from 0.2 to 1.4 mm) and of the roughness of the geometry (smooth and modified with sandpaper: 220 grit, aluminium oxide) on the steady-shear measurements were found to be insignificant, less than the reproducibility of the data estimated to be within ± 2 and ± 9 % for shear rates of 25 and 0.001 s^{-1}, respectively. For dynamic measurements, the standard deviation based upon five measurements carried out with fresh samples was estimated to be within ± 8 %.

To confer the same shear flow history at the beginning of each measurement, the suspensions were subjected to a constant pre-shearing. Initially, various pre-shearing rates were tested in order to optimize the conditioning. While investigating the resulting structures using small amplitude oscillatory shear, strikingly different results were obtained. Figure 3.2**Erreur ! Source du renvoi introuvable.**a reports the steady-shear viscosity of the model suspension for tests carried out from 25 to 10^{-3} s^{-1}. The behaviour is typical of a highly concentrated suspension, with a gel-like structure responsible for an unbounded viscosity (apparent yield stress) at low shear rates and a plateau viscosity at very high shear rates. Figure 3.2**Erreur ! Source du renvoi introuvable.**b presents the evolution of the storage modulus *G'* at a frequency of 125.6 rad.s^{-1} following each applied pre-shear rate shown in Figure 3.2**Erreur ! Source du renvoi introuvable.**a, starting with the larger value of 25 s^{-1}. Some structure build-up curves have been removed from Figure 3.2**Erreur ! Source du renvoi introuvable.**b

for clarity. For the larger values of the initially applied shear rate, the storage modulus is shown to be very small and increases first rapidly and then the growth rate appears to reach a constant value at longer times. After conditioning at a very small shear rate following an initial pre-shear at 25 s^{-1}, the initial storage modulus is much larger and the rate of increase with time is comparable to that observed at long times for tests carried out after a large initial shear rate. Although the rates of increase appear to be quite similar for long times, no equilibrium structure is reached after 5000 s and the modulus for the test carried out after an applied shear rate of 10^{-3} s^{-1} is more than double that obtained following the applied shear rate of 25 s^{-1}. Obviously, the resulting structures are highly dependent on the previous flow history. Note that the same structure development would be obtained if after pre-shearing at 25 s^{-1} the second shearing would have been carried out at 10^{-3} s^{-1} instead of carrying the shear rate decreasing ramp. However, the time required to reach steady-state at that low shear rate would have been much longer. Actually, this strong dependence of the structure on flow history was the motivation of the work presented here, in which we investigate in depth the evolution of the structure at rest and under flow. In all subsequent measurements, the samples were pre-sheared at 25 s^{-1} until a steady state viscosity was observed to ensure a similar initial structure for all samples. Following that pre-shearing, various rest times and/or flow conditions were imposed as discussed in the following sections.

3.4. Results

3.4.1. Structure build-up at rest

The results of Figure 3.2b can be used to evaluate the effect of the flow history on the clay structure build-up at rest. It is important to keep in mind that the storage modulus, G', of the model suspension arises only from the clay structure since the matrix is inelastic, while both of them contribute to the loss modulus, G''. Figure 3.2b shows that G' grows from an initial value, G'_i, to a time invariant value, G'_∞, following an exponential form:

$$G'(t) = G'_i + (G'_\infty - G'_i)\left(1 - \exp\left[-\left(\frac{t}{\tau}\right)^m\right]\right) \tag{3.1}$$

with m the stretching exponent, and τ the characteristic time. A similar trend was observed for G'', which was larger than G' at 125.6 rad.s^{-1}. The values of G'_i and G'_∞ are shown in Figure 3.2 to depend strongly on the initially applied shear rate, $\dot{\gamma}_i$. The stretching exponent m ($\approx$ 0.3) is nearly independent of the initial shear rate and the characteristic time τ tends to a constant value ($\approx$ 600 s). This means that the kinetics of the build-up process at rest does not depend significantly on the flow history. However, the build-up process leads to different equilibrium structures, as G'_∞ decreases from high to low plateau values for increasing $\dot{\gamma}_i$ from 10^{-1} to 7 s^{-1}. The estimated equilibrium structure, G'_∞, is quite different from that of the initial modulus, G'_i, especially for tests carried out after high initial shear rates. It should be pointed out that

the initial modulus G'_i reported in Figure 3.2 was obtained by extrapolating the experimental data of Figure 3.2b using Equation 3.1 to time zero over a time period longer than the inverse of the imposed frequency. This extrapolated value may appear questionable due to complications arising from the stress relaxation of the sample and limitations of the MCR rheometer to impose an oscillatory shear flow during the stress relaxation. However, it is interesting to note that G'_i is, within experimental error, the same as the storage modulus, $G'_{\|}$, measured at a frequency of 125.6 rad.s^{-1} using parallel superposition of SAOS to steady-shear flow at $\dot{\gamma}_i$. As expected, the storage modulus measured in parallel superposition characterizes the structure of the suspension destroyed by steady-shear flow. However, as mentioned by Moldenaers and Mewis (1993) for measurements on polymeric liquid crystals, this superposition is nontrivial due to the fast viscoelastic response with respect to instrument limitations outlined above. Following a large initial shear rate, the destroyed structure characterized by G'_i leads to a considerably weaker final structure (G'_∞) when compared to the structure obtained following a lower initial shear rate. Consequently, the equilibrium structure build-up at rest, i.e. with the Brownian motion as the main driving force, strongly depends on the flow history. The Brownian character of the build-up process is suggested by the time scale to reach the final structure, which is comparable to the rotational relaxation time of an individual clay layer ($1/D_r = 10^3$ s). To our knowledge, only Jogun and Zukoski (1996) have reported a similar dependence of G'_∞ on the shear flow history for dense kaolin suspensions, but

information on G'_i, characteristic of the initial structure following steady-shear flow, has not been presented.

An explanation for the behaviour depicted in Figure 3.2 may be provided by the large excluded volume of the clay particles in the suspension. It results in a geometrically restricted (Brownian) motion of the nanoparticles. As mentioned above, at a volume fraction of 4 %, the distance between well dispersed clay particles is shorter than their lateral dimensions. As a result, the hydrodynamic forces play a double role. Firstly, as expected for any given $\dot{\gamma}_i$, G'_i is always lower than G'_∞, i.e. the structure under flow is always less developed than that of the pseudo-equilibrium value reflecting the competition between the break-down due to the hydrodynamic forces and the build-up induced by Brownian motion. It is quite evident that the structure is destroyed more and more as the applied shear rate is increased and, hence, G'_i decreases with increasing $\dot{\gamma}_i$. Secondly, one would expect the equilibrium value for G'_∞ to be unique, therefore the decreasing value of G'_∞ with increasing $\dot{\gamma}_i$ is difficult to explain. Note that G'_i following a test at low shear rate (smaller than 0.6 s^{-1}) can be larger than the pseudo-equilibrium G'_∞ obtained after a large initial shear rate. For tests carried out at shear rates below 0.6 s^{-1}, the structure build-up is controlled not only by the Brownian motion but by small hydrodynamic forces required to overcome the effects of the large excluded volume of the particles.

Figure 3.3 reports the storage modulus as a function of frequency for the model suspension measured following different initial shear rates, themselves preceded by a pre-shearing at 25 s^{-1}. These values, obtained after a 5400 s rest time, are close to those of G'_{∞} calculated by fitting the storage modulus as a function of time (Equation 3.1). For small initial shear rates, a non-terminal flow behaviour is observed, characteristics of a weak gel, but the suspension becomes more liquid-like as the initial shear rate is increased. Finally, the modulus at the lowest applied frequency, G'_0, follows the same trend as that of G'_{∞} shown in Figure 3.2.

In the light of the previous results, it is obvious that the shear flow history of polymer nanocomposites need to be controlled if one wishes to draw some conclusions about the particle dispersion or volume fraction threshold, based on the low-frequency dependency of G'.

3.4.2. Structure build-up under flow

To assess the effect of the flow history on the structure build-up under flow, the transient shear stress, σ^-, resulting from a sudden change from a high to a low shear rate was measured (the structure break-down is investigated in the next section with sudden changes from an initial shear rate lower than the final one). This process is important because it may shed light on the previously reported observations, mainly the structure build-up observed in Figure 3.2b following pre-shearing at 25 s^{-1} down to very low shear rates. Typical transient responses for the model suspension to a stepwise

reduction in shear rate from different $\dot{\gamma}_i$ to a final value, $\dot{\gamma}_f$ of 0.1 s^{-1} are illustrated in Figure 3.4. Similar trends were observed for final shear rates ranging from 0.01 to 1 s^{-1}. The fast decrease of σ^- at short times, corresponding to the viscoelastic response of the suspension, is followed by a monotonic increase up to an equilibrium shear stress independent of $\dot{\gamma}_i$ If the structure of this suspension under steady-shear flow is shown to be independent of the shear flow history, the structure build-up under flow strongly depend on the history, in contrast to the kinetics of the build-up at rest, which does not depend significantly on the flow history, as discussed above. The observations reported in Figure 3.4 are very similar to those presented by Dullaert and Mewis (2005a, b) for fumed silica suspensions. They modified the so-called stretched exponential model to take into account the initial viscoelastic response. The empirical equation is:

$$\sigma(t) = \sigma_1 \left(\exp\left[-\frac{t}{\tau_1}\right]\right) + \sigma_2 \left(1 - \exp\left[-\left(\frac{t}{\tau_2}\right)^m\right]\right) + \sigma_3 \qquad (3.2)$$

where σ_1, and $\sigma_2 + \sigma_3$ represent the steady stress for the initial and final shear rate, respectively. The first and second terms on the right-hand side respectively describe the initial viscoelastic and thixotropic responses. The fits using this equation are shown by solid lines in Figure 3.4, but the parameters are not reported here. While the characteristic time, τ, and the stretching exponent, m, of Equation 3.1 for the structure build-up at rest are almost independent of the initial shear rate, clear dependences are observed for the thixotropic characteristic time, τ_2, and m of Equation 3.2 for the structure build-up under flow. The characteristic time τ_2 follows a power-law behaviour

with indexes equal to approximately -0.7 and 0.4 for the final shear rate, $\dot{\gamma}_f$, and initial shear rate, $\dot{\gamma}_i$, dependencies, respectively. The build-up process is mainly strain-controlled as τ_2 is nearly inversely proportional to the final shear rate. A similar power-law dependence on $\dot{\gamma}_f$ has been observed by Dullaert and Mewis (2005b) for fumed silica suspensions. As a lower τ_2 induces a faster build-up, the previous power-law indexes reflect that a faster equilibrium structure is reached starting from a more developed initial structure (low initial shear rate) and finishing with a less developed structure (large final shear rate). We note that the structure of the suspension subjected to changes in shear rate as illustrated in Figure 3.4 is represented by the storage modulus measured in SAOS as reported in Figure 3.2**Erreur ! Source du renvoi introuvable.**b and described by Equation 3.1.

The initial viscoelastic responses shown in Figure 3.4 and characterized by σ_1 in Equation 3.2 are not reliable since the filtering technique of the MCR rheometer is susceptible to influence the measurements (Dullaert and Mewis 2005b, Mackay *et al.* 1992). Instead, the fast viscoelastic relaxation upon cessation of flow was investigated using the ARES rheometer according to a suitable procedure as reported by Mackay *et al.* (1992) and more recently by Dullaert and Mewis (2005a,b). Figure 3.5 presents the shear stress relaxation function σ^- of the nanoclay suspension upon cessation of steady shear flow for different initial shear rates $\dot{\gamma}_i$. The first 28 ms of the data are ignored due to limitations of the instrument as beforehand revealed by the non-instantaneous decay of the stress observed for a Newtonian oil (not shown). Above 28 ms and up to 60 ms,

the log-linear extrapolation of σ^- to time zero (time of cessation of the steady shear flow), yields the elastic component of the steady-shear stress as the viscous stress contribution dissipates instantaneously. The curves are well described by the first term of Equation 3.2 with a characteristic time, τ_1, which is function of the initial shear rate. This elastic contribution is related to an apparent yield stress caused by the particle structure and is discussed further below.

The elastic (σ_e) and viscous (σ_v) contributions, along with the total steady stress (σ) of the nanoclay suspension are presented in Figure 3.6. The steady-shear data were obtained during a decreasing shear rate ramp using a measurement time of 200 s (no differences were noticeable for longer measurement times). Actually, the use of a decreasing shear rate allowed reaching the equilibrium state faster since the thixotropic characteristic time, τ_2, decreases when $\dot{\gamma}_i$ approaches $\dot{\gamma}_f$ as already discussed above. The steady-shear behaviour is well described by the Bingham equation:

$$\sigma = \sigma_0 + \mu_0 \dot{\gamma} \tag{3.3}$$

where σ_0 and μ_0 are the apparent yield stress and the high-shear-rate viscosity of the suspension, respectively. The apparent yield stress determined from the best fit of the experimental data is 70 Pa. The elastic contribution σ_e in Figure 3.6 increases with decreasing shear rate and represents the apparent yield stress at low shear rate (below 0.1 s^{-1}). On the other hand, the viscous contribution increases with shear rate to become larger than σ_e above a critical shear rate of 0.6 s^{-1}, leading to a purely viscous behaviour

for shear rates larger than 7 s^{-1}. The critical shear rate of 0.6 s^{-1} is relevant since, as outlined before, the structure build-up is induced not only by Brownian motion but by small hydrodynamic forces. The structural and hydrodynamic contributions to the flow curve of fumed silica suspensions follow similar trends, has previously shown by Dullaert and Mewis (2005b).

3.4.3. Structure breakdown

A similar procedure for characterizing the structure break-down under flow was used by measuring the transient stress, σ^+, for stepwise increases in shear rate.

Figure 3.7 reports the transient shear stress data of the model suspension as a function of strain for jumps from an initial shear rate, $\dot{\gamma}_i$, of 10^{-2} s^{-1} to different larger final shear rates $\dot{\gamma}_f$, Additional experiments have been carried out from different initial shear rates to a final shear rate of 1 s^{-1}, but the results are not presented here. All the results of Figure 3.7 display large overshoots located at a critical strain, $\gamma_{\sigma^+_{max}}$, before reaching a steady-state value, σ^+_∞. Starting from the same initial structure (same initial shear rate) the increasing overshoot with increasing final shear rate reflects both the elastic response of the initial structure (σ_e in Figure 3.6) and the break-down and rearrangement of the structure under flow. The rearrangement is mainly strain-controlled since $\gamma_{\sigma^+_{max}}$ is nearly independent of $\dot{\gamma}_f$. The rearrangement may include anisotropy of the microstructure and/or orientation of the nanoparticles under flow, as observed for fibre suspensions by Ausias *et al.* (1992). However, the anisotropy and the

orientation under transient flow still need to be experimentally confirmed using optical rheometry. Similar mechanisms have been proposed by Pignon *et al.* (1998) for suspensions of laponite in water.

The time-dependent changes in stresses depicted in Figure 3.7 can be described using a similar empirical equation than that used for the build-up curves (Equation 3.2). This equation (Dullaert and Mewis 2005b) is:

$$\sigma(t) = \sigma_1\left(1 - \exp\left[-\frac{t}{\tau_1}\right]\right) - \sigma_2\left(1 - \exp\left[-\left(\frac{t}{\tau_2}\right)^m\right]\right) + \sigma_3 \qquad (3.4)$$

The fits are shown by the solid lines in Figure 3.7. The parameters are not reported, but the characteristic time, τ_2, follows the same power-law dependence on the final shear rate (index equals to -0.7) as obtained from build-up experiments. Hence, the structure break-down as well as the structure build-up are mainly strain-controlled. The stretching exponent m and τ_2 dependences on the initial shear rate are also found to be similar to those observed from build-up measurements (power-law index close to 0.4).

Stepwise increases in shear rate induce breakdown of the initial structure characterized by G'_i (Figure 3.2) and shown to develop at rest to different final structures characterized by G'_∞. The stress growth behaviour of the developed structures is illustrated in Figure 3.8 for an applied shear rate of 1 s^{-1}, preceded by a preconditioning at 25 s^{-1} down to a shear rate of $\dot{\gamma}_i$, and following a rest time of 5400 s. As expected, the shear stress displays a larger overshoot as the initial structure is more developed, i.e. for low $\dot{\gamma}_i$. The overshoot, σ^+_{max}, as a function of the initial shear rate is shown in

Figure 3.8b to follow exactly the same trend as G'_{∞} (Figure 3.2) with a transition over the same $\dot{\gamma}_i$ range, with a high plateau at the lowest $\dot{\gamma}_i$ and a low one at high $\dot{\gamma}_i$. The opposite tendency is shown by the critical strain $\gamma_{\sigma^+_{max}}$, which goes from a lower plateau at the lowest $\dot{\gamma}_i$ to a higher plateau for large $\dot{\gamma}_i$, suggesting that the more developed structure breaks down at a lower strain and is therefore more fragile. Critical strain data obtained for stress growth experiments carried out at the same shear rate as the initial one, $\dot{\gamma}_i$, after a rest time of 5400 s follow the same trend (closed circles in Figure 3.8).

Figure 3.9 presents the effect of the rest time and of the applied shear rate on the overshoots for stress growth experiments carried out at the same final shear rate $\dot{\gamma}_f$ as the initial $\dot{\gamma}_i$. In this case, the stress overshoot can be entirely attributed to the breakdown and rearrangement of the structure developed during the rest time, The reduced overshoot function, $(\sigma^+_{max} - \sigma^+_{\infty})/\sigma^+_{\infty}$, from measurements carried out at 0.3 s^{-1} is shown to increase with rest time following a stretched exponential form as observed previously for the recovery of the storage modulus G' (Figure 3.2**Erreur ! Source du renvoi introuvable.**b). The reduced overshoot is observed to increase slightly with increasing shear rate confirming the findings (Li *et al.* 2003, Solomon *et al.* 2001).

3.4.4. Flow reversal

To get an insight of the anisotropy effect of the structure, flow reversal measurements have been performed. Results of consecutive stress growth experiments without rest

time are shown in Figure 3.10 for three imposed shear rates. When the initial pre-shearing is applied in the same (clockwise, CW) direction as the following applied shear rate, steady state is rapidly reached as shown by constant stress values in the figure (open symbols). However, if the direction of the pre-shearing is in the counter-clockwise (CCW) direction whereas the subsequent shear rate is applied in the CW direction, the shear stress (closed symbols) goes to very low and even negative values before increasing monotonously to finally reach the same steady-state value, σ_{∞}^{+}. At the lowest imposed shear rate of 0.03 s^{-1} for the flow reversal case, σ^{+} is first negative up to a deformation of 0.06, and is the result of the relaxation of the structure developed during the previous shear (opposite direction); afterwards, the positive value of σ^{+} is indicative of the stretching and build-up of the new structure. The σ^{+} value at time zero is approximately equal to the elastic contribution σ_e shown in Figure 3.6. At larger shear rates, the initial viscoelastic response is only partially visible due to the smaller elastic contribution and the accessible time scale of the rheometer. Even at the largest shear rate, σ^{+} does not display a reverse overshoot as observed by Sepehr *et al.* (2004) for concentrated short fibre suspensions and attributed to the tumbling of fibres.

The interpretation of the previous transient viscoelastic response is extended by investigating the reverse flows done after a rest time of 5400 s, and the results are reported in Figure 3.11. The reduced transient shear stress, $\sigma^{+}/\sigma_{\infty}^{+}$, starts from a low value since the structure relaxes during the allowed rest time. Then, $\sigma^{+}/\sigma_{\infty}^{+}$ displays a peculiar behaviour revealing a first small overshoot or shoulder and then a second

overshoot at a larger strain. The first overshoot or shoulder is located at a strain value similar to those of the overshoots observed during the stress growth experiments of Figure 3.7 and Figure 3.8. The first overshoot, clearly visible at high shear rates, must be related to the viscoelastic response and breakdown of the initial structure developed at rest. The second overshoot, seen even for low shear rates, takes place at a strain more than one decade larger than the first one. It is indicative of the structure rearrangement and build-up. By comparing the trend depicted in Figure 3.11 with that of Figure 3.8a at $\dot{\gamma} = 1\ s^{-1}$, it is obvious that the structure remains strongly anisotropic even after a long rest time. This behaviour outlines again the restricted Brownian motion, as discussed before. Our results confirms the importance of the Brownian motion on the transient behaviour, in contrast to the conclusions of Salomon *et al.* (2001), Lele *et al.* (2002) and Ren *et al.* (2003). We finally note that Salomon *et al.* (2001) reported single overshoots for the reverse flow experiments. However, the peculiar behaviour shown in Figure 3.11 may not be visible in their results because they used a linear scale for the strain. Also, the viscoelastic nature of their polymer matrix could have affected the transient responses of their nanocomposites.

3.5. Concluding remarks

The linear and non-linear viscoelastic properties of a model suspension for non-polar polymer/clay nanocomposites have been investigated taking into account the flow history. The time evolution of the viscoelastic properties reported only arise from the

structural changes of the clay structure since this model suspension is based on a Newtonian matrix.

Upon cessation of steady shear flows, different equilibrium structures are reached, which strongly depend on the pre-shear rate. A lower pre-shear rate leads to the development of a stronger equilibrium structure. It follows that the non-terminal behaviour of this model suspension is more solid-like as the pre-shear rate decreases. The existence of these different pseudo-equilibrium structures has been attributed to the large excluded volume of the clay particles. The structure build-up is controlled not only by the Brownian motion but by small hydrodynamic forces required to overcome the effects of the large excluded volume of the particles.

The build-up as well as the break-down of the clay structure under flow follow a similar kinetics described by empirical relations of stretched exponential form, which depends on the flow history, as observed for nanoparticles of fumed silica (Dullaert and Mewis 2005b). The amplitude of the stress overshoots observed during break-down measurements increases with rest time and with decreasing pre-shear rate. i.e. following the same trend as the structure described by the storage modulus measured in SAOS.

Finally, overshoots are observed for reverse stress growth experiments, but only after a long rest time, confirming the findings of (Li *et al.* 2003, Solomon *et al.* 2001). Our flow reversal results suggest a strong anisotropy of the shear induced clay structure, which persists even after a long rest time, outlining the restricted Brownian motion.

This flow reversal response as well as the other transient responses could be elucidated by following the overall orientation of the clay structure using rheo-optical methods. These will be reported in a subsequent publication.

3.6. Acknowledgements

The authors wish to thank Dr. Hojatolla Vali and Dr. Kelly Sears, from McGill University, for their precious help with the TEM experiments. Southern Clay Products kindly provided materials used in this study. One of the authors (C.M.) is thankful to Alcan Inc. for a scholarship. Finally, financial support from NSERC (Natural Science and Engineering Research Council of Canada) and from FQRNT (Fonds Québécois de Recherche en Nature et Technologies) is gratefully acknowledged.

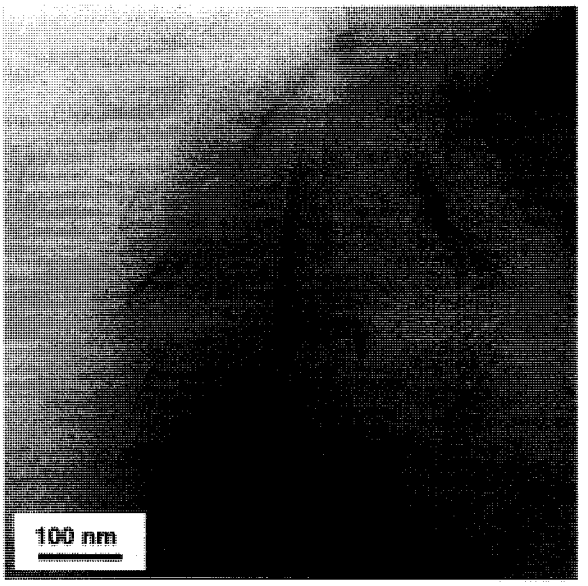

Figure 3.1 : TEM micrograph of the model suspension.

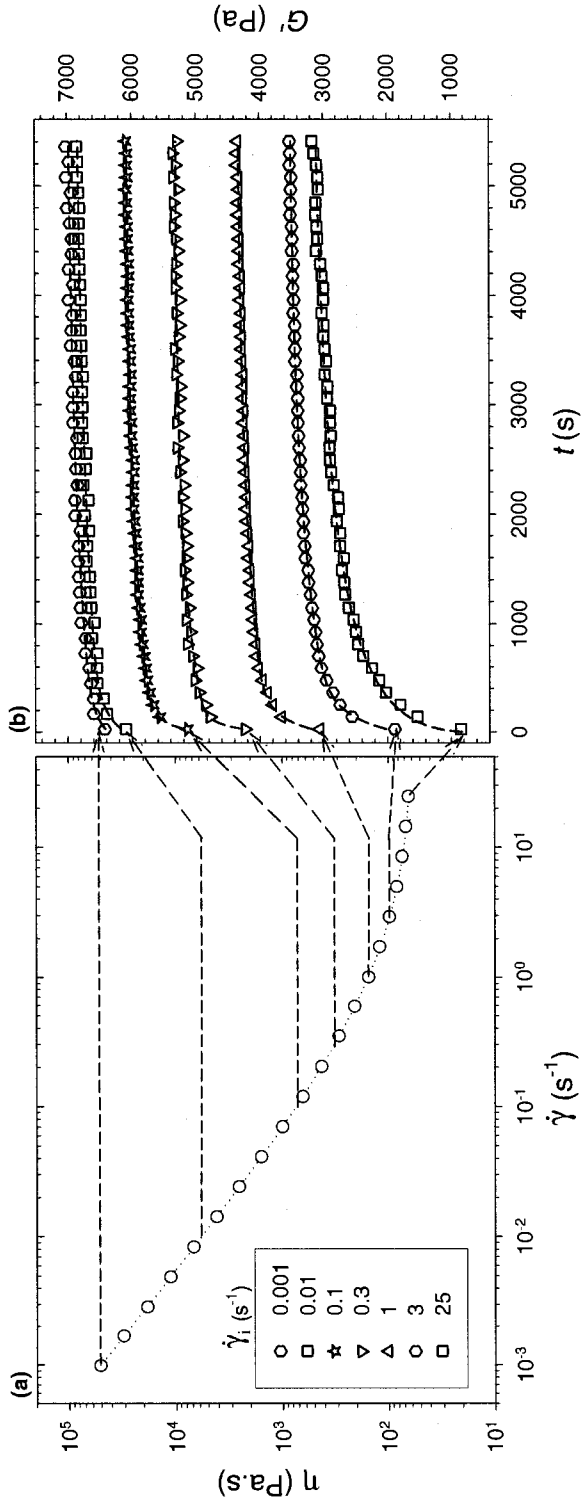

Figure 3.2 : Structure changes under preconditioning: (a) Steady viscosity η vs. shear rate $\dot{\gamma}$ and (b) storage modulus *G'* vs. time *t* at a frequency of 125.6 rad.s^{-1} upon cessation of the steady-state flow imposed in (a). Symbols indicate the values of the initial shear rate $\dot{\gamma}_i$ of the steady shear flows; the solid lines represent best fits using Equation 3.1.

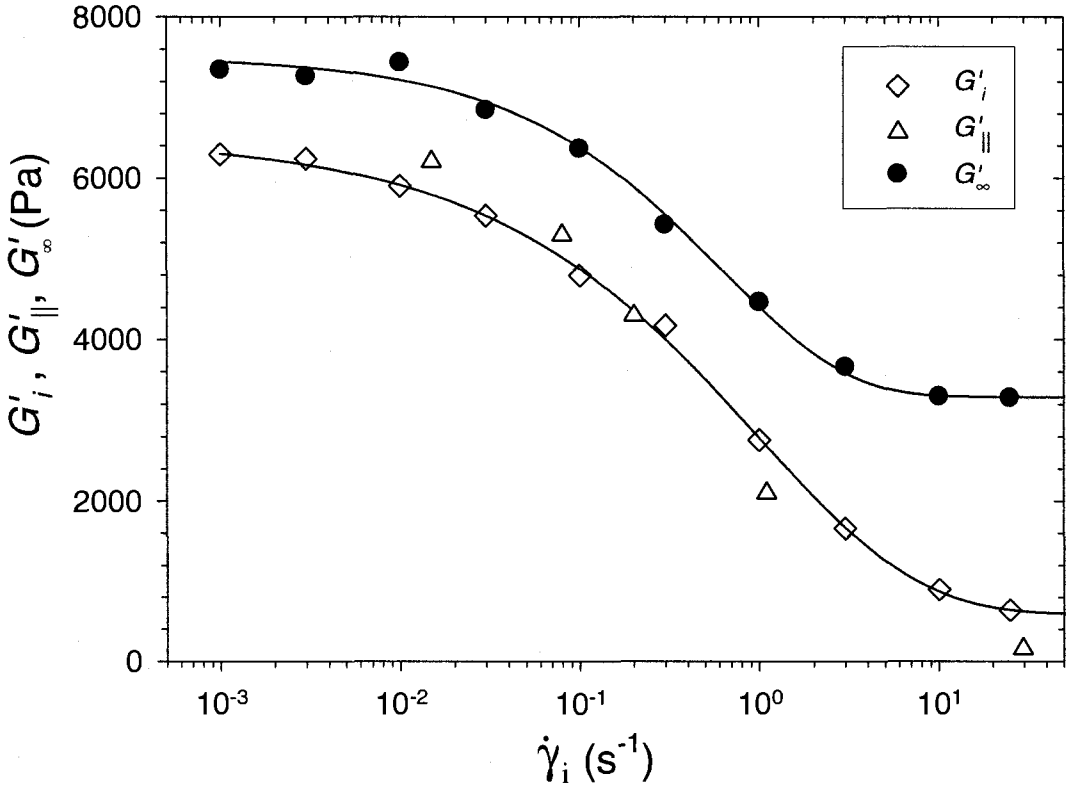

Figure 3.2 : Storage modulus parameters of Equation 3.1 vs. initial shear rate $\dot{\gamma}_i$ obtained by fitting the data shown in Figure 3.2.

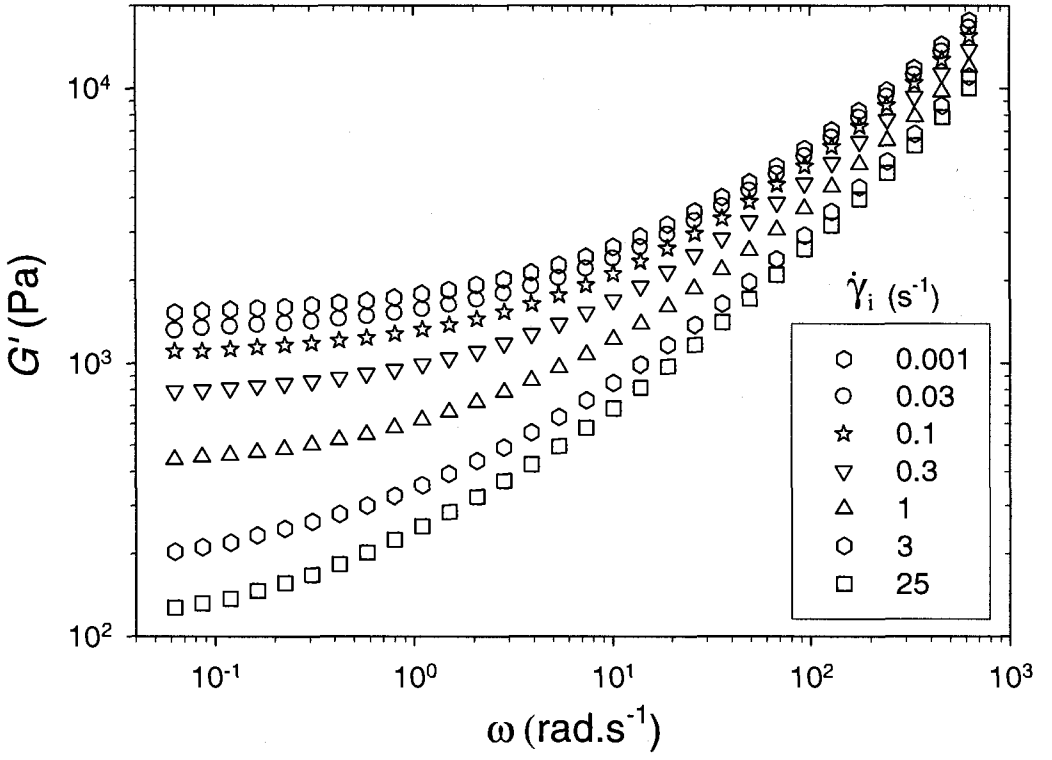

Figure 3.3 : Storage modulus G' vs. frequency ω measured after steady-shear flow at $\dot{\gamma}_i$ following a shear rate at 25 s^{-1} and rest time of 5400 s.

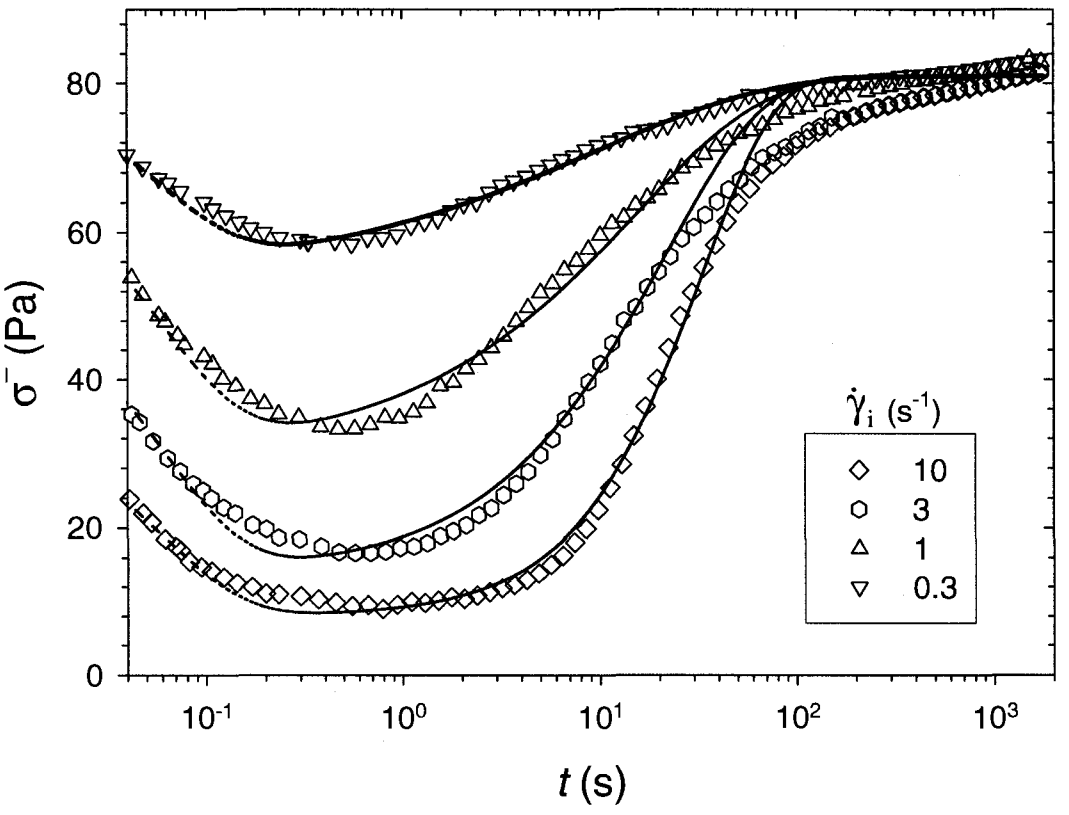

Figure 3.4 : Transient stress σ^- vs. time t after a stepwise reduction in shear rate to a final value $\dot{\gamma}_f$ of 0.1 s^{-1}. The solid lines represent best fits using Equation 3.2.

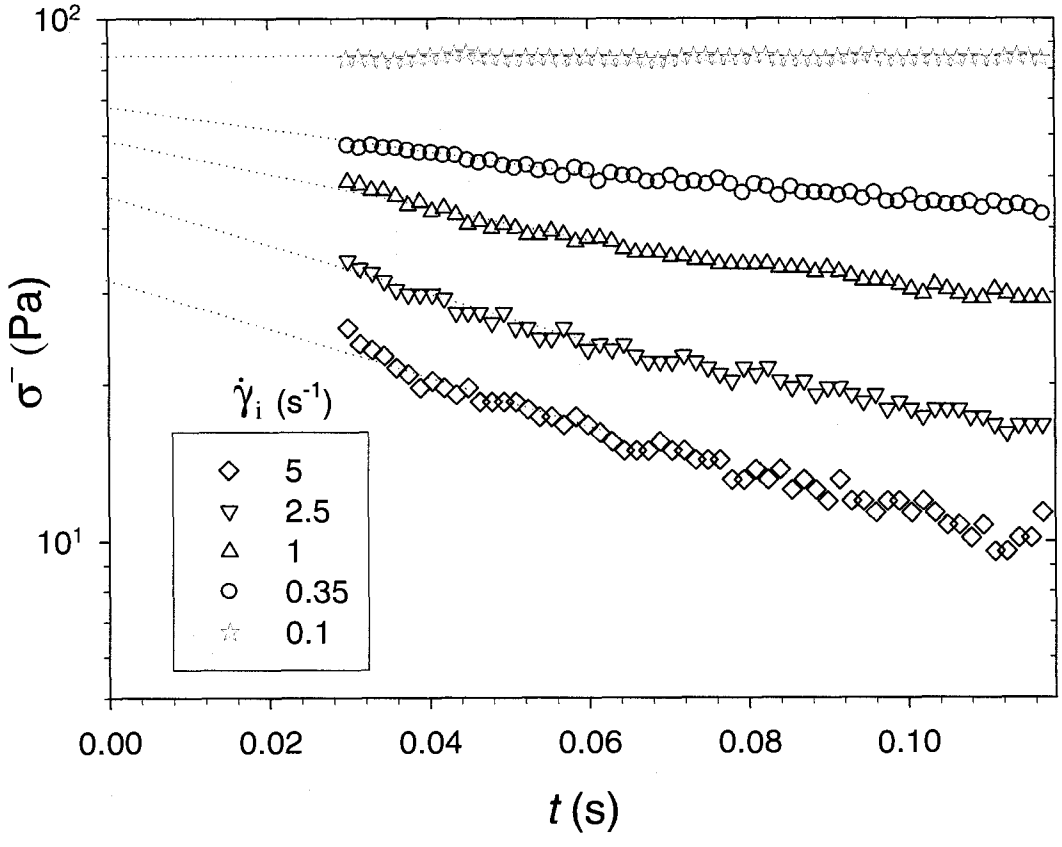

Figure 3.5 : Transient stress $\bar{\sigma}$ vs. time t upon cessation of flow after steady-state for different initial shear rates $\dot{\gamma}_i$. The solid lines represent log-linear regressions.

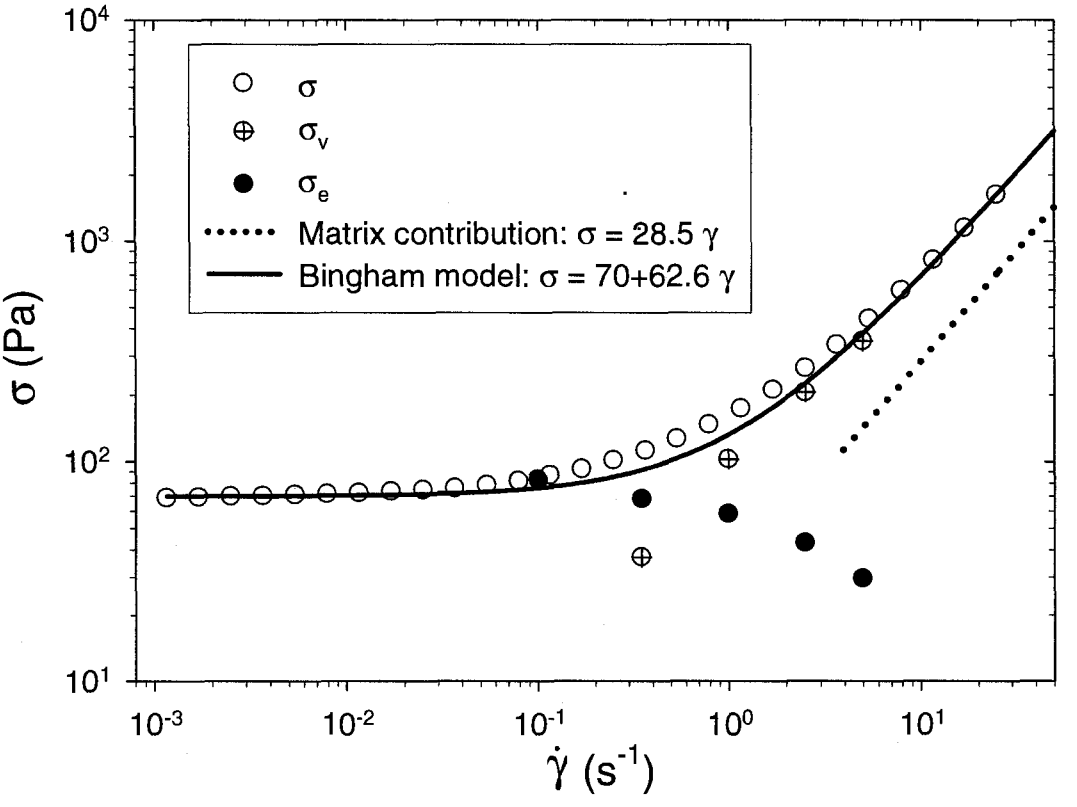

Figure 3.6 : Elastic σ_e and viscous σ_v contributions to the total steady stress σ vs. $\dot{\gamma}$. Dotted and solid lines represent the matrix contribution and the best fit using Equation 3.3, respectively.

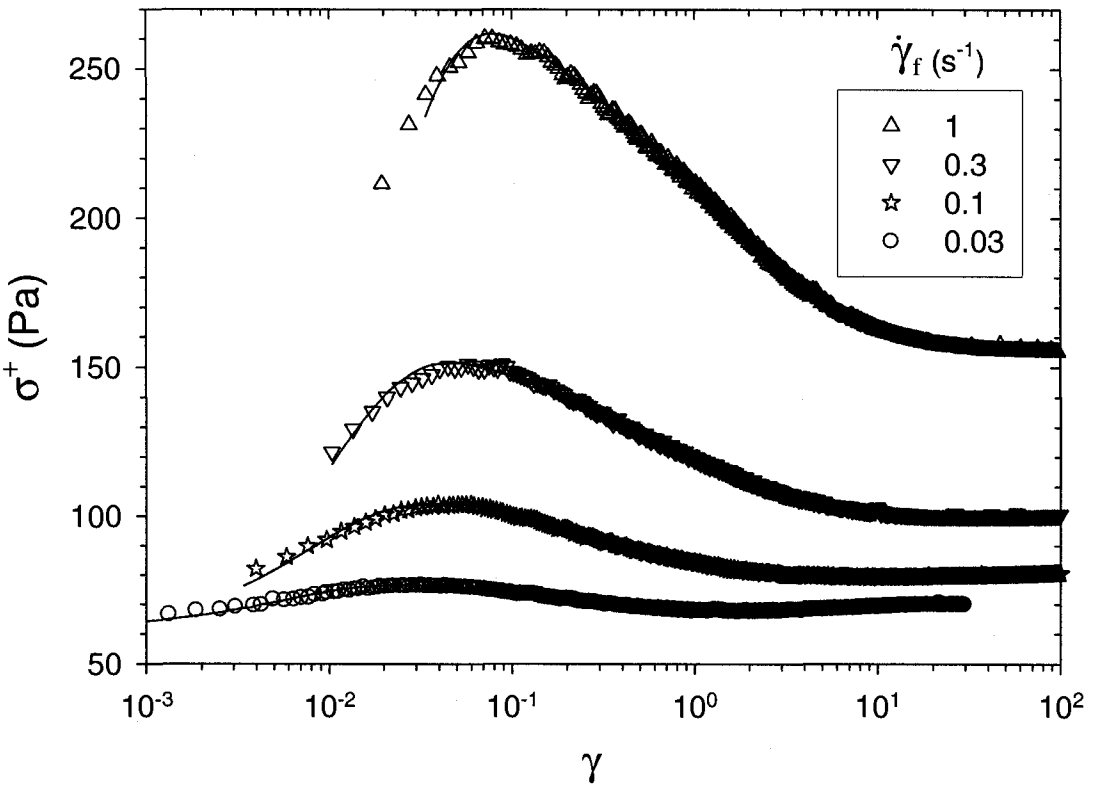

Figure 3.7 : Transient stress σ^+ vs. γ for stepwise increases in shear rate from an initial $\dot{\gamma}_i = 0.01\ s^{-1}$ to different shear rates. The solid lines are the best fits using Equation 3.4.

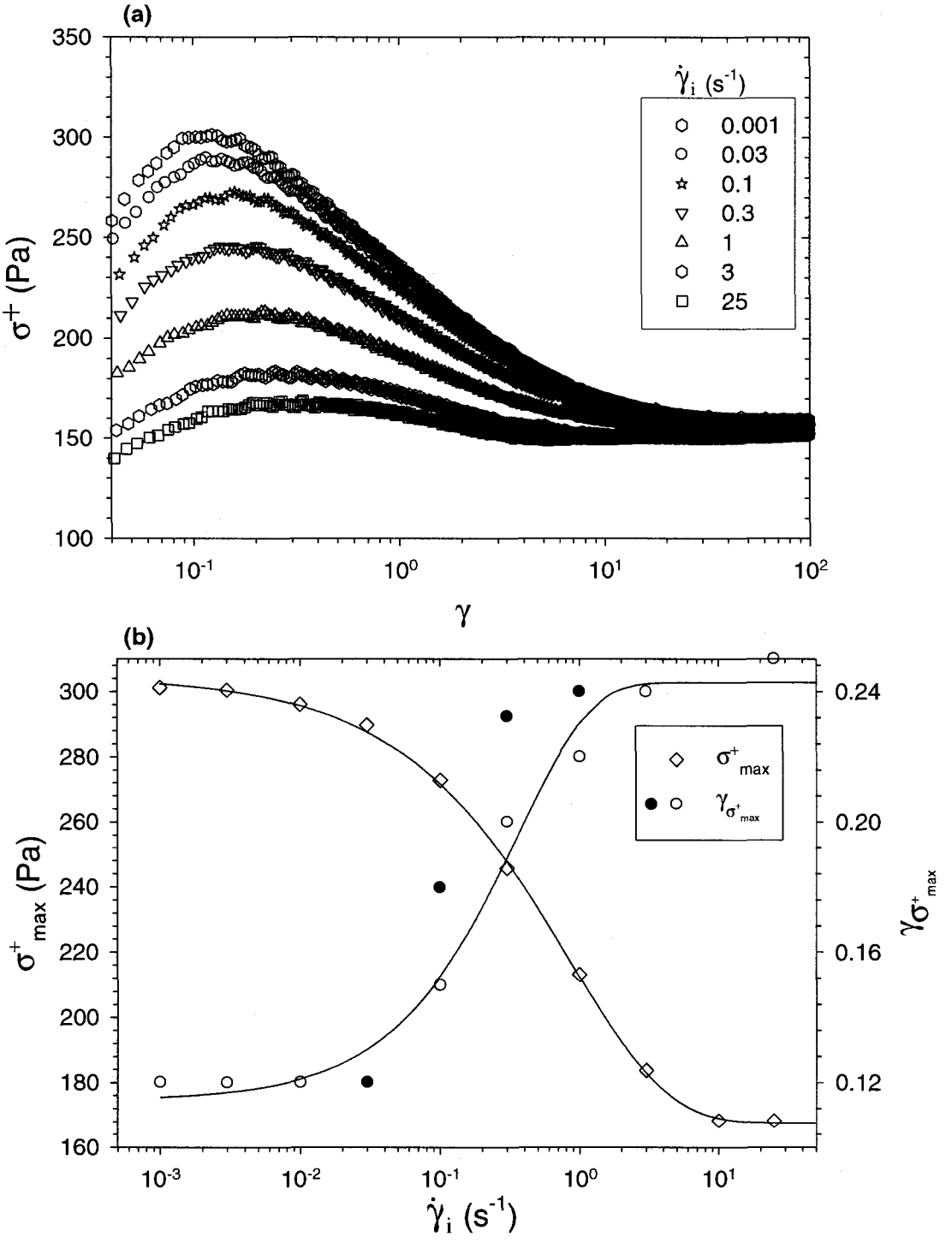
(a)
350
300
250
200
150
100
σ+ (Pa)
10-1
100
101
102
γ
γ̇i (s-1)
0.001
0.03
0.1
0.3
1
3
25
(b)
300
280
260
240
220
200
180
160
σ+max (Pa)
0.24
0.20
0.16
0.12
γσ+max
10-3
10-2
10-1
100
101
γ̇i (s-1)
σ+max
γσ+max

Figure 3.8 : Stress growth behavior for the model suspension. (a) transient stress σ^+ vs. strain γ for stress growth experiments carried out at 1 s^{-1} after a rest time of 5400 s, following a preconditioning at 25 s^{-1} and down to a shear rate of $\dot{\gamma}_i$, (b) transient stress overshoot σ^+_{max} and critical strain $\gamma_{\sigma^+_{max}}$ vs. initial shear rate $\dot{\gamma}_i$ after a rest time of 5400 s (open circles for $\dot{\gamma}_f$ = 1 s^{-1} and closed symbols for $\dot{\gamma}_f = \dot{\gamma}_i$). The lines are drawn to guide the eyes.

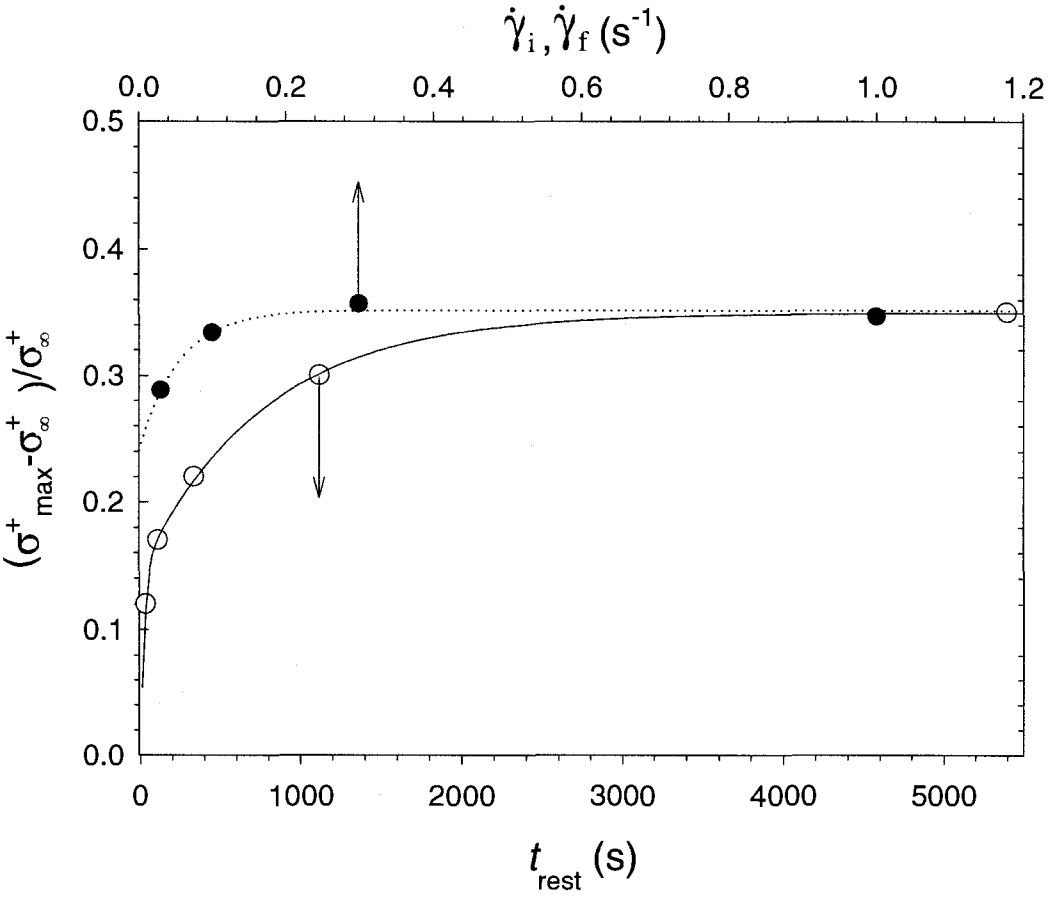

Figure 3.9 : Reduced stress overshoot $(\sigma^+_{max} - \sigma^+_\infty)/\sigma^+_\infty$ vs. rest time t_{rest} ($\dot{\gamma}_f = \dot{\gamma}_i = 0.3$ s^{-1}) and vs. shear rate $\dot{\gamma}_f = \dot{\gamma}_i$ after a rest time of four consecutive experiments carried out at the same shear rate.

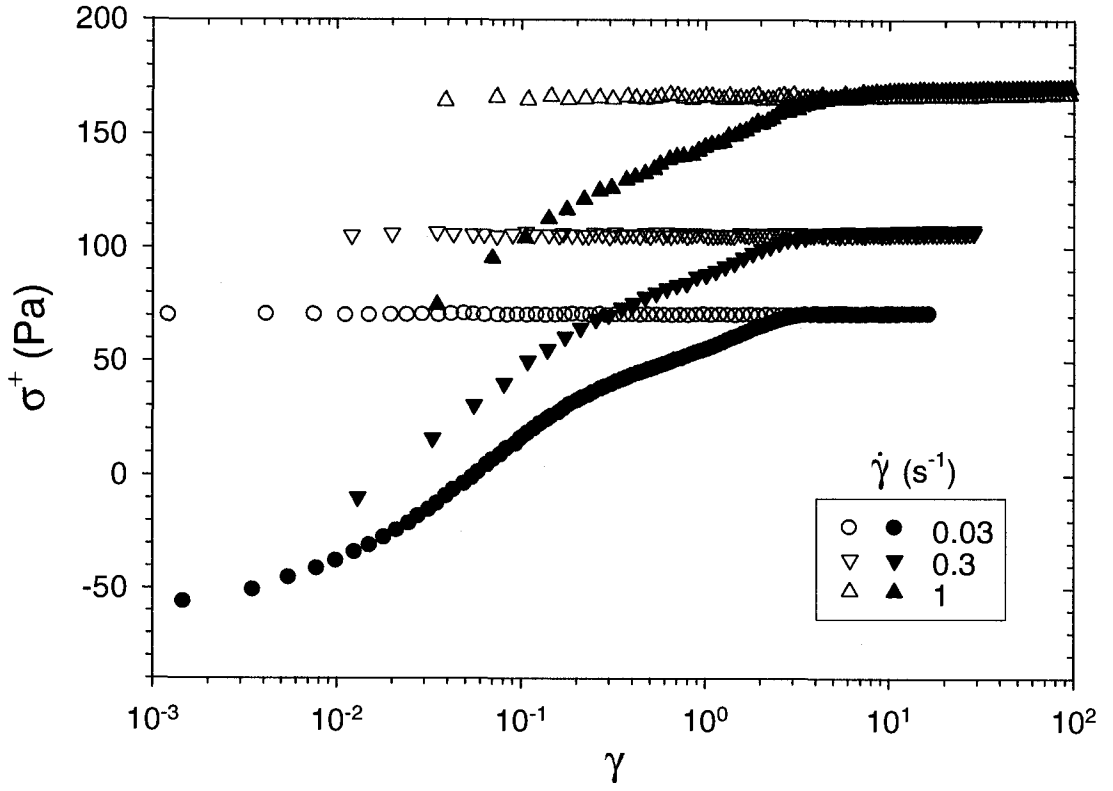

Figure 3.10 : Transient stress σ^+ vs. strain γ for consecutive stress growth experiments following a pre-shearing in the same (CW) direction and in the opposite (CCW) direction.

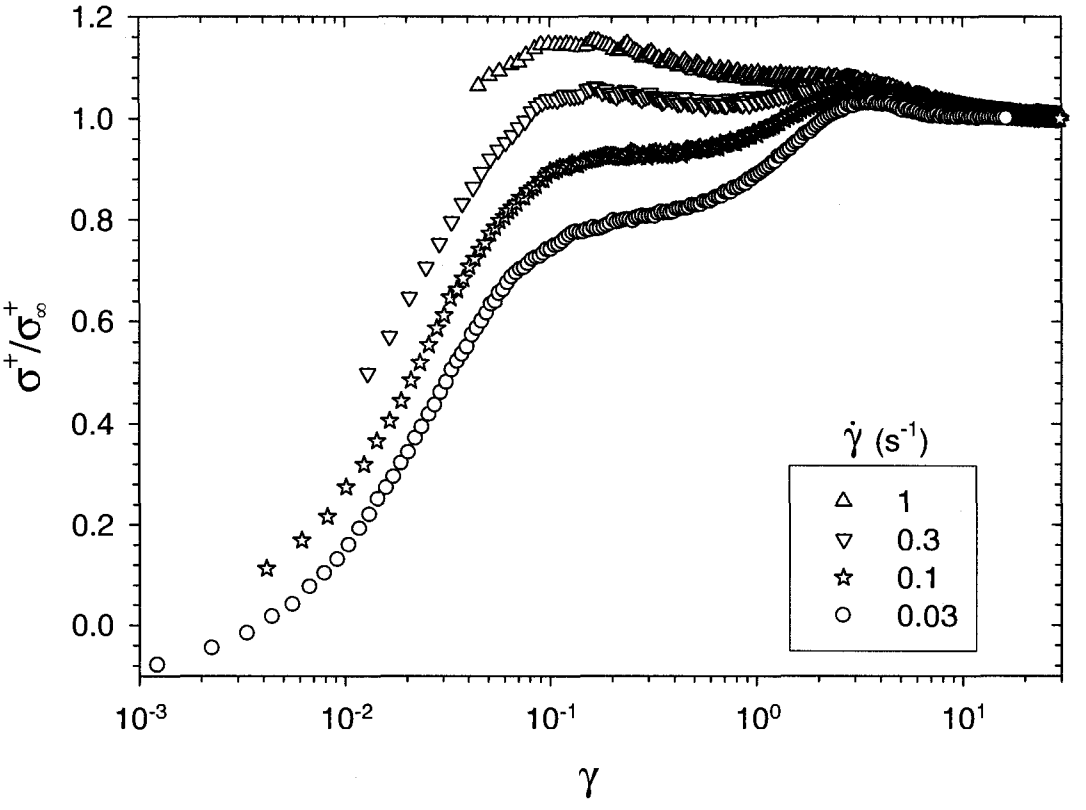

Figure 3.11 : Reduced transient shear stress σ^+/σ^+_∞ vs. strain γ for stress growth experiments following a pre-shearing in the opposite (CCW) direction and a rest time of 5400 s.

CHAPITRE 4 - ARTICLE: ANISOTROPY OF NON-AQUEOUS LAYERED SILICATE SUSPENSIONS SUBJECTED TO SHEAR FLOW

Christophe Mobuchon, Pierre J. Carreau and Marie-Claude Heuzey

Center for Applied Research on Polymers and Composites (CREPEC), Chemical Engineering Department, Ecole Polytechnique, PO Box 6079, Stn Centre-Ville, Montreal, QC, Canada H3C3A7

Naveen Krishna Reddy, Jan Vermant

Department of Chemical Engineering, K.U. Leuven, de Croylaan 46, B-3001, Heverlee, Belgium

4.1. Abstract

The flow-induced orientation of non-equilibrium and metastable structures of non-aqueous layered silicate suspensions is probed by combination of light scattering and advanced rheometric measurements, including two dimensional amplitude oscillatory

---

Cet article a été présenté en partie lors de la 4^{ième} conférence annuelle de l'European Society of Rheology (A.E.R.C.) et soumis à la revue Journal of Rheology

shear flow (2D-SAOS). The self-similar nature of the non-equilibrium and metastable structures was inferred from the small angle light scattering (SALS) patterns. Furthermore, linear dichroism measurements were used to study distinct orientational mechanisms of these silicate dispersions. At first, structural orientational changes were observed in the vorticity plane with anisotropy and orientation that developed in the same range of shear rates as the shear-thinning behavior of the suspensions. Once the viscosity plateau is reached at high shear rates, a second minor change in the anisotropy is detected in the velocity gradient plane. Upon cessation of flow, the lack of orientational recovery was explicitly shown with the 2D-SAOS experiments. Actually, this new technique proved to be sensitive to the anisotropic nature of the microstructure of organoclay suspensions. As a result of the flow induced orientation, the transient response of the non-aqueous layered silicate suspensions is shown to imply both structural and orientational contributions.

4.2. Introduction

Colloidal suspensions exhibit a wide range of complex rheological properties including transition from fluid-like to solid-like behavior leading to nonlinear rheological properties and thixotropic phenomena (Barnes 1997, Mewis 1979). This complex behavior stems from the self-organization of the colloidal particles on multiple length scales (Hoekstra *et al.* 2005, Pignon *et al.* 1997a). The representation of their inner structure requires description of both spatial and orientational distributions of the

dispersed phase over length scales ranging from the particle size (a few nanometers) to the macroscopic scale. The understanding of the flow-induced changes in the multi-scale structure is relatively well understood for colloidally stable suspensions, whereas for aggregated colloidal suspensions an understanding of flow effects on the size, particle shape, density, and anisotropy of aggregates is only gradually emerging (Vermant and Solomon 2005).

Layered silicates of the smectite group, commonly used as rheological modifiers in paints, ceramic additives, inks, drilling fluids and greases, have attracted a great interest in the emerging field of polymer nanocomposites (Patel *et al.* 2006). Their ordering at the nanometer length scale leads to unique mechanical, electrical, optical and thermal properties (Ray and Okamoto 2003). The most commonly used smectite is the montmorillonite for which the individual layers are typically 1.2 nm thick, 320–400 nm long and 250 nm wide (Cadene *et al.* 2005). Non-aqueous suspensions based on layered silicates are expected to belong to the aggregated suspensions class. While many studies have reported the structure of aqueous layered silicate suspensions, there have been fewer investigations of their non-aqueous counterparts. In the following, the extensive literature on the aqueous layered silicate suspensions is at first reviewed. The discussion focuses on the investigations for which the physicochemical parameters were chosen to lead to attractive suspensions as in the non-aqueous case investigated in this study.

4.2.1. Inorganic smectite suspensions

At medium ionic strength, where the particles become weakly attractive, aqueous smectite suspensions undergo a sol-gel transition. In the case of laponite suspensions (~1 nm thick, average diameter of ~30 nm), the physical structure of the gel state has been probed using scattering techniques over multiple length scales ranging from the particle size (nanometer) to the micrometer scale (Morvan *et al.* 1994, Mourchid *et al.* 1995, Pignon *et al.* 1998, Pignon *et al.* 1997a, Pignon *et al.* 1997b, Ramsay and Lindner 1993, Ramsay *et al.* 1990). At small length scales, dense aggregates are formed by the combination of subunits of oriented layers (Morvan *et al.* 1994, Mourchid *et al.* 1995, Pignon *et al.* 1997a), while at larger scales, of the order of 1 μm, a fractal network emerges from these dense aggregates (Pignon *et al.* 1997a). The fractal dimension of the network is governed by the physicochemical parameters of the suspension. In turn, the fractal nature of the system controls the rheological behavior of the gel, at least at sufficiently low volume fractions. Indeed, the fractal dimension of the network has been shown by Pignon *et al.* (1997a) to be related to the yield stress. To our knowledge such investigations have not been performed on montmorillonite gel. However, direct visualization using silicon fluorescence X-ray microscopy has revealed the existence of large-scale structures much larger than the individual montmorillonite layers (Bihannic *et al.* 2001).

Under shear flow conditions, the formation of elongated rollers of aggregates arranged perpendicularly to the flow direction has been inferred by Pignon *et al.* (1997b, 1998) from an observed anisotropic butterfly-like static light scattering (SLS) pattern. Indeed, this peculiar pattern denotes spatial concentration fluctuations at large scale in the direction of the shear flow. The formation of roller-like structures has been reported from the direct microscopic visualization of attractive emulsions (Montesi *et al.* 2004) and for organic carbon nanotube suspensions (Lin-Gibson *et al.* 2004, Ma *et al.* 2007) in (confined) shear flow. Beyond a critical shear rate, this characteristic SLS pattern is replaced by an isotropic one indicating the breakdown of the large anisotropic structure into smaller aggregates (Pignon *et al.* 1998, Pignon *et al.* 1997b). Analogous light scattering patterns are also displayed by organic gels based on spherical particles of silica (Degroot *et al.* 1994, Hoekstra *et al.* 2005, Varadan and Solomon 2001, Verduin *et al.* 1996), immiscible polymer blends with viscoelastic asymmetry in the melt components (Hobbie *et al.* 2002) and semi-dilute polymer solutions that undergo shear-induced phase separation (Moses *et al.* 1994). The mechanism leading to butterfly patterns is attributed by Hoekstra *et al.* (2003, 2005) to the directional dependence of break-up and aggregation of agglomerates, while Hobbie *et al.* (2004) maintain that it can arise as a consequence of elastic effects. Finally, for aggregated suspensions, only a partial relaxation of the large scale anisotropy is observed after cessation of shear (Hoekstra *et al.* 2005, Mohraz and Solomon 2005, Pignon *et al.* 1998, Varadan and

Solomon 2001, Verduin *et al.* 1996) and denotes the lack of restoring forces to evolve toward isotropy (Mohraz and Solomon 2005, Verduin *et al.* 1996).

4.2.2. Organic smectite suspensions

In an organic fluid and depending on its polarity, the inherent attractive interactions between clay layers can be overcome by coating their surface with short hydrocarbons (organo-modification). Depending on the strength of the remaining attractive interparticle forces, the resulting sterically stabilized organoclay suspensions can belong to the class of either weakly or strongly aggregated suspensions, and in other cases, to the ideal class of ''hard'' Brownian platelets. ''Hard'' refers here to suspensions for which non-steric interactions are negligible relative to Brownian motion effects. The relative weakness of the non-steric interactions between the clay layers favors their dispersion. In reality, complete exfoliation is rarely achieved and a preserved stacking of layers leading to tactoid structures and aggregates has been observed (see for instance Li *et al.* (2003).) Small length scale spatial correlations are usually revealed using transmission electron microscopy (TEM), scattering techniques including small and ultra small-angle neutron scattering (SANS and USANS) (Hanley *et al.* 2003, Ho *et al.* 2001, King *et al.* 2007, Yoonessi *et al.* 2005), and more extensively wide and small angle X-ray scattering (SAXS and WAXS) (see for instance Vaia *et al.* (2002)). To our knowledge, the spatial organization of clay tactoids and aggregates in organic suspensions at large scale have not been investigated using light

scattering as in the case of aqueous clay gels. Finally, recent investigations using confocal laser microscopy to investigate clay suspensions seem promising for probing their real-space structures (Langat *et al.* 2006, Yoonessi *et al.* 2004).

4.2.3. Objective

We have recently reported (Mobuchon *et al.* 2007) the effect of flow history on the rheological properties and structural recovery of organo-modified montmorillonite suspensions. In contrast to published results for colloidal suspensions (Pignon *et al.* 1998), we have observed that upon cessation of steady shear flow different structures at rest were reached, depending on the pre-shearing history. The aim of the present study is to describe the complex nature of these different metastable structures and more specifically to define their anisotropic nature. The origin of the anisotropy is investigated using 2D-static light scattering and linear dichroism measurements under flow. In the system under investigation, changes in the linear dichroism can arise from both form and intrinsic dichroism contributions, hence reflecting aggregate organization and orientation as well as orientation of the individual platelets.

In addition, a structural-destructive testing based on stress growth measurements in forward and reverse directions has been performed to highlight the extent of the structural anisotropy and its effects on the nonlinear rheological properties. Subsequently, the results of a rheological non-destructive testing using a novel two-dimensional small amplitude oscillatory shear flow method (2D-SAOS) are presented.

It has been achieved by synchronizing small amplitude in parallel and orthogonal oscillatory motions, to the steady shear flow direction. In this way, the viscoelastic moduli can be obtained in all the directions of the shear plane leading to a measure of the anisotropy of the metastable colloidal structures. Measurement of viscoelastic properties in the orthogonal direction has been achieved on other systems (De Cleyn and Mewis 1987, Mewis and Schoukens 1978, Simmons 1966, Vermant *et al.* 1998, Walker *et al.* 2000, Zeegers *et al.* 1995) but, to our knowledge, used only once to assess the structural anisotropy of lyotropic liquid crystalline polymers (Walker *et al.* 2000).

4.3. Materials and methods

4.3.1. Materials

The organoclay suspension of this investigation is based on an organomodified montmorillonite (Cloisite® 15A, Southern Clay Products). The organophilic clay particles were dispersed in a non-polar Newtonian blend of polybutenes (Indopol, BP), with a viscosity of 28.5 Pa.s at 25 °C. All measurements were performed using a suspension containing a volume fraction of organoclay, ϕ_v, of 0.04, except for the optical measurements that were carried out at 0.01 and 0.03. Details about the preparation of the suspensions and results from conventional linear and non-linear rheometry are reported elsewhere (Mobuchon *et al.* 2007).

4.3.2. Optical measurements

a) Small angle light scattering

The parallel plate flow cell of a stress-controlled rheometer Physica MCR300 (Anton Paar) can be combined with a setup for time-resolved flow small angle scattering. A 10 mW He-Ne laser was used as the light source. The light beam was sent through the sample along the velocity gradient direction by means of a set of prisms. Using a combination of two half convex lenses and a beam stop and one achromatic lens, the 2D scattering patterns were focused directly onto the chip of a 12-bit IEEE 1394 -based digital camera (ORCA-285, Hamamatsu) (Cumming *et al.* 1992). Images were analyzed with in-house developed software (SalsSoftware, KU Leuven). The scattering pattern anisotropy, A, is quantified based on the eigenvalues of the second-order moment tensor of the intensity distribution (Johnson and Fuller 1988):

$$A = \frac{\sqrt{[\sum I(x,y)xx - \sum I(x,y)yy]^2 + 4[\sum I(x,y)xy]^2}}{I} \qquad (4.1)$$

where $I(x,y)$ is the intensity at the pixel coordinates (x,y) and I is the total intensity. Typically, scattering angles in the light scattering experiments lie between 3° and 20°. In real space, this corresponds to sizes of approximately 0,5-10 μm (λ = 632.8 nm).

b) Linear dichroism

When light propagates through a sample, its polarization state is altered by the refractive index tensor, $\boldsymbol{n} = \boldsymbol{n'} + i\boldsymbol{n''}$, of the material (Fuller 1995). The real part, $\boldsymbol{n'}$,

modifies the phase of light polarization and the imaginary part, n'', induces attenuation. Anisotropy in these tensors gives rise respectively to the birefringence, $\Delta n'$, and the dichroism, $\Delta n''$, defined as the difference between their principal real and imaginary indices. The dichroism is comprised of a conservative dichroism, which arises from the anisotropic scattering of light, and of a consumptive dichroism which expresses the anisotropic absorption of light. The conservative dichroism can be isolated by selecting the wavelength of light, λ, in such a way that no significant absorption occurs. It has successfully been used to follow the degree of alignment and average orientation angle of dilute suspensions of anisotropic particles in shear flows (Frattini and Fuller 1984, Johnson *et al.* 1985, Johnson and Fuller 1988, Johnson *et al.* 1990). In these cases, the measured dichroism resulted from the anisotropy of the scatterer itself (intrinsic contribution). Dichroism induced by the spatial arrangement of the scatterers (form contribution) has also been measured to follow the flow induced structure of hard-sphere suspensions (D'Haene *et al.* 1993, Lee *et al.* 1999, Wagner *et al.* 1988) and more recently of sticky sphere suspensions (Hoekstra *et al.* 2005).

The optical train used to measure the dichroism is based on a field effect modulator as proposed by Frattini *et al.* (1984). It operates by sending a modulated polarization vector of light into the sample. The modulation of the light source (10 mW He-Ne laser, λ = 632.8 nm) is achieved using a combination of a Glan-Thomson polarizer (Newport), a photoelastic modulator (Beaglehole Instruments), and a zero order quarter wave plate (Newport). The resulting polarization state generator induces the

polarization vector of the light source to rotate at a frequency and amplitude prescribed by the photoelastic modulator. The modulated light is then sent through the sample by a set of prisms. The transmitted intensity is measured using a sensitive photodiode (Beaglehole Instruments). Its harmonic analysis is performed by two phase lock-in amplifiers (SR830, Stanford Research Systems) to determine the dichroism intensity $\Delta n''$ and the orientation angle χ of its major axes relative to the shear flow direction. Actually, using the appropriate Müller matrices, the transmitted intensity is shown to have the following Fourier expansion (Frattini and Fuller 1984, Pellens *et al.* 2005):

$$I = I_{DC} + I_{\omega} sin(\omega t) + I_{2\omega} cos(2\omega t) + \cdots \tag{4.2}$$

with

$$I_{\omega} = 2J_1(A) tanh\left[\frac{2\pi\Delta n'' d}{\lambda}\right] sin(2\chi) I_{DC} \tag{4.3}$$

$$I_{2\omega} = 2J_2(A) tanh\left[\frac{2\pi\Delta n'' d}{\lambda}\right] cos(2\chi) I_{DC} \tag{4.4}$$

where J_m are Bessel functions of the m^{th} order with the amplitude, A, of the photoelastic modulator adjuster to have $J_0(A) = 0$. I_{DC} is the DC component of the light intensity and d is the sample thickness. Once I_{DC}, I_{ω} and $I_{2\omega}$ are known, they can be used to solve for the dichroism and its orientation angle.

Two flow cells mounted on the stress-controlled rheometer (Anton Paar, Physica MCR 300) were used to examine the optical anisotropy in two different planes of the flow field. With the parallel disk flow cell, the light was sent parallel to the velocity gradient

direction so that the electric vector sampled the velocity gradient plane. For the Couette cell, the light propagated along the vorticity axis leading to the measurement of optical anisotropies in the vorticity plane. The parallel disk flow cell consisted of two disks in borosilicate glass. The Couette geometry had an inner bob of 26.7 mm with a gap of 2 mm and a sample height of 16.5 mm.

4.3.3. Mechanical measurements

a) Destructive testing

As a first way to mechanically probe the anisotropy of the metastable clay structures, various interrupted forward flow and flow reversal experiments were carried out. Tests with and without time delay between the pre-shearing and the stress growth experiments were performed. These experiments were carried out using a stress-controlled rheometer (Anton Paar, Physica MCR 501) equipped with a cone-and-plate geometry (radius of 25 mm and cone angle of 0.04 rad). The data were considered only after a period of 0.04 s, the time required to reach the specified shear rate within an error of less than 2 %.

b) Non-destructive testing

The structural non-destructive testing consisted in extending the conventional linear viscoelastic measurements upon cessation of flow to two dimensions. In the present work, 2D-SAOS measurements were made to obtain the viscoelastic properties in all

directions, ranging from parallel to orthogonal directions with respect to the steady shear flow direction. The variations of the moduli with respect to the angle between the previous flow history and the oscillatory flow, directly probe the presence of any structural anisotropy. The 2D-SAOS measurements and the orthogonal superposition measurements were carried out using a strain-controlled rheometer (ARES, Rheometric Scientific) using a specially designed double-wall Couette cell (dimensions reported in Table 1), which is open at the bottom to minimize pumping flows. The bi-directional flow field was imposed by coupling the axial, γ_z, and conventional angular, γ_θ, oscillatory deformations:

$$\gamma_r = 0, \tag{4.5}$$

$$\gamma_\theta = \gamma_\theta^0 \sin(\omega t), \tag{4.6}$$

$$\gamma_z = \gamma_z^0 \sin(\omega t + \delta_\gamma), \tag{4.7}$$

with ω the applied angular frequency. The oscillatory motion is characterized by the relative amplitudes γ_θ^0 and γ_z^0, and the phase lag, δ_γ, between the angular and axial deformations. When the two deformations are in phase, i.e, $\delta_\gamma = 0$, the resulting oscillatory deformation is unidirectional, with an amplitude given by $\sqrt{\gamma_\theta^{0\,2} + \gamma_z^{0\,2}}/2$, and oriented at an angle $\varphi_{z\theta} = arctan(\gamma_\theta^0/\gamma_z^0)$ from the perpendicular direction. The resulting stress response is calculated from the components in the θ and z directions in the same manner as the deformation, and its harmonic analysis leads to the viscoelastic

moduli at a given angle $\varphi_{z\theta}$. With $\delta_\gamma = \pi/2$ and $\gamma_\theta^0 = \gamma_z^0$, the oscillatory deformation becomes two-dimensional, scanning circularly the shear plane. The two-dimensional oscillatory shear with phase lag (2D-SAOS δ_γ) is more suitable for transient measurements since it scans the entire shear plane in a single period. The general observation of the resulting 2D stress gives a direct insight into the structural anisotropy. Moreover, the investigation of the phase lags, δ_θ and δ_z, between the strain and stress components allows discriminating the elastic, σ_e and viscous, σ_v, contributions to the resulting total shear stress, σ. For an anisotropic viscoelastic material, σ can be written as follows:

$$\sigma_r = 0, \tag{4.8}$$

$$\sigma_\theta = \sigma_\theta^0 \sin(\omega t + \delta_\theta), \tag{4.9}$$

$$\sigma_z = \sigma_z^0 \cos(\omega t + \delta_z), \tag{4.10}$$

which, by splitting up its in phase and out of phase components with the imposed strain, leads to:

$$\sigma_e = \sqrt{\left(\sigma_\theta^0 \cos(\delta_\theta)\sin(\omega t)\right)^2 + \left(\sigma_z^0 \cos(\delta_z)\cos(\omega t)\right)^2}, \tag{4.11}$$

$$\sigma_v = \sqrt{\left(\sigma_\theta^0 \sin(\delta_\theta)\cos(\omega t)\right)^2 + \left(\sigma_z^0 \sin(\delta_z)\sin(\omega t)\right)^2}. \tag{4.12}$$

The corresponding elastic and storage moduli can then be obtained by dividing respectively σ_e and σ_v by the applied strain amplitude, γ^0.

Vibrating the inner cylinder axially provided the oscillatory deformation, γ_z. Its displacement is driven by the normal force rebalanced transducer (FRT) of the ARES rheometer (Vermant *et al.* 1997). In its regular mode, the ARES rheometer uses a control loop to compensate the displacement of the transducer induced by the normal force. This control loop was modified to force the normal force transducer to follow the axial position from the signal supplied by a frequency generator composed of a data card (NI PCI-6221 DAQ, National Intruments) and a LabVIEW (National Instruments) routine. Strain amplitudes in the range of $5x10^{-4}$ up to $5x10^{-2}$ could be applied. The pumping flow induced by the axial motion of the inner cylinder was minimized by some openings at the bottom of the wall (Simmons 1966, Vermant *et al.* 1997). These openings allow the fluid squeezed under the inner cylinder to flow back and forth between the gap of the cylinders.

The angular oscillatory deformation, γ_θ, was achieved by rotating the outer cylinder with the servo-controlled motor of the ARES rheometer. This motor was also controlled by the same LabVIEW-controlled frequency generator to ensure synchronisation of the axial and angular deformations.

The resulting force and torque signals were measured directly on their respective control board and analysed using a LabVIEW routine based on the fast Fourier transform (FFT) for the frequency analysis. The contributions from the instrument (inertia, friction and elasticity of the transducers) and the sample inertia on the force and torque signals were sufficiently small and did not need to be taken into account

(results shown below for the neat polybutene). Measurements for the neat polybutene were conducted at a constant strain of 0.025, while a smaller deformation of 0.01 was used for the organoclay suspensions.

All the previous optical and mechanical measurements were carried out at ambient conditions (≈ 20 °C), except for the transient non-linear measurements that were done at 25 °C. The reproducibility of the data was estimated to be within ± 2 and ± 9 % for shear rates of 25 and 0.001 s^{-1}, respectively. For dynamic measurements, the standard deviation was estimated to be within ± 5 %.

4.4. Results

4.4.1. Flow-induced anisotropy of non-equilibrium and metastable organoclay structures

a) Small angle light scattering

Small angle light scattering (SALS) measurement allows probing the micro-scale structural evolution under shear flow. After carefully loading the material between the plates, the scattering pattern was found to be isotropic. The power-law decay of the scattered intensity, I, along the flow and vorticity directions with the scattering vector, q, suggests that the structure is self-similar. The fractal dimension, D_f, is given by the minus of the power-law exponent and is equal to 2. Subjecting the clay suspensions to shear flow resulted in anisotropic SALS patterns. For shear rates from 0.1 to 100 s^{-1} the

isocontour plots are shown in Figure 4.1 (ϕ_v = 0.03, ambient temperature, exposure time 0.1s). Under shear flow, a slight anisotropy appears, with two apparent lobes in the scattering patterns running along the flow direction. In real space this corresponds to more pronounced structures along the vorticity, as compared to the flow direction. No major changes of this anisotropy with increasing shear rate were observed using the factor *A* based on the eigenvalues of the second-order moment tensor (Johnson and Fuller 1988) (results not shown). It should be mentioned that this method is not very sensitive to minor changes in anisotropy (Hoekstra *et al.* 2005) and results using the more sensitive polarimetry is presented in the next section. Averages of the intensity as a function of the magnitude of the scattering vector of the patterns in arc segments oriented along the flow and vorticity directions are depicted in Figure 1 (the curves for the different shear rates have been offset vertically for clarity). For a given shear rate, the magnitude and the power-law exponent of the scattered intensity, *I*, now depends somewhat on the direction. The power-law exponent is equal to 1.71 and 1.70 when the pattern was scanned along the flow and vorticity directions, respectively, with a negligible standard deviation of 0.08 on the shear rate range explored from 0 to 100 s^{-1}. The essentially constant fractal dimension slope of *I* versus *q* with shear rate is in contrast with the reports on more significant shear-induced densification for thermoreversible aggregated suspensions (Hoekstra *et al.* 2003, Rueb and Zukoski 1997, Varadan and Solomon 2001). On the other hand, the presence of a network of mass-fractal clusters is in agreement with the low-frequency plateau storage modulus

reported earlier (Mobuchon *et al.* 2007). The I versus q curves for the suspension scanned along the two perpendicular directions do differ in level of the intensity, especially at the higher shear rates. Averages on the scattering pattern along the flow direction yield higher intensities. This reflects a higher number density of scatterers along the vorticity direction, and suggests that the main structural rearrangements to be along the flow direction, albeit on length scales which are larger than the ones probed in this experiment, with the structure in the flow direction being opened up by flow. The independence of fractal dimension of the clusters does suggest that the building blocks are not fundamentally altered in the shear range probed. The characteristic cluster size could not be extracted from the intensity distribution since the I vs. q does not deviate enough from the power-law behavior in the experimental q range. The picture emerging from the SALS patterns is that of a network of clusters, being broken up by flow. The higher scattering intensity from structures along the vorticity direction is in agreement with the reports of roller-like structures oriented along the vorticity direction during flow in a number of systems (Vermant and Solomon 2005). Observations in the real space using confocal laser scanning microscopy (CLSM) will be reported in a subsequent article to further confirm the existence of a mass-fractal network and its dimensions.

b) Dichroism measurements

To quantify the flow-induced anisotropy, the dichroism, Δn", and its orientation angle, χ, were measured for shear rates ranging from 10^{-3} to 10^{2} s^{-1}. Figure 4.2 reports the dichroism, Δn", in the velocity gradient plane as a function of the applied shear rate for two different volume fractions of particles (ϕ_v = 0.01 and 0.03) and gaps (590 and 949 μm with ϕ_v = 0.03). The two volume fractions were chosen to be above the liquid-solid transition. At the largest volume fraction of 0.03 the dichroism is shown to be independent of gap-size (circular symbols in Figure 4.2), indicating that there is no effect of multiple scattering (Batchelor *et al.* 1987) and that the maximum length scale of the structures is smaller than 590 μm. The magnitude of the dichroism increases with the clay volume fraction, but in either case the same trend with increasing shear rate is displayed, from a low to a high plateau value.

The variations of the anisotropy in the velocity gradient and vorticity planes as functions of the applied shear rate are presented in Figure 4.3 for a particle volume fraction of 0.01. The steady-shear viscosity data are also included on the same figure and are represented by the solid lines. In comparison with the results for the velocity gradient plane, the dichroism in the vorticity plane exhibits a stronger dependency on the shear rate (Figure 4.3a). At the lowest shear rate investigated (10^{-3} s^{-1}), it is nearly zero but increases monotonously with shear rate to a plateau value, just slightly lower than for the velocity gradient plane. As shown in Figure 4.3b, the orientation angle in the vorticity plane also depends on the shear rate, unlike in the velocity gradient plane

where the orientation angle χ is close to 0^{o} (filled symbols in Figure 4.3b), implying that scatterers are oriented along the flow direction in the velocity gradient plane. At the lowest shear rate the orientation in the vorticity plane is about 25^{o} with respect to the flow direction and evolves towards the flow direction (0^{o}) at high shear rates. Apart from their different dependencies on shear rate, the changes in the dichroism in the two planes do not take place on the same shear rate range. In the vorticity plane, Δn" and χ follow the evolution of the shear-thinning of the viscosity of the suspension. On the other hand, the anisotropy in the velocity gradient plane keeps increasing, although the viscosity plateau at high shear rates is almost reached, i.e. when the thermodynamic contribution (particle-particle interactions) to the total steady stress becomes insignificant with respect to the hydrodynamic forces (Figure 8 in Mobuchon *et al.* (2007)). The evolution of the scattering dichroism with shear rate is in agreement with the progressive alignment and orientation in the flow direction of the structural building blocks. Yet, the observed evolution cannot be explained solely by the orientation of individual particles. Clearly a more complex interplay between the aggregate structure at low shear rates and the orientation of the structure building blocks at high shear rates leads to a more complex dependency of the scattering dichroism. Finally, upon cessation of flow the flow-induced anisotropy in the two planes was observed not to relax (results not shown), at least on the time interval required for full recovery of their viscoelastic properties (Figure 2a of Mobuchon *et al.* (2007)). The metastable clay microstructures shown in our previous work are consequently anisotropic. A persisting

anisotropy at large scale was also observed for organophilic silica suspensions with the lack of relaxation of their anisotropic SLS patterns (Hoekstra *et al.* 2005, Mohraz and Solomon 2005, Varadan and Solomon 2001, Verduin *et al.* 1996).

The retention of the anisotropy outlines the weakness of the Brownian forces compared to the attractive (van der Waals) and excluded volume repulsive forces. As a result, the interplay between these non-Brownian thermodynamic forces and the hydrodynamic forces governs for the most the orientation evolution of this aggregated colloidal suspension depicted in Figure 4.3.

4.4.2. Orientational contribution to stress growth measurements

It is intuitively reasonable to expect that the flow-induced anisotropy highlighted previously will imply orientational mechanisms in the transient response of these colloidal suspensions. In order to clarify this, stress growth data for forward and reverse directions have been compared. This procedure was initially proposed as a structural-destructive testing to probe the structural anisotropy under flow and at rest. The main features of the transient behavior of the organoclay suspension at a volume fraction of 0.04 are presented in Figure 4.4. In addition to the transient shear stress, the transient orthogonal moduli $G'_{\perp}$ and $G''_{\perp}$, measured at a frequency of 62.8 rad/s, are reported as a function of the strain, γ. The moduli were measured using the set-up for the axial oscillatory deformation of the 2D-SAOS. Transient superposition measurements are nontrivial to analyze, as the changes in the structure and stress also

lead to transients in the oscillatory response. Yet, because of the high frequency used, and the relatively long time scales of the transient response, this should not be too problematic in the present case. Hence, we believe this is a novel tool for probing the evolution of the microstructure. Upon stepwise changes in shear rate, the organoclay suspension undergoes a structure build-up or break-down. Figure 4.4a illustrates the structure breakdown for a stepwise increase in shear rate from 10^{-3} s^{-1} to 0.1 s^{-1}. According to Figure 4.3a, this stepwise change in shear rate affects mainly the anisotropy in the vorticity plane. Through the elastic response of the initial structure, the transient shear stress, σ^+, increases as a function of γ, depicting a typical overshoot before reaching a steady-state value at large strain, as illustrated in Figure 4.4a. However, the two superposition moduli at this high frequency stay nearly constant during the initial period. Monotonous decreases with γ towards a plateau value are then observed for $G'_{\perp}$ (more pronounced) and $G''_{\perp}$ during the breakdown toward a less elastic final structure. It should be pointed out that more dramatic drops of the superposition moduli are expected at low frequencies. The low frequency part of the spectrum of colloidal suspensions was actually shown experimentally (Potanin *et al.* 1997) and numerically (Dhont and Wagner 2001) to be more sensitive to the shear induced structural deformation. A stepwise decrease in shear rate from 1 to 10^{-2} s^{-1} corresponding to structure build-up is shown in Figure 4.4b. The initial decrease in the shear stress with strain is typical of stress relaxation in viscoelastic materials and the following shear stress increase is due to the structure build-up. Nearly stable moduli are

observed during the relaxation of the initial structure, and as for the structure breakdown, the moduli follow the stress response, increasing up to a characteristic value of the final, stronger structure (initial structure in Figure 4.4a). On the other hand, the elastic modulus does not evolve in the same manner as the transient shear stress measured during a reverse flow at 10^{-2} s^{-1} following an initial forward flow at the same shear rate. The results are illustrated in Figure 4.4c. At this shear rate, the organoclay network structure, as detected by SALS, is strongly developed and the hydrodynamic contribution to the total steady stress is negligible (see Figure 3 and Figure 7 of Mobuchon *et al.* (2007)). In the first part of the curve, where σ^+ is negative, the initial structure induced by the preceding shear in the opposite direction relaxes as suggested by the constant $G'_\perp$. However, the initial structure resists partially to the reverse flow since $G'_\perp$ does not vanish. The subsequent evolution of the elastic modulus indicates that the initial structure is subjected to a rearrangement to conform to the flow reversal. As mentioned previously, at an applied shear rate of 10^{-2} s^{-1} the total steady stress is mainly due to an elastic contribution, most likely stemming from an aggregate network (Mobuchon *et al.* 2007). A reverse flow is therefore expected to involve the relaxation of the initial structure followed by the elastic stretching in the opposite direction. These elastic-induced deformations do not affect significantly $G'_\perp$ (Figure 4.4a and Figure 4.4b). A reverse flow even at low shear rate involves consequently both orientational and structural mechanisms. Tests with and without rest time between the pre-shearing and the stress growth experiments were also carried out and the results are presented in

Figure 4.5. Figure 4.5a reports data obtained without a rest time for forward (open symbols) and reverse start-up flow experiments (filled symbols) done at an applied shear rate of $\pm 10^{-1}$ s^{-1}. Figure 4.5b reports the corresponding data obtained following a rest time of 5400 s. In these tests, three different pre-shear rates, $\dot{\gamma}_i$, were used: 10^{-3}, 1 and 10 s^{-1}. Depending on the amplitude of the pre-shear rate, the transient shear stresses exhibit either the characteristic evolution of a structure breakdown (Figure 4.4a) or build-up (Figure 4.4b) as described above. Following a pre-shearing at 10^{-3} s^{-1}, the forward (open symbols) and reverse (filled symbols) stress growths do not overlap, suggesting a flow-induced anisotropy (Figure 4.5a and Figure 4.5b). For a larger pre-shear rate, the difference between the forward and reverse stress growths becomes negligible, even when a rest time is allowed. These results appear at first to be in contradiction with the increase of anisotropy with shear rate observed previously from the dichroism measurements. This apparent contradiction can be explained by the minor role played by the initial anisotropy on the transient stress response, as it implies a pronounced structural contribution (i.e. evolution of the particle spatial distribution) to reach a more or less developed structure. One may argue that the scattering dichroism is more sensitive to the local scale arrangements, whereas the stresses seem to be governed by larger scale structures. A different procedure has been applied by using the same shear rate amplitude for the stress growth than for the pre-shearing (Figure 4.5c), following a rest time. In this case, the structural contribution arises from the structure build-up during the rest time between the pre-shearing and the stress

growth measurement. Despite the fact that the experimental investigation suffers from limitations in the strain range at large shear rate, the same trend as observed before (Figure 4.5a and Figure 4.5b) emerges.

In light of the previous results, the structural-destructive testing based on forward and reverse stress growth measurements does not bring out systematically the initial structural anisotropy. In the next section, results for non-destructive mechanical testing based on 2D small amplitude oscillatory shear measurements are presented.

4.4.3. Mechanical anisotropy of metastable organoclay structures

a) Two-dimensional small amplitude oscillatory shear (2D-SAOS)

In these experiments the moduli are probed along a specific direction. At first, the Newtonian suspending fluid (polybutene) was investigated to assess the performance of the set-up. Typical unidirectional oscillatory deformations projected in the shear plane are illustrated in Figure 4.6**Erreur ! Source du renvoi introuvable.**a for a frequency of 25 rad.s^{-1}, in terms of γ_z vs. γ_θ for different phase angles, $\varphi_{z\theta}$, between the two orthogonal solicitations. The oscillatory deformations could be imposed continuously from 0° to 180° on a large frequency range. As expected for an isotropic fluid, the loss modulus, *G"*, of the Newtonian polybutene does not depend on the solicitation angle, $\varphi_{z\theta}$ (Figure 4.6**Erreur ! Source du renvoi introuvable.**b). A deviation of less than ±3 % is observed for the $\varphi_{z\theta}$ range covered. On the other hand, for the organoclay suspension following a pre-shearing at 3 s^{-1} and a rest time of 5400 s a strong

dependency of the moduli with $\varphi_{z\theta}$ is reported in Figure 4.6 for a frequency of 0.63 rad/s. Both moduli vary similarly (δ independent of $\varphi_{z\theta}$) by more than 50 % when the solicitations go perpendicular ($\varphi_{z\theta} = 0^{o}$) to the pre-shearing direction ($\varphi_{z\theta} = 90^{o}$). The data in the pre-shearing direction are in good agreement with those previously reported for this system (Figure 4 of Mobuchon *et al.* (2007)). The trend depicted in Figure 4.6 is also observed to be independent of the frequency for the range investigated, as shown in Figure 4.7a for the elastic modulus data and in Figure 4.7b for the normalized modulus ($G'/G'_{\phi_{z\theta=180^{o}}}$). Nevertheless, the strong dependency on $\varphi_{z\theta}$ outlines the anisotropic nature of the clay structure and is consistent with the lack of relaxation of the dichroism after cessation of shear.

Figure 4.8 presents the effect of the pre-shearing amplitude, $\dot{\gamma}_i$, on the storage modulus as a function of the solicitation angle at a fixed frequency of 0.6 rad.s^{-1}. The storage modulus is observed to decrease with increasing the initial shear rate indicating a weakening of the corresponding final structure (Figure 4.8a). However, when normalized as $G'/G'_{\phi_{z\theta=180^{o}}}$, the suspension surprisingly displays a behavior as a function of the solicitation angle approximately independent of the pre-shearing amplitude ($\dot{\gamma}_i$ = 3 10^{-3} - 3 s^{-1}) and so, for all the different metastable structures reached (Figure 4.8b). Over the investigated range of pre-shear rates, the anisotropy in the velocity gradient plane was shown to remain constant while it increased in the vorticity plane (Figure 4.2). Therefore, it seems that the mechanical response to 2D-SAOS

solicitations is less sensitive compared to the rheo-optical measurements may be because of the low volume fraction used or because the rheo-optical measurements are sensitive to both form and structural contributions, whereas the latter might dominate the stress response. In addition, a stronger dependency on the solicitation angle is observed following a pre-shearing done in large amplitude oscillatory shear (LAOS) at 0.63 rad.s^{-1} and a strain of 10 (Figure 4.9). This test leads respectively to a weaker structure (Figure 4.9a) and to a more anisotropic, metastable structure (Figure 4.9b) than a pre-shearing at 3 s^{-1}.

b) Two-dimensional small amplitude oscillatory shear with phase lag (2D-SAOS δ_γ)

In these experiments the entire shear plane was scanned in a single period, giving an instantaneous 'image' of the mechanical anisotropy. The two-dimensional small amplitude oscillatory shear with phase lag was also firstly tested with the Newtonian polybutene. Figure 4.10 illustrates the circular applied deformation, γ_z as a function of γ_θ, and the resulting stress response, σ_θ as a function of σ_z, at a frequency of 25 rad.s^{-1}. The stress response is also circular with a slight deformation induced by an added phase shift between the two stress components. This additional phase shift comes from control loop of the normal force rebalance transducer, which is not fully adapted to perform this experiment at high frequency. The experimental frequency window was therefore limited up to 25 rad.s^{-1} to avoid this experimental artefact. As expected for a

purely viscous fluid, the phase lag between the strain and stress components is close to $\pi/2$, and leads with $\gamma^0 = 0.28$ and $\sigma_z^0 = \sigma_\theta^0 = 34$ Pa, to the same value of the loss modulus, i.e. $G'' \approx 1214$ Pa reported in Figure 4.6.

In the case of the organoclay suspension (Figure 4.11), the stress response becomes elliptic with its major axis (highest moduli) perpendicular to the pre-shearing direction. As seen before for the 2D-SAOS without phase lag, the overall tendency is observed to be independent of the frequency on the range investigated (ω = 0.06-0.63 rad.s^{-1}), as confirmed by the normalized stress in Figure 4.11b. The behavior does not depend either on the pre-shearing amplitude ($\dot{\gamma}_i$ = 3 10^{-3} - 3 s^{-1}) as shown in Figure 4.12. However, a more pronounced elliptic stress response is observed following a pre-conditioning based on a LAOS experiment (ω = 0.63 rad.s^{-1}, γ^0 = 10) and different rest times (10 and 5190 s) and this is reported in Figure 14. During the rest time, the structure builds up and the stress response increases (Figure 4.13a) according to a homothetic transformation (Figure 4.13b), which is in agreement with the persistent dichroism at rest. Finally, the equivalence of these solicitations with 2D-SAOS with solicitations done without phase lag is shown in Figure 4.8a by the dashed lines. The storage moduli extracted from the elliptic stresses merge with the ones given by the 2D-SAOS.

4.5. Concluding remarks

In this article the flow-induced orientation of non-aqueous layered silicate suspensions has been probed optically using small angle light scattering and linear dichroism measurements. A newly developed non-destructive mechanical method based on two-dimensional small amplitude oscillatory shear flow (2D-SAOS) has also been proposed to quantify the flow-induced orientation.

The existence of an anisotropic organoclay network structure has been inferred from the power-law decay of the small angle light scattering (SALS) intensity. The structure is slightly denser in the flow direction compared to the vorticity direction. The constant fractal dimensions with the shear rate denote the lack of significant shear-induced densification. The linear dichroism measurements have shown that the anisotropy evolutions in the velocity gradient and vorticity gradient planes do not take place on the same shear rate range. In the vorticity gradient plane, the monotonous increase of the anisotropy with shear rate towards the flow direction was observed to follow the shear-thinning behaviour of the suspension and was consequently ascribed to network structural changes. In contrast, the anisotropy in the velocity gradient plane still intensifies once the viscosity plateau is reached, accompanied by only a minor evolution of the orientation angle. The anisotropy induced at these high shear rates in the velocity gradient plane can be rationalized by the evolution of the spatial

distribution of the structure building blocks, as suggested by the slightly anisotropic SALS pattern with two lobes observed in the velocity gradient plane.

Upon cessation of flow, the flow-induced anisotropy in the two planes was observed not to relax which denotes the lack of restoring forces to evolve toward isotropy. Consequently, the metastable organoclay structures have the same anisotropic nature as their non-equilibrium counterparts. The structure build-up observed at rest was explicitly shown to follow a homothetic transformation using the 2D-SAOS with phase lag. Actually, the 2D-SAOS technique with and without phase lag proved to be sensitive to the anisotropic nature of the organoclay suspensions. This technique appears to be powerful, representing an alternative to scattering methods in the case of non-transparent or concentrated complex fluids. These primary results are encouraging and should foster further research to define the limitations and sensitivity of the 2D-SAOS method.

As a result of the flow-induced orientation, the transient response of the organoclay suspensions implies both structural and orientational contributions. By comparing stress growth data in the forward and reverse directions, the orientational contribution has been shown to play an increasing role as the transient flow evolve from a structure build-up to a structure breakdown. In the perspective of modeling their non-linear rheological behaviour, the two contributions have to be included in the constitutive equation. A detailed investigation of the micro-scale structural evolution under flow will be reported in a subsequent publication.

4.5.1. Acknowledgements

The authors wish to thank Mr. Allen Glasman (Senior Technical Support Specialist), from TA Instruments, for his precious help in setting up the two-dimensional amplitude oscillatory shear functionality. We also acknowledge helpful support and discussions with Prof. Gerald G. Fuller. Southern Clay Products kindly provided the nanoclay used in this study. One of the authors (C.M.) is thankful to Alcan Inc. for a scholarship and to the Groupe Français de Rhéologie for a travel grant to attend the 4th Annual Meeting of the European Society of Rheology (Naples, Italy). Finally, financial support from NSERC (Natural Science and Engineering Research Council of Canada) and from FQRNT (Fonds Québécois de Recherche en Nature et Technologies) is gratefully acknowledged.

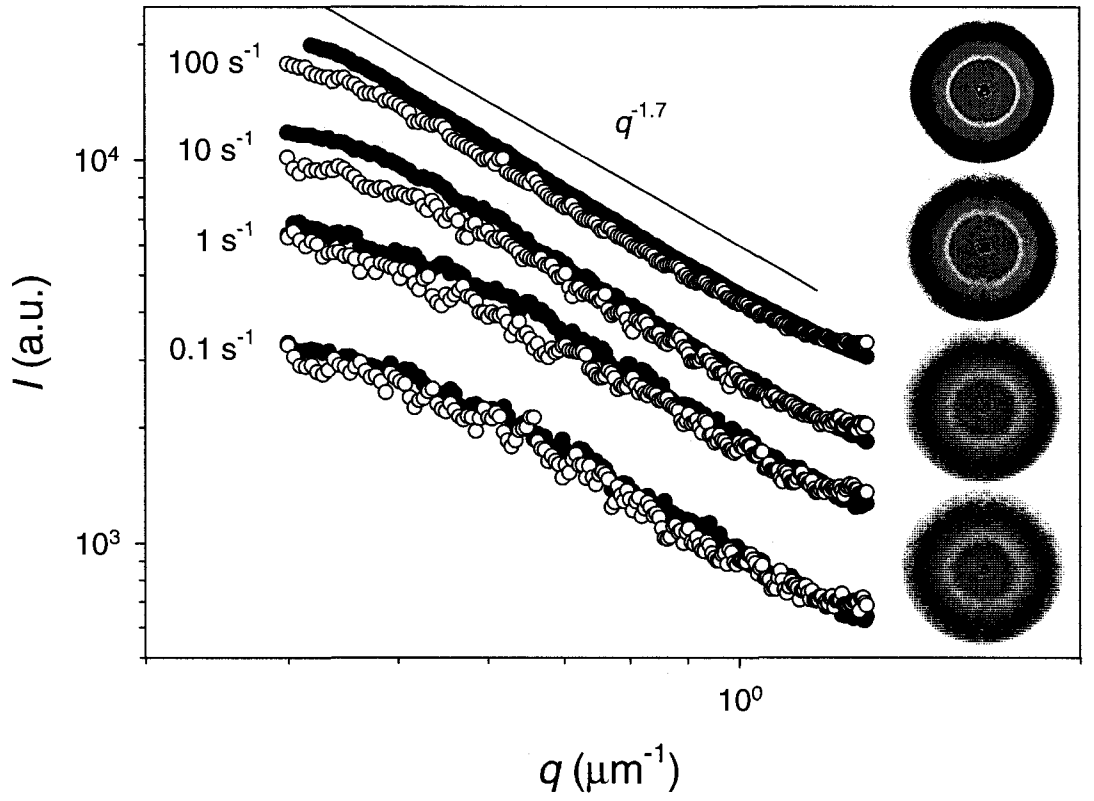

Figure 4.1 : Scattered intensity distribution $I(q)$ in the flow (filled symbols) and vorticity (unfilled symbols) directions as $\dot{\gamma}$ is varied from 0.1 to 100 s^{-1}. Data are offset for clarity. The solid line represents the measured fractal dimension. The inset figures show the corresponding SALS patterns in the same order than the scattered intensity distributions. The flow direction is from left to right, vorticity direction is from bottom to top. $\phi = 0.03$.

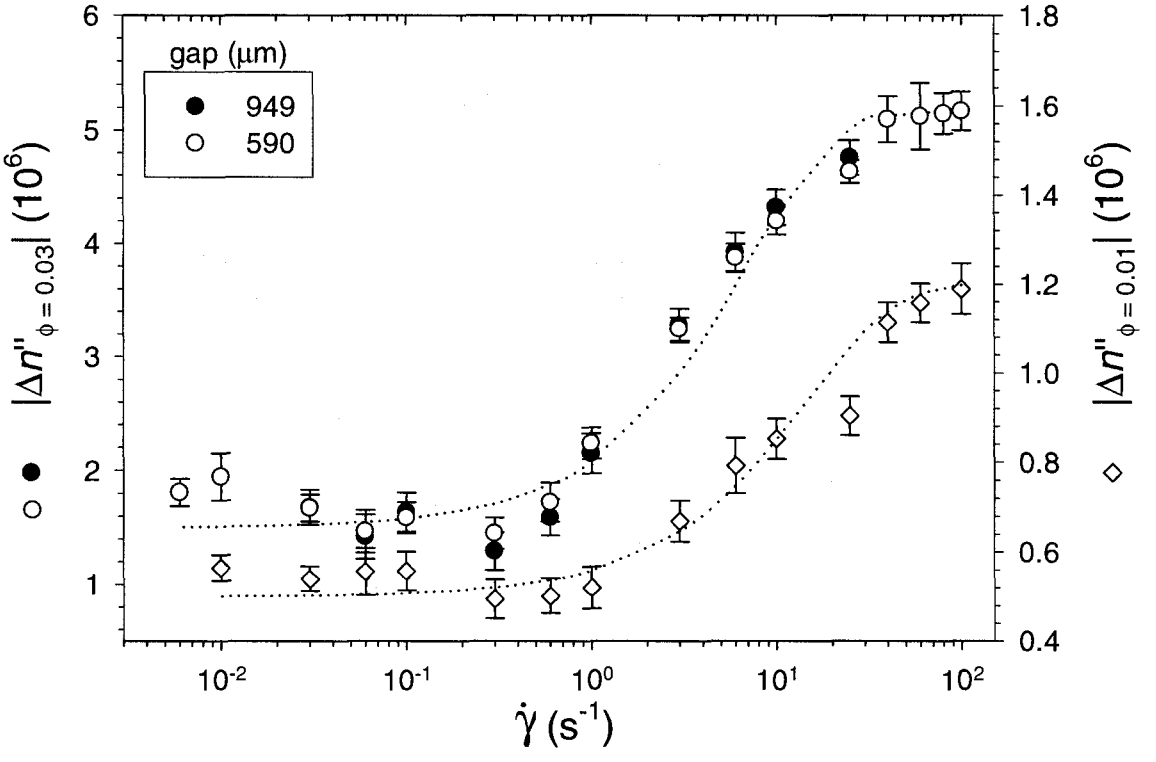

Figure 4.2 : Effect of the gap and volume fraction on $|\Delta n''|$ measured in the velocity gradient plane as $\dot{\gamma}$ is varied.

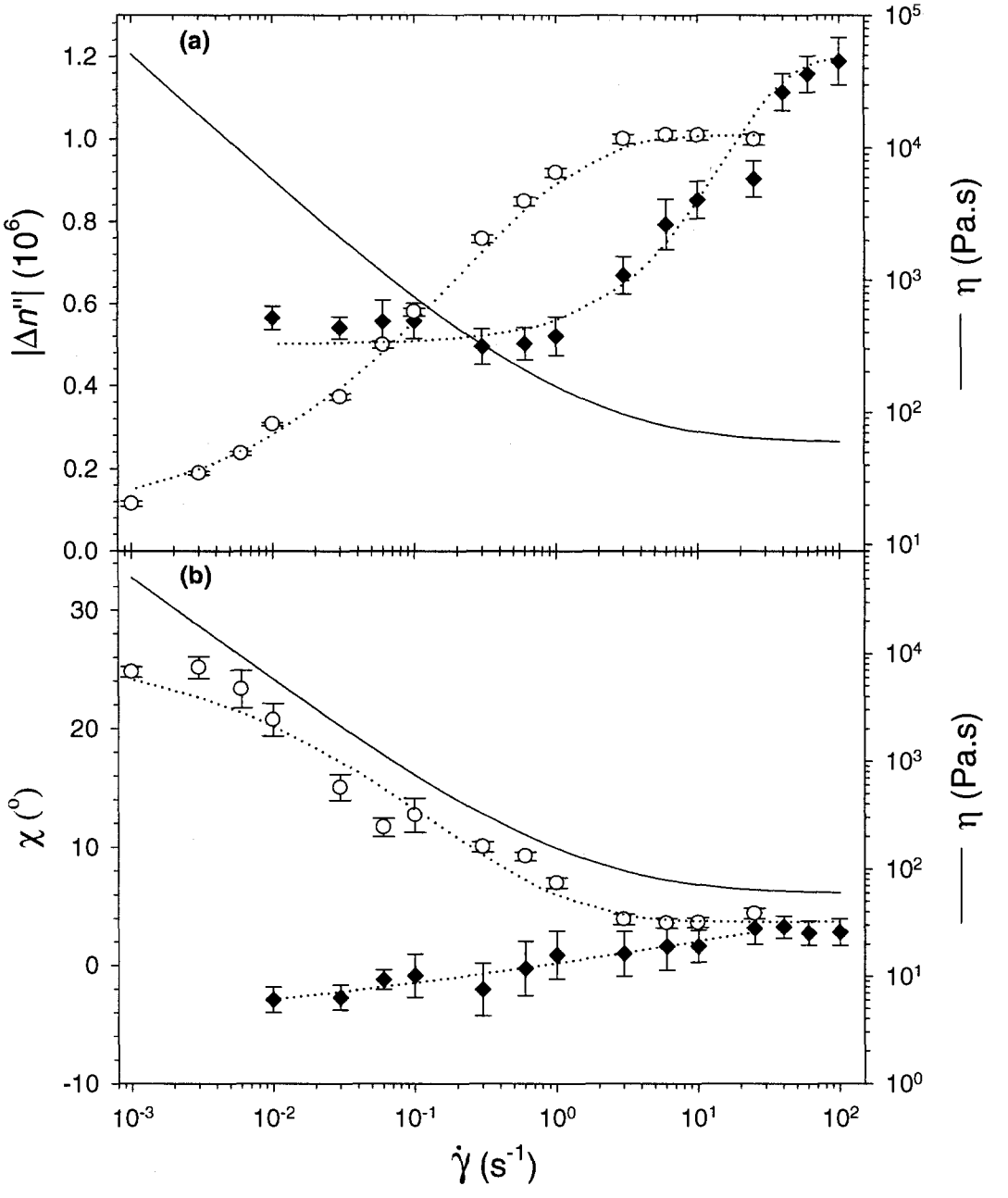

Figure 4.3 : Dependence of $|\Delta n''|$ (a) and χ (b) with $\dot{\gamma}$ in the velocity gradient (filled symbols) and vorticity planes (unfilled symbols). $\phi = 0.01$.

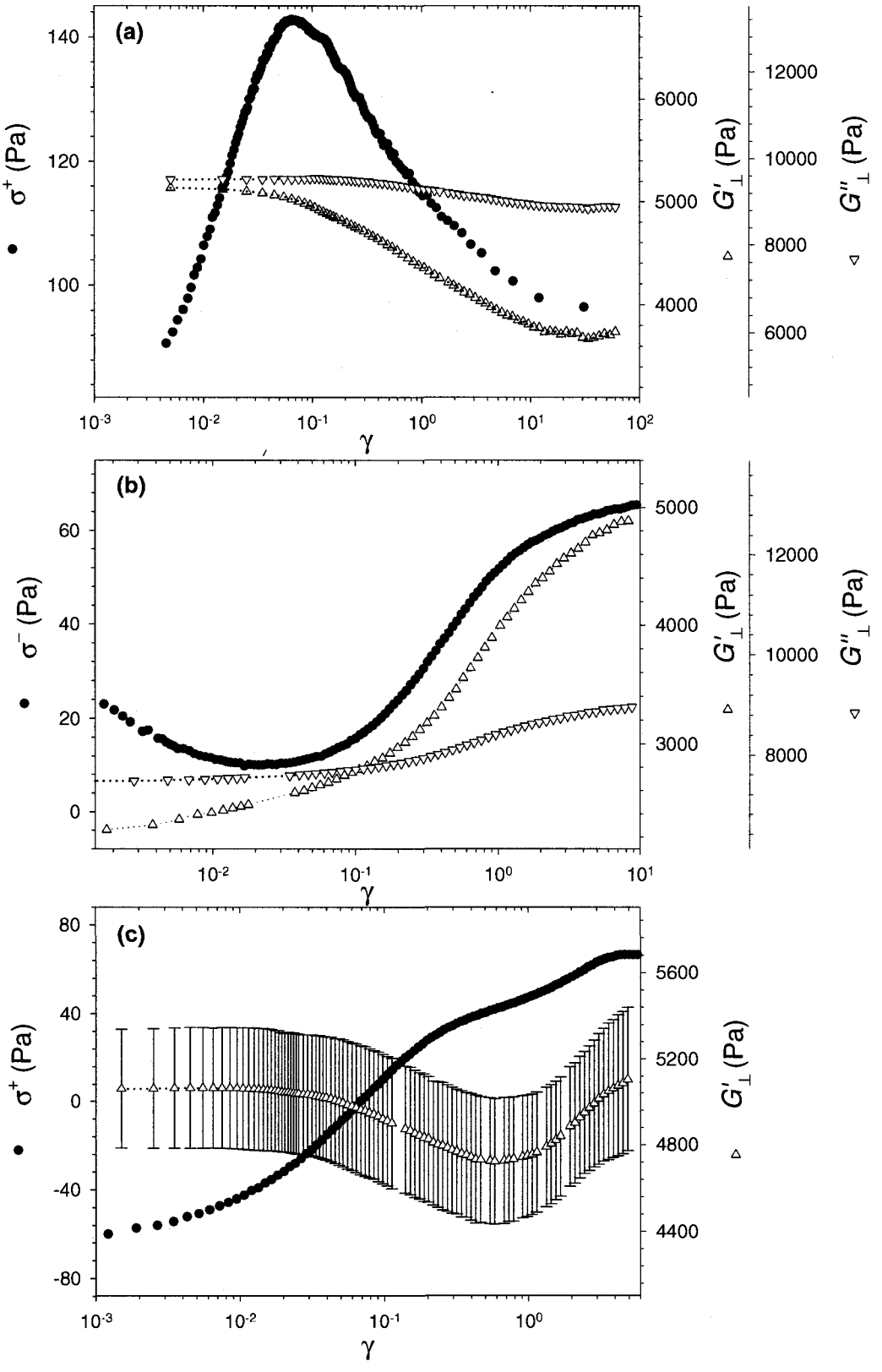
(a)
140
120
100
σ+ (Pa)
6000
5000
4000
G'⊥ (Pa)
12000
10000
8000
6000
G''⊥ (Pa)
10-3
10-2
10-1
100
101
102
γ
(b)
60
40
20
0
σ− (Pa)
5000
4000
3000
G'⊥ (Pa)
12000
10000
8000
G''⊥ (Pa)
10-2
10-1
100
101
γ
(c)
80
40
0
-40
-80
σ+ (Pa)
5600
5200
4800
4400
G'⊥ (Pa)
10-3
10-2
10-1
100
γ

Figure 4.4 : Typical transient behaviours of the organoclay suspension: stepwise increase in shear rate from $\dot{\gamma}_i = 10^{-3}$ s^{-1} to $\dot{\gamma}_f = 10^{-1}$ s^{-1} (a), stepwise decrease in shear rate from $\dot{\gamma}_i = 1$ s^{-1} to $\dot{\gamma}_f = 10^{-2}$ s^{-1} (b) and reverse flow at $\dot{\gamma} = 10^{-2}$ s^{-1} (c). $\phi = 0.04$.

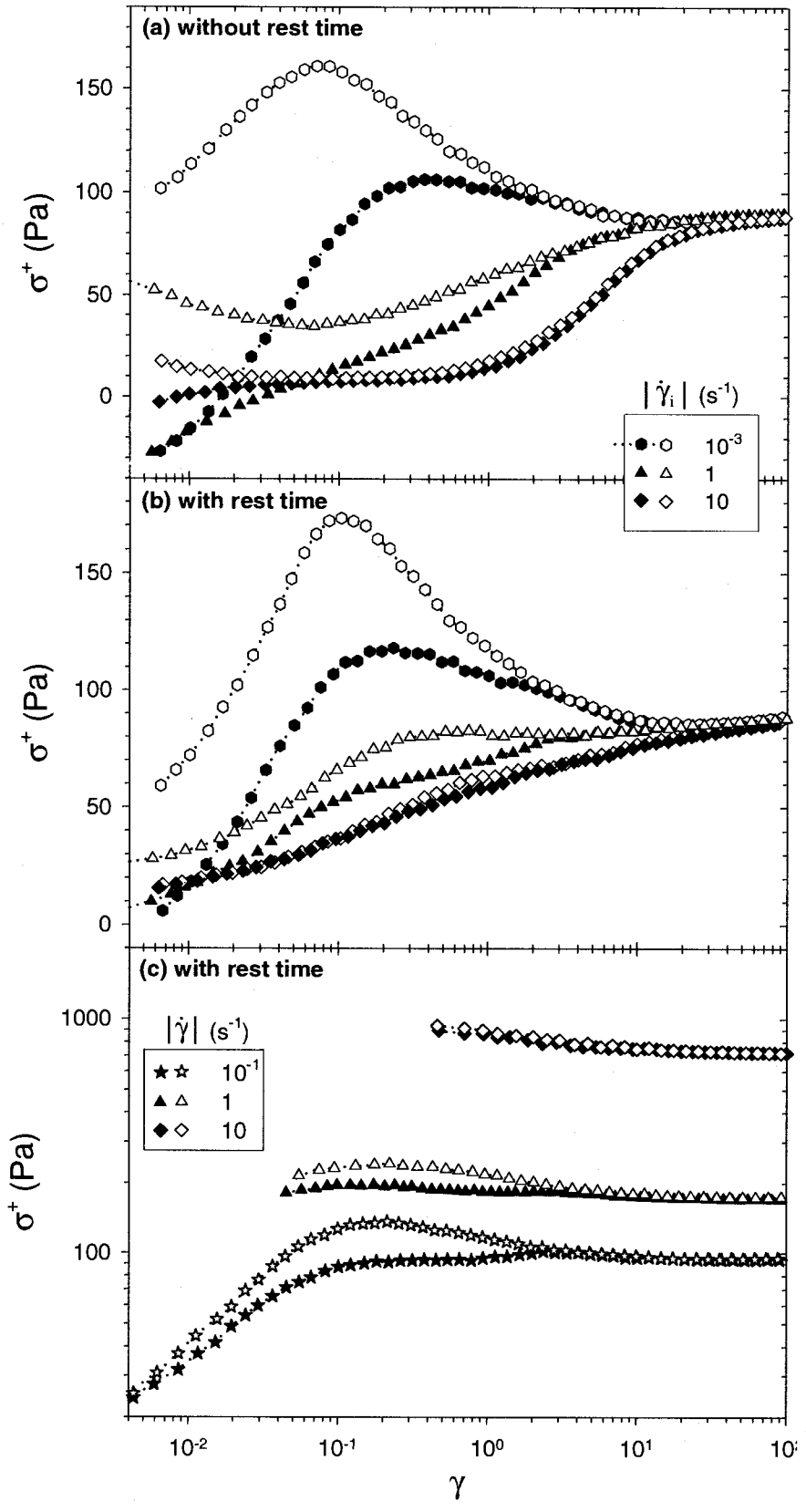
(a) without rest time
(b) with rest time
(c) with rest time
σ+ (Pa)
γ
|γ̇i| (s-1)
10-3
1
10
|γ̇| (s-1)
10-1
1
10
150
100
50
0
1000
10-2
10-1
100
101

Figure 4.5 : Stress growth measurements carried out after a pre-shearing in the same direction (unfilled symbols) and in the opposite direction (filled symbols): with pre-shearings at $|\dot{\gamma}_i|$ (a), with pre-shearings at $|\dot{\gamma}_i|$ after a rest time of 5400 s (b) and with pre-shearings at $\dot{\gamma}$ after a rest time of 5400 s (c). $\phi = 0.04$.

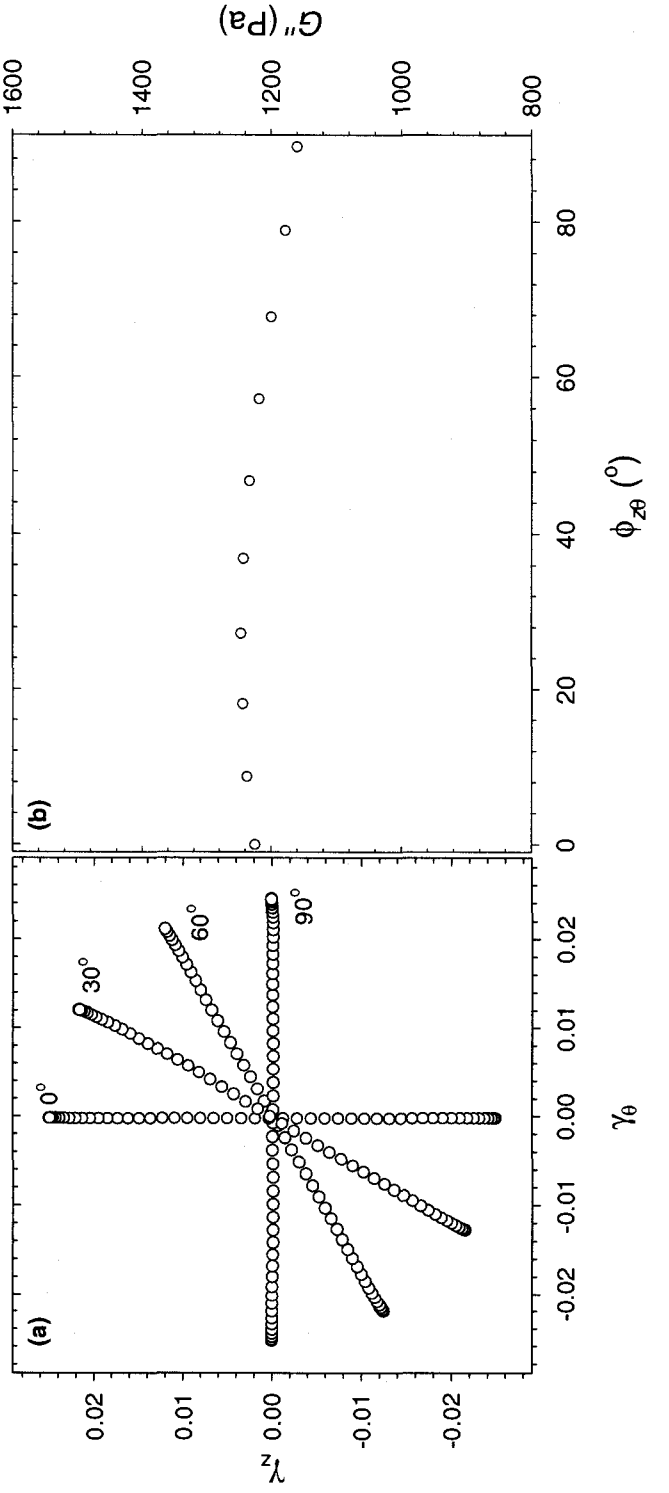

Figure 4.6 : 2D-SAOS at 25 rad.s^{-1} for the Newtonian polybutene suspending fluid: unidirectional oscillatory deformations projected in the shear plane (a) and G'' as a function of $\varphi_{z\theta}$ (b).

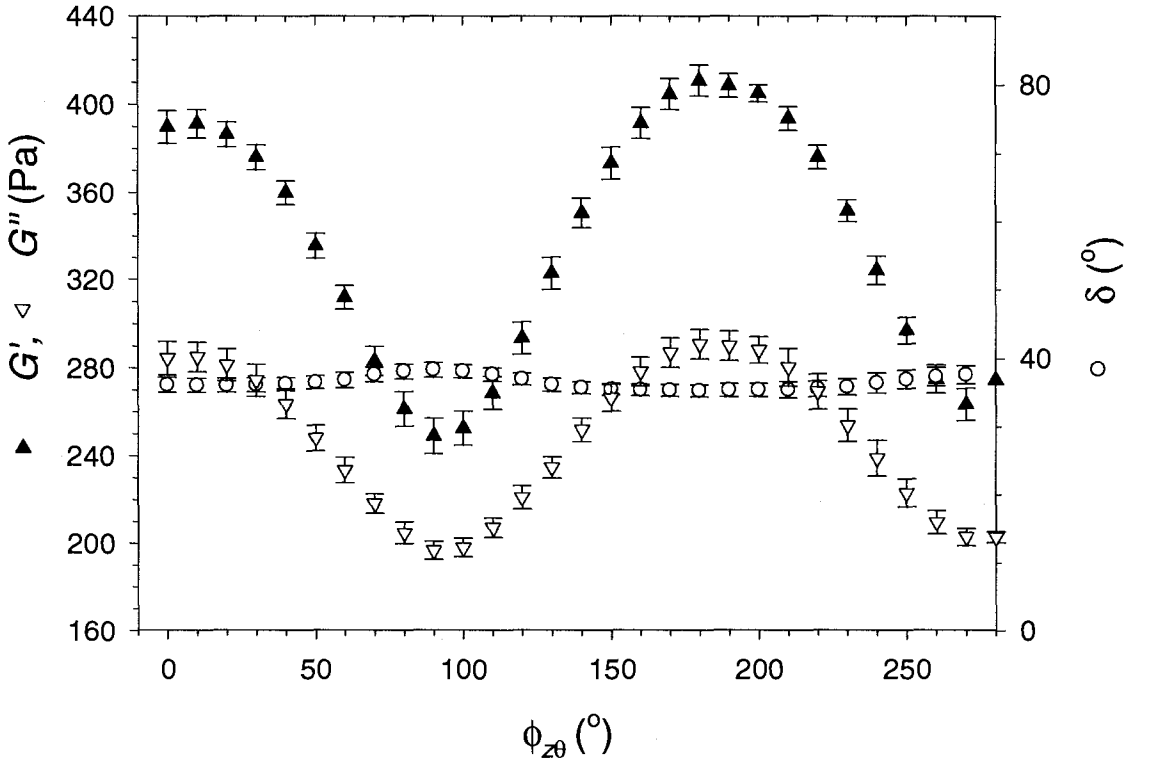

Figure 4.6 : Viscoelastic 2D-SAOS properties as a function of $\varphi_{z\theta}$ at 0.63 rad.s^{-1} after a preconditioning at 3 s^{-1} and a rest time of 5400 s. The parallel direction of the pre-shearing corresponds to $\varphi_{z\theta} = 90°$. $\phi = 0.04$.

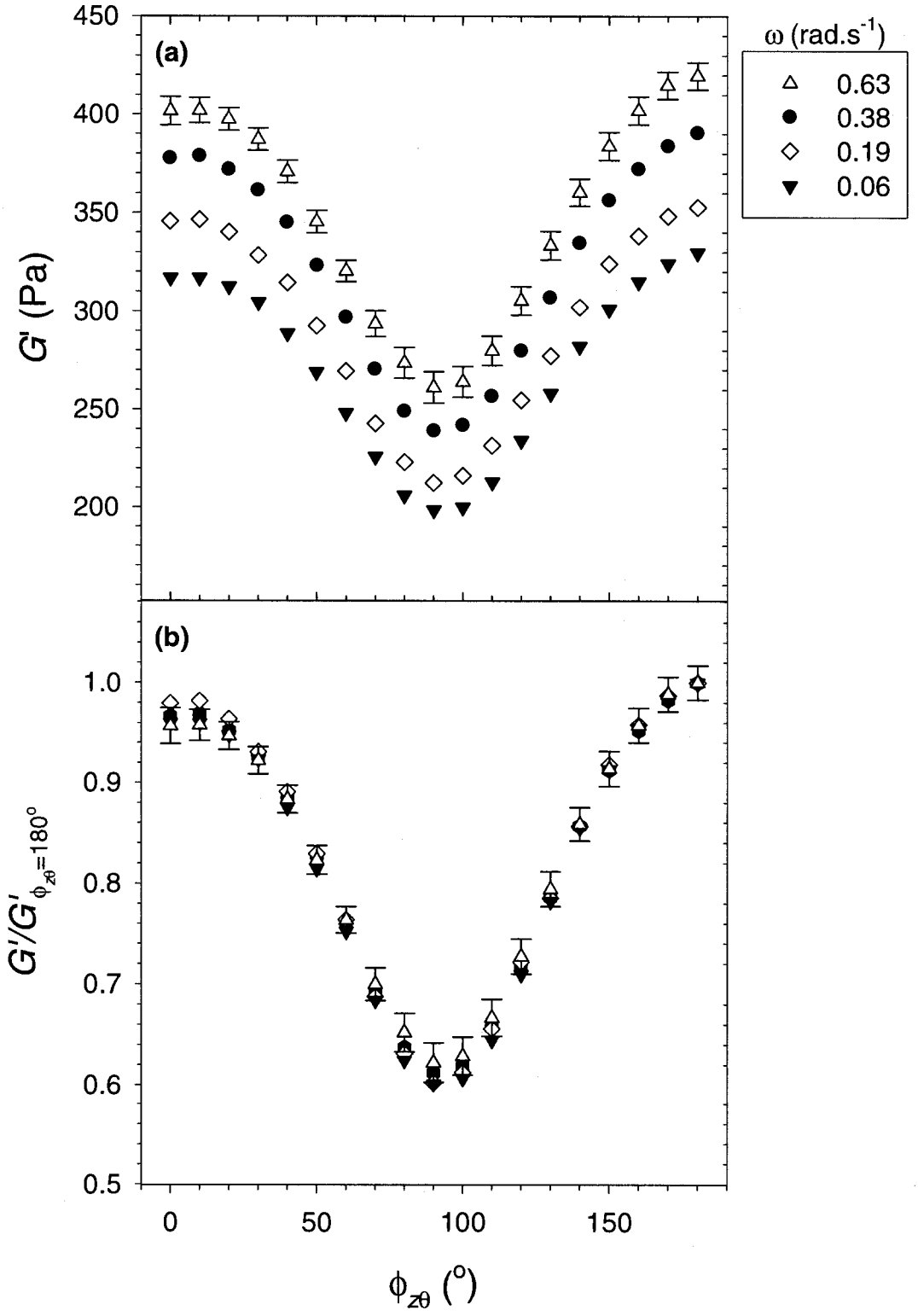
(a)
(b)
G' (Pa)
G'/G'φzθ=180°
φzθ (°)
ω (rad.s-1)
0.63
0.38
0.19
0.06
450
400
350
300
250
200
1.0
0.9
0.8
0.7
0.6
0.5
0
50
100
150

Figure 4.7 : Frequency dependency of G' (a) and $G'/G'\varphi_{z\theta=180^{o}}$ (b) as a function of $\varphi_{z\theta}$ for the organoclay suspension after a preconditioning at 3 s^{-1} and a rest time of 5400 s. $\phi = 0.04$.

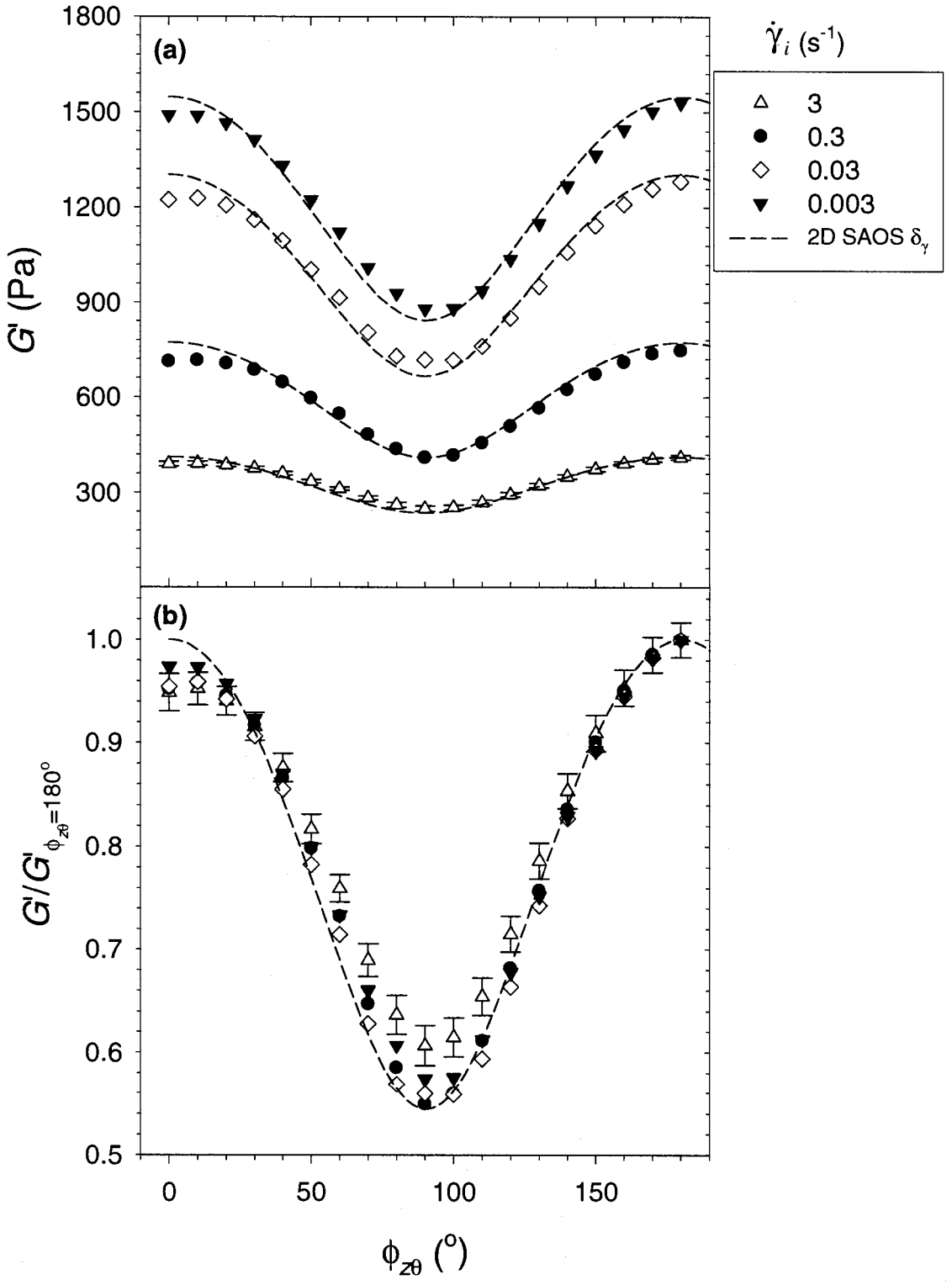
(a)
(b)
G' (Pa)
G'/G'φzθ=180°
φzθ (°)
γ̇i (s-1)
3
0.3
0.03
0.003
2D SAOS δγ
1800
1500
1200
900
600
300
1.0
0.9
0.8
0.7
0.6
0.5
0
50
100
150

Figure 4.8 : Flow history dependency of G' (a) and $G'/G'\varphi_{z\theta=180^{o}}$ (b) as a function of $\varphi_{z\theta}$ measured at 0.63 rad.s^{-1} after a rest time of 5400 s. $\phi = 0.04$.

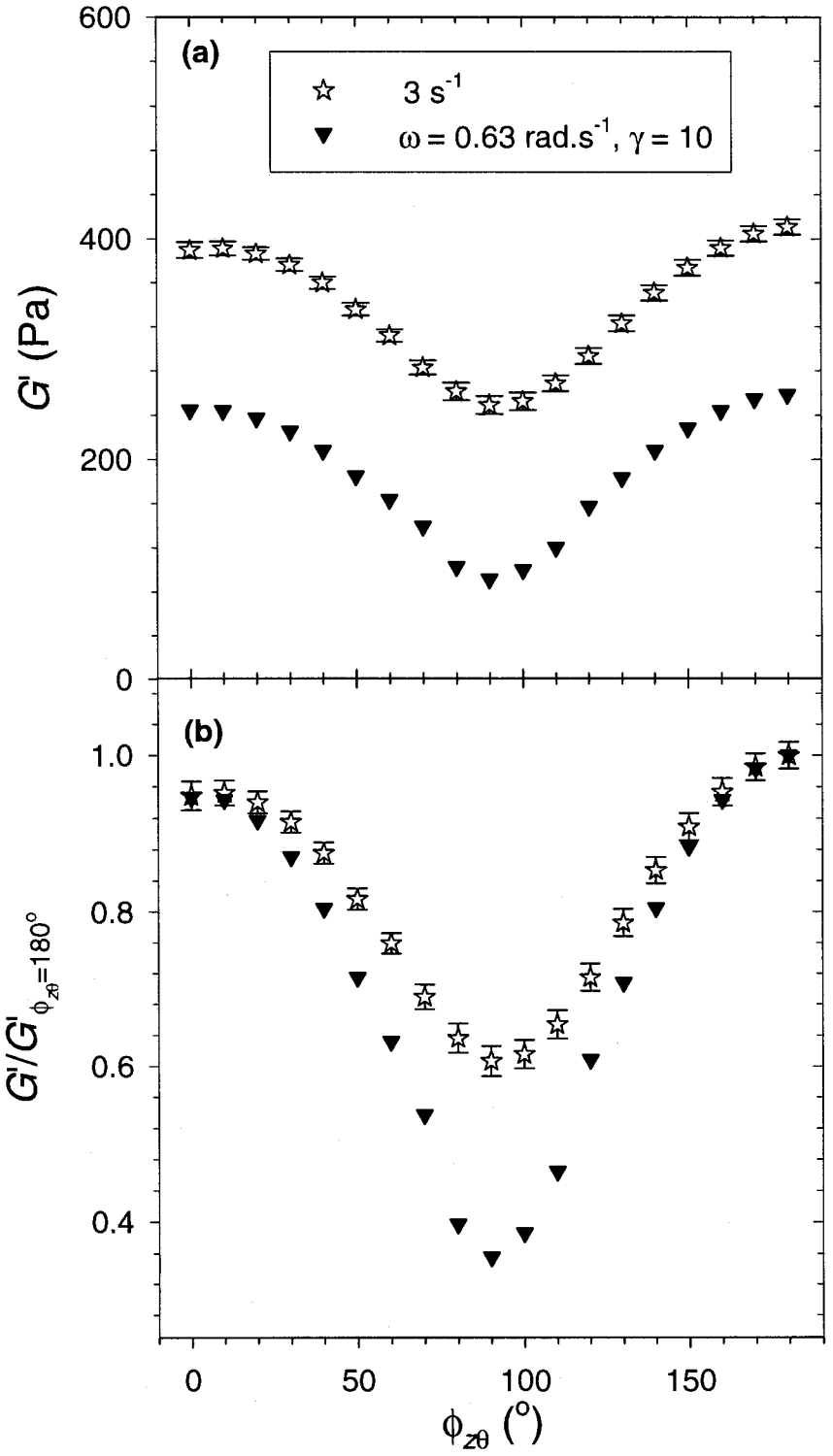
(a)
3 s-1
ω = 0.63 rad.s-1, γ = 10
G' (Pa)
600
400
200
0
(b)
G'/G'φzθ=180°
1.0
0.8
0.6
0.4
0
50
100
150
φzθ (°)

Figure 4.9 : G' (a) and $G'/G'\varphi_{z\theta=180^{o}}$ (b) as a function of $\varphi_{z\theta}$ measured at 0.63 rad.s^{-1} after different pre-shearing conditions and a rest time of 5400 s. $\phi = 0.04$.

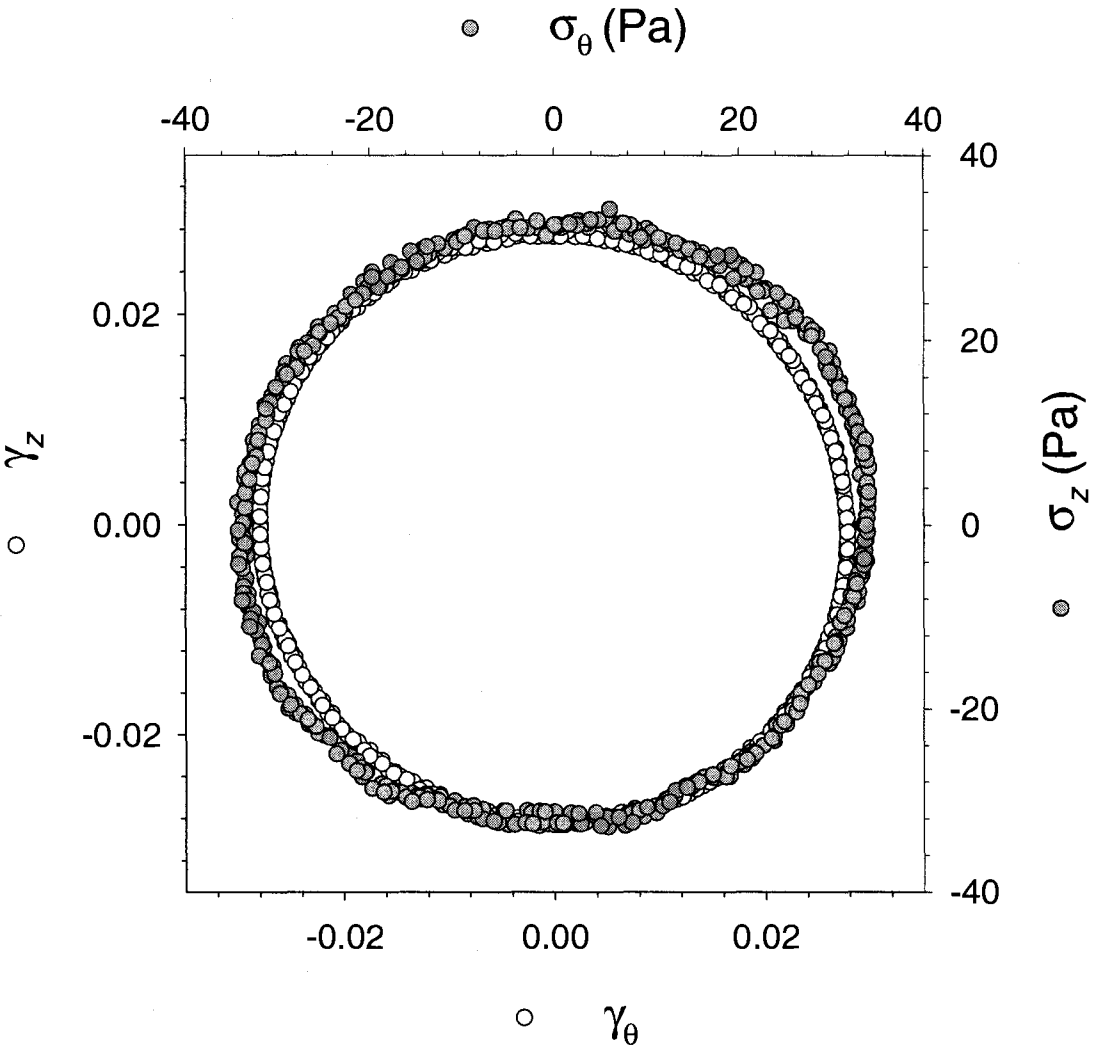

Figure 4.10 : 2D SAOS δ_γ at 25 rad.s^{-1} for the Newtonian polybutene suspending fluid: γ_z vs γ_θ and σ_z vs. σ_θ.

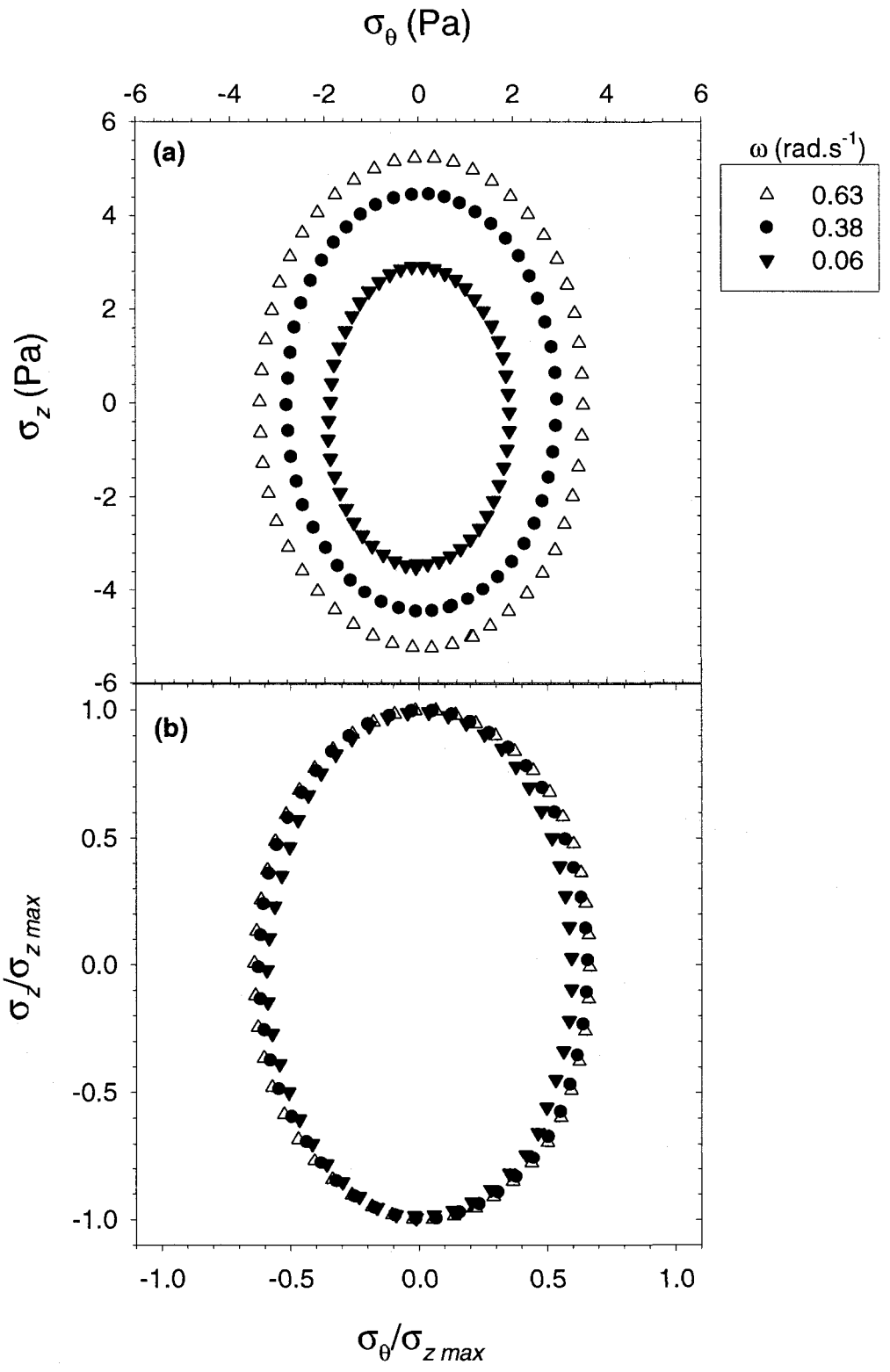
σθ (Pa)
(a)
(b)
ω (rad.s-1)
0.63
0.38
0.06
σz (Pa)
σz/σz max
σθ/σz max

Figure 4.11 : Frequency dependency of the 2D SAOS δ_γ: σ_z vs. σ_θ (a) and $\sigma_z/\sigma_{z\,max}$ vs. $\sigma_\theta/\sigma_{z\,max}$ (b) after a preconditioning at 3 s^{-1} and a rest time of 5400 s. $\phi = 0.04$.

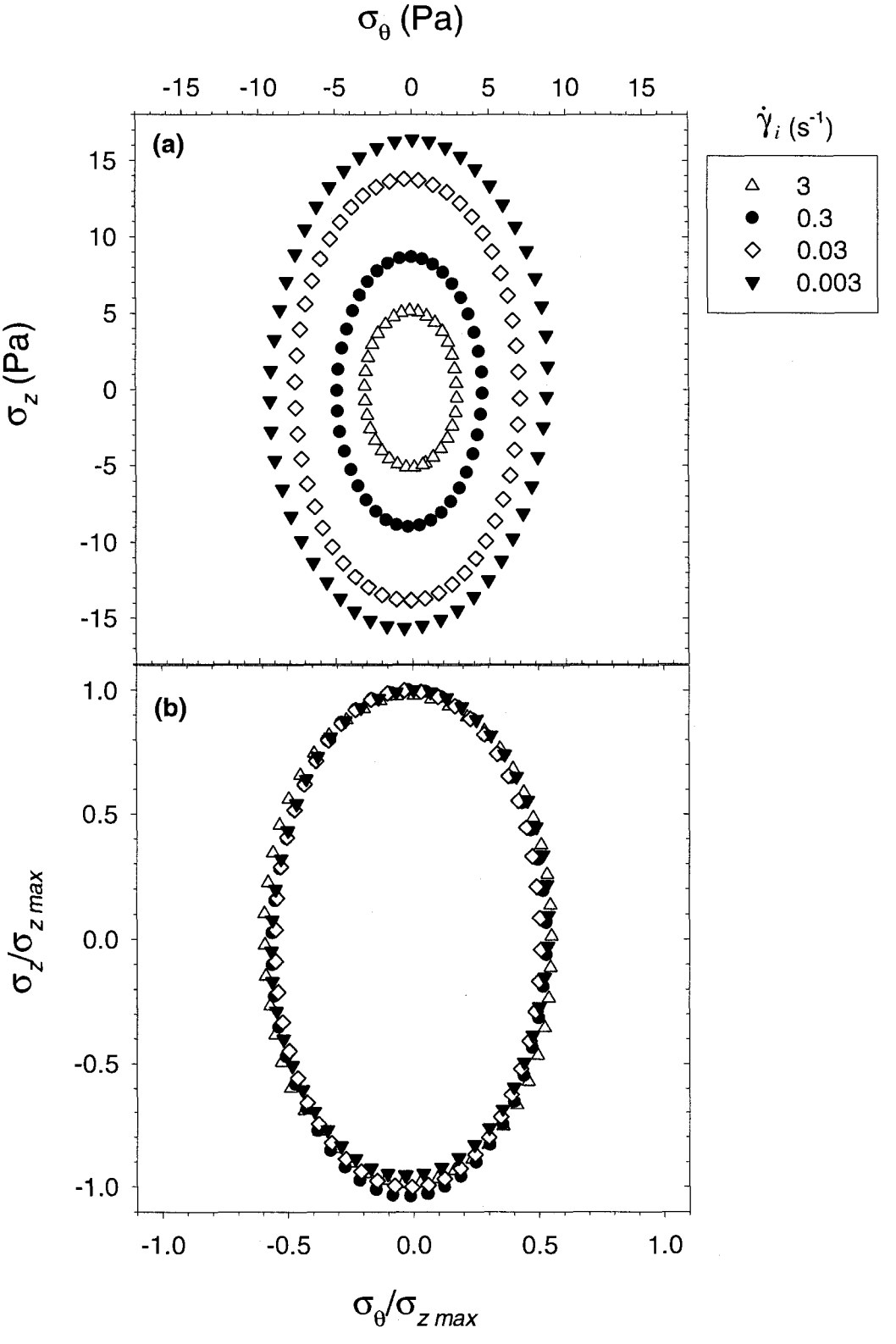
σθ (Pa)
-15 -10 -5 0 5 10 15
(a)
15 10 5 0 -5 -10 -15
σz (Pa)
γ̇i (s-1)
3
0.3
0.03
0.003
(b)
1.0 0.5 0.0 -0.5 -1.0
σz/σz max
-1.0 -0.5 0.0 0.5 1.0
σθ/σz max

Figure 4.12 : Flow history dependency of the 2D SAOS σ_z vs. σ_θ (a) and $\sigma_z/\sigma_{z\,max}$ vs. $\sigma_\theta/\sigma_{z\,max}$ (b) measured at 0.63 rad.s^{-1} and a rest time of 5400 s. $\phi = 0.04$.

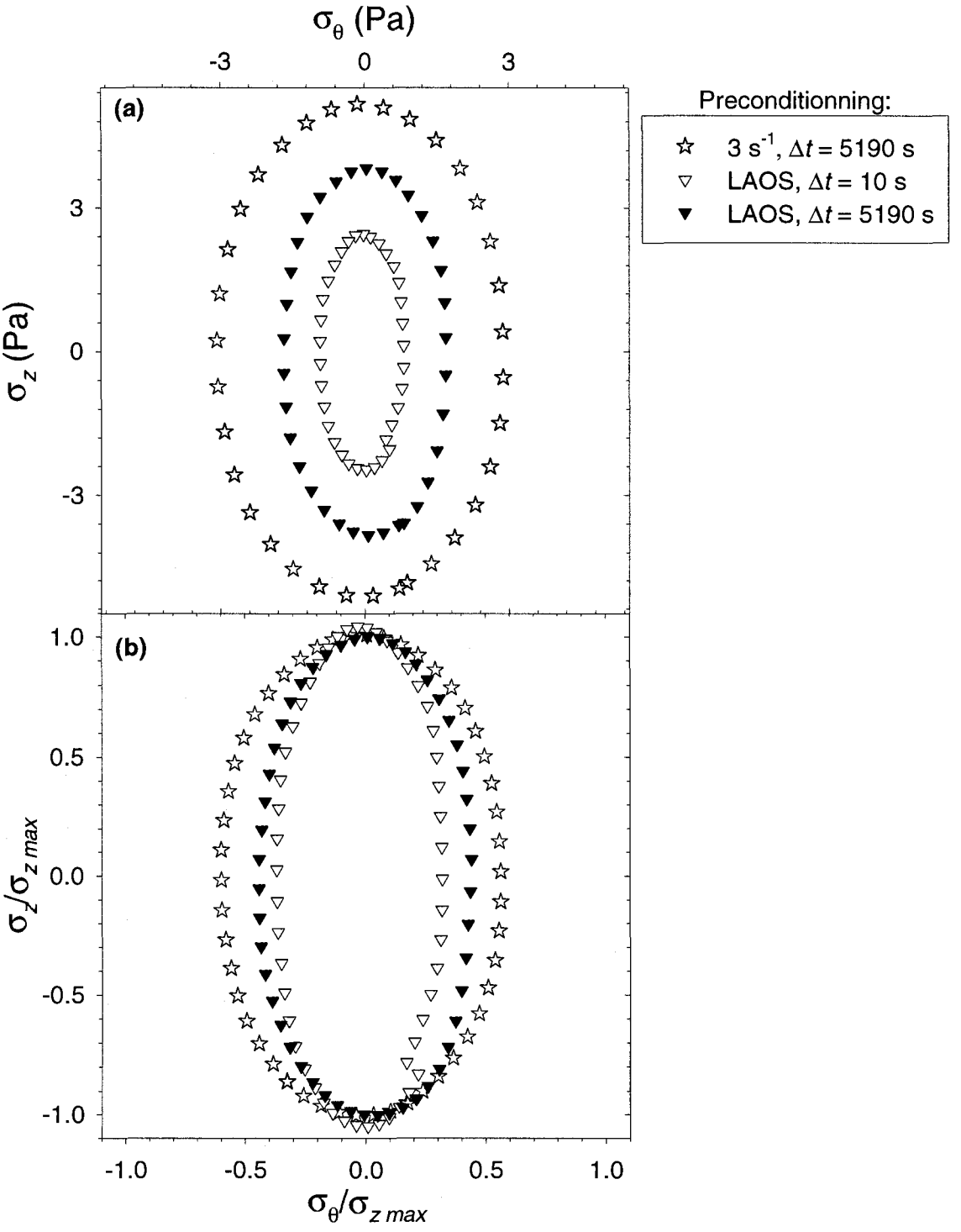
σθ (Pa)
-3
0
3
(a)
3
0
-3
σz (Pa)
Preconditionning:
3 s-1, Δt = 5190 s
LAOS, Δt = 10 s
LAOS, Δt = 5190 s
(b)
1.0
0.5
0.0
-0.5
-1.0
σz/σz max
-1.0
-0.5
0.0
0.5
1.0
σθ/σz max

Figure 4.13 : σ_z vs. σ_θ (a) and $\sigma_z/\sigma_{z\,max}$ vs. $\sigma_\theta/\sigma_{z\,max}$ (b) measured at 0.63 rad.s^{-1} after different pre-shearing conditions and a rest time of 5400 s. $\phi = 0.04$.

Table 4.1 : Dimensions of the doublewall couette cell.

Inner radius cup (mm)	22
Inner radius cylinder (mm)	23
Outer radius cylinder (mm)	24
Outer radius cup (mm)	25
Immersed cylinder length (mm)	50

CHAPITRE 5 - ARTICLE: STRUCTURAL ANALYSIS AND SCALING BEHAVIOR OF NON-AQUEOUS LAYERED SILICATE SUSPENSIONS

Christophe Mobuchon, Pierre J. Carreau* and Marie-Claude Heuzey

Center for Applied Research on Polymers and Composites (CREPEC), Chemical Engineering Department, Ecole Polytechnique, PO Box 6079, Stn Centre-Ville, Montreal, QC, Canada H3C3A7

5.1. Abstract

The scaling behavior with temperature, particle volume fraction, and flow history of the viscoelastic properties of polar and non-polar non-aqueous layered silicate suspensions have been explored and analyzed. Master curves of the linear and nonlinear viscoelastic properties have been obtained using shift factors defined by the low frequency storage modulus and yield stress. Based on fractal scaling theories, the scaling laws of the solid-like properties were ascribed to the presence of space-filling networks made of

---

Cet article a été présenté en partie lors de la 79^{ième} conférence annuelle de la Society of Rheology (S.O.R.) et soumis à la revue Journal of Rheology

clusters with a mass-fractal dimensionality, D_f ~2. Confocal laser scanning microscopy (CLSM) allowed to observe the aggregate networks and to quantify their characteristic microscopic length scale. Under flow, the shear rate dependency of the microstructure characteristic length scale was attributed to a reversible shear-induced aggregation. Finally, the lack of structural recovery at the micro-scale upon cessation of flow has allowed elucidating the flow history dependency of these suspensions.

5.2. Introduction

Colloids and nanoparticles have found increasing uses as rheological modifiers in paints, inks, lubricating greases, cosmetics and pharmaceutical formulations. More recently, layered silicates of the smectite group have attracted great interests as nanoscale fillers for reinforcement of polymers (PNCs) (Patel *et al.* 2006). Due to their particular nature, suspensions based on colloids and nanoparticles are quite complex since they undergo fluid-to-solid transitions with the formation of disordered solids defined by their arrested dynamics and elasticity (Trappe and Sandkuhler 2004).

For attractive colloidal particles, Trappe *et al.* (2001) recently proposed a phase diagram that is a function of the particle volume fraction (ϕ), energy of interparticle attraction, and applied stress. The non-equilibrium solid states of this diagram include two extremes: hard sphere colloidal glasses at high volume fraction, ϕ, and low attractive potential, U, and strongly attractive colloidal gels at low ϕ and high U. For

the limiting case of hard-sphere colloidal particles (for which the interaction potential between spherical particles is determined solely by the excluded volume), the suspensions undergo a liquid-to-glass transition at a volume fraction $\phi_g \sim 0.58$, due to the crowding of single particles. The solid-like properties of colloidal glasses stem from the permanent kinetic trapping of the particles within cages formed by their nearest neighbors (Trappe and Sandkuhler 2004). The resistance to configuration changes of these cages provides a mechanism for energy storage (and viscous dissipation), which gives rise to a low-frequency plateau storage modulus (Crassous *et al.* 2005, Helgeson *et al.* 2007b, Mason and Weitz 1995). Models based on the mode coupling theory (MCT) predict a low-frequency plateau storage modulus (Mason and Weitz 1995), G'_0, scaling with the volume fraction, ϕ, as $G'_0(\phi) \alpha (\phi)^n$ with $n \approx 0.3$ - 0.5 (Götze 1991, Zaccarelli *et al.* 2001).

On the other hand, at low volume fractions, attractive spherical particles aggregate as they form self-similar clusters with a mass, M, scaling with their average size, ξ_c, as $M(\xi_c) \alpha M_0(\xi_c/a_{eff})^{D_f}$, where D_f is the mass-fractal dimensionality, a_{eff} is the characteristic size and M_0 is the mass of the cluster compact building blocks, respectively. Aggregation of clusters ultimately leads to a space-filling network exhibiting macroscopic non-ergodicity (i.e., breakdown in the equivalence of time and space averages) and therefore, to a sol-to-gel transition. The solid-like behavior of colloidal gels originates from the stress bearing network made of close packed clusters. The dependency of the network elasticity on the volume fraction ϕ was shown to be

stronger than predicted for colloidal glasses, with $G'_0(\phi) \alpha (\phi)^n$ and $n \approx 4$ (spherical colloidal particles) (Buscall *et al.* 1988, Khan and Zoeller 1993, Piau *et al.* 1999, Saint-Michel *et al.* 2003, Shih *et al.* 1990, Yziquel *et al.* 1999). Scaling models linking the fractal microscopic structure parameters to the macroscopic elastic properties of gels are presented in detail in the next section. Despite the structural differences between colloidal glasses and gels, their solid-like properties are similar in nature. Both result from the physical jamming or crowding of the characteristic particles within the suspensions: the single particles in the case of glasses, and clusters in the case of gels (Segrè *et al.* 2001).

Between the two limiting cases of glasses and gels, the structure and elasticity of non-equilibrium solid states remains to be investigated. Moreover, suspensions of spherical colloidal particles have attracted a large amount of interest while attractive colloidal suspensions of anisotropic particles have been the subject of fewer investigations. Liquid-to-glass transition of suspensions containing anisotropic colloidal particles is expected at volume fraction much lower than their maximum packing fraction since the excluded volume of anisotropic particles is larger than their actual volume (Jogun and Zukoski 1996, Jogun and Zukoski 1999). The particle anisotropy may also lead to differences associated with their orientation and consequently to a more complex picture of non-equilibrium solid states (Lyatskaya and Balazs 1998).

Layered silicate particles are highly anisotropic. The most commonly used layered silicate is montmorillonite, in which the individual layers are about 1.2 nm thick, 320–

400 nm long and 250 nm wide for the larger ones (Cadene *et al.* 2005). Aqueous layered silicate suspensions undergo phase transitions controlled by repulsive or attractive interactions dependent upon ionic strength and pH. The establishment of their state diagram has gradually emerged during the recent years (Kroon *et al.* 1998, Michot *et al.* 2004, Mourchid *et al.* 1995, Pignon *et al.* 1996, Pignon *et al.* 1998, Pignon *et al.* 1997a, Pignon *et al.* 1997b, Ruzicka *et al.* 2006, Shalkevich *et al.* 2007, Tanaka *et al.* 2005, Tanaka *et al.* 2004, Tombacz and Szekeres 2004). With the increase of ionic strength, clay layers become attractive and the state diagram is expected to gradually follow the jamming phase diagram for attractive particles proposed by Trappe *et al.* (2004). In the same way, non-aqueous layered silicate suspensions belong to attractive colloidal suspensions as the repulsive electrostatic interactions are negligible, and, therefore, should exhibit the non-equilibrium fluid-to-solid transitions of the jamming phase diagram. Note that due to the high aspect ratio of the clay layers, the liquid-to-glass transition is not restricted to high volume fractions and is expected at low volume fractions as well where gelation can occur (see developments of King *et al.* (2007) and Ren *et al.* (2000) for the calculation of ϕ_g). Actually, a fluid-to-solid transition has been observed for polymer layered silicate nanocomposites with the development of a low-frequency plateau storage modulus increasing with volume fraction (see for instances Aubry *et al.* (2005), Lim and Park (2001) and Ren *et al.* (2000)). The non-terminal flow behavior is usually attributed to the formation of a percolated three-dimensional network of clay layers or tactoids and, thus, to a fluid-to-glass transition (Galgali *et al.*

2001, Mitchell and Krishnamoorti 2002, Ren *et al.* 2000). Sol-to-gel transition through the formation of fractal networks has been lately considered (Durmus *et al.* 2007, Vermant *et al.* 2007). Until now, the literature reveals a lack of studies of colloidal attractive suspensions in light of jamming phase diagrams including structural and rheological descriptions of their non-equilibrium states.

In the current paper, we investigate the non-equilibrium solid states of polar and non-polar non-aqueous layered silicate suspensions. At first, the scaling behavior of their viscoelastic properties is explored according to the flow history (stress), the volume fraction, and the temperature (interaction energy). Afterwards, the rheological scaling laws observed are correlated with the clay microstructure. Confocal laser scanning microscopy (CLSM) is also used to verify the existence of a space-filling network and observed length scales are compared with the predictions of fractal scaling theories. Finally, the flow history dependency of layered silicate suspensions reported in a previous publication (Mobuchon *et al.* 2007) is explained by the investigation of the network evolution under flow and at rest.

5.3. Theoretical background

In the framework of fractal scaling theories (Bremer *et al.* 1989, Buscall *et al.* 1988, Shih *et al.* 1990, Wu and Morbidelli 2001), the network structure is considered to result

from the close packing of mass-fractal clusters with an average size ξ_c following a scaling relation with the volume fraction ϕ (Mellema *et al.* 2000):

$$\xi_c = a_{eff}\phi^{1/(D_f-d)} \qquad 1 \leq D_f \leq 3 \tag{5.1}$$

where d is the Euclidian dimension of the system and a_{eff} is the characteristic size of the cluster compact building blocks. The cluster mass-fractal dimensionality, D_f, can be interpreted as a measure of the compactness of the clusters and depends on the mechanism of particle aggregation. A value of 3 for D_f corresponds to uniform dense (non-fractal) clusters, while diffusion-limited aggregation (DLCA) and reaction-limited cluster aggregation (RLCA) lead to a value of 1.8 and 2.1, respectively (Bushell *et al.* 2002). As self-similarity is restricted to length scales below ξ_c, two levels of structure can be distinguished: fractal intra-microstructure of the clusters and inter-microstructure characterized by the cluster interactions.

Recently, Wu and Morbidelli (2001) developed a scaling model, based on the work of Shih *et al.* (1990), to relate the microscopic structure parameters to the macroscopic elastic properties. In their model, the intra- and inter-microscopic contributions to the elasticity are considered in series to give the overall microscopic elasticity, K_{eff}:

$$K_{eff} = {}^{1}/_{K_{\xi_c}} + {}^{1}/_{K_l} \tag{5.2}$$

where K_{ξ_c} and K_l are the intra- and inter-microscopic elastic constants, respectively. According to Shih *et al.* (1990), the elastic properties of a cluster are dominated by its

backbone, which is approximated as a linear chain of springs with a fractal dimension, $1<x<D_f$, different from that of the cluster. The intra-microscopic elastic constant K_{ξ_c} can then be related to ξ_c using the following Khantor–Webman relation (Kantor and Webman 1984, Krall and Weitz 1998):

$$K_{\xi_c} = K_0\left(a_{eff}/\xi_c\right)^{2+x} \tag{5.3}$$

where K_0 is the spring constant of a bond between two cluster compact building blocks. On the other hand, the inter-microscopic elastic constant, K_l, refers to the interactions between the clusters and, therefore, it is independent of the intra-microscopic structure parameters. The macroscopic elastic modulus, G', can be related to K_{eff}, as:

$$G' = \frac{K_{eff}}{\xi_c} = \frac{1}{\xi_c}\frac{K_{\xi_c}}{1+\left(K_{\xi_c}/K_l\right)} \cong \frac{1}{\xi_c}K_{\xi_c}\left(\frac{K_l}{K_{\xi_c}}\right)^{\alpha} \tag{5.4}$$

where α is a constant in the range of [0, 1], which depends on the given range of K_{ξ_c}/K_l. The dependence of G' on ϕ is then derived from Equation 5.5:

$$G' \cong \frac{K}{a_{eff}}\,\phi^{n=\frac{\beta}{d-D_f}} \quad \text{with } \beta = (d-2)+(2+x)(1-\alpha) \text{ and } K = {K_l}^{\alpha}\,{K_0}^{1-\alpha} \tag{5.5}$$

This scaling model was also extended for the strain limit of linearity, γ^0, following the original approach of Shih *et al.* (1990):

$$\gamma^0 \propto \phi^B \qquad \text{with } B = (d-\beta-1)/\left(d-D_f\right) \tag{5.6}$$

In the case of the strong-link regime, where links between the neighboring clusters are stronger than the intra-microscopic links within the clusters, $\alpha = 0$ and Equation 5.6 predicts that the limit of linearity decreases with increasing ϕ. In contrast, γ^0 increases with increasing ϕ for the limiting condition of weak-link regime ($\alpha = 1$) for which the breaking of the network occurs at the intercluster links.

Finally, the two preceding scaling laws (Equations 5.5 and 5.6) lead to the following scaling law for the yield stress, σ_0:

$$\sigma_0 = G'\gamma^0 \propto \phi^{t=\frac{d-1}{d-df}} \tag{5.7}$$

5.4. Materials and methods

5.4.1. Materials and preparation methods

a) Polar suspensions

The polar system used in this study consists of a natural layered silicate, a sodium montmorillonite, $M_x[Al_{2-y}Mg_y]Si_4O_{10}[OH]_2 \cdot nH_2O$, (Cloisite Na^+, Southern Clay products, ρ = 2.86 g/mL), dispersed in a Newtonian polyalkylene glycol, $HO[C_2H_4O]_x[C_3H_6O]_y$-$[C_2H_4O]_xH$, (Plurasafe WT 90000, BASF) of molar mass around 1500 g/mol, viscosity of 59 Pa.s and density of 1.09 g/mL at 25 °C. Clay volume fractions used are comprised between 0.001 to 0.005. The colloidal individual montmorillonite layers can be described as elliptical platelets 1.2 nm thick and lateral

dimensions of 0.25 – 0.4 μm (Cadene *et al.* 2005). The clay was added to the polyalkylene glycol via solution mixing as follows: first, natural clay platelets were exfoliated in deionized water using an ultrasound probe (Sonics & Material) (Ho *et al.* 2001). The pH was adjusted to approximately 9.5 in order to avoid dissolution of the silicate (Thompson and Butterworth 1992). Polyalkylene glycol was then added to the aqueous clay suspension and the entire mixture exposed to ultrasonication before extraction of the deionized water in a high vacuum oven at 40 °C. For a clay volume fraction of approximately 0.001 and larger, the resulting suspensions were homogeneous translucid gels, stable over several months. Other methods aiming at incorporating directly the nanoclay in polyalkylene glycol, based on both sonication and high shear mixing, were observed not to induce gel formation. The mechanical energy involved in these two methods, conjugated with the good affinity between the clay and the polyalkylene glycol, does not suffice to overcome the energy of adhesion between the clay layers and hence hinders the polyalkylene glycol intercalation (Bousmina 2006). For the confocal laser scanning microscopy studies described below the natural clay was tagged with Safranine-O, $C_{20}H_{19}ClN_4$, (Sigma-Aldrich), a fluorescent cationic dye, taking advantage of its cation exchange capacity (CEC). Fluorescent suspensions were prepared using the procedure described above with the addition of an appropriate amount of Safranine-O (equivalent to 5 % of the clay CEC (92.6 mmol/100 g clay)) in deionized water. The low amount of adsorbed Safranine-O

on the clay surface is later shown not to affect noticeably the rheological properties of the suspensions.

b) Non-polar suspensions

The non-polar system is based on a sodium montmorillonite (Cloisite® 15A, Southern Clay products) organically modified with a dimethyl dihydrogenated quaternary ammonium salt, $CH_3CH_3N^+HTHT$, where HT refers to the hydrogenated tallow of various carbon chain lengths: C_{18} (65%), C_{16} (30%) and C_{14} (5%). The longest C_{18} chains have an estimated length of 2.67 nm (Ho *et al.* 2001). A second organomodified montmorillonite (Cloisite® 30B, Southern Clay products) with a methyl dihydroxyethyl, quaternary ammonium salt, $CH_3N^+[CH_2OH]_2$, was also used for comparison. The non-polar suspending fluid selected was a mixture of two Newtonian polybutenes, $R[CH_2CCH_3CH_3]_x[CH_2]_yR$, of different molar mass, respectively 910 g/mol (76.4 mass %, Indopol H100, BP) and 1300 g/mol (23.6 mass %, Indopol H300, BP) with an overall viscosity of 28.5 Pa.s and a density of 0.89 g/mL at 25 °C. Clay volume fractions used are comprised between 0.0075 and 0.04. The non-polar suspensions were prepared following two different procedures, both resulting in stable homogeneous translucid gels. The first procedure consists of incorporating directly the organomodified montmorillonite by ultrasonication. Details about the procedure and characterization of the corresponding dispersions are reported elsewhere (Mobuchon *et al.* 2007). The second procedure via solution mixing from toluene is equivalent to the

procedure described above for the polar suspension. Toluene was selected, since the organomodified montmorillonite can be dispersed in it to yield a transparent gel (Ho *et al.* 2001). The fluorescent organoclay used for the confocal laser scanning microscopy studies was prepared separately from its suspensions. In brief, Safranine-O was dissolved in ethanol/deionized water (1:1) solution and stirred overnight after the addition of organoclay. The treated organoclay was filtered and washed with a hot solution of ethanol in deionized water (1:1 at first and then 4:1) until the filtrate became colorless. The fluorescent organoclay was then dried in a vacuum oven overnight and pulverized into fine powder. The non-polar suspensions based on the resulting fluorescent organoclay were prepared via the previously described ultrasonication and solution mixing methods.

c) Note on particle interactions

In non-aqueous systems, the interaction potential between clay platelets includes short-range van der Waals attraction and forces induced by polymer chains and excluded volume. The potential of the van der Waals forces can be quantified by the Hamaker constant A_H, which is a function of temperature and differences in refractive index and dielectric constants of the two phases. In the case of the non-polar suspensions, a steric barrier to the van der Waals forces is expected due to the compatibility between the surfactant hydrocarbon tails and the suspending fluid. A steric barrier is also expected in polar suspensions with the adsorption, during the solution mixing step, of the

polyalkylene glycol chains on the clay surface. Depending on the extent of steric stabilization, the suspensions can belong to hard solid dispersions, where the van der Waals interactions are negligible relative to the Brownian motion, and in other cases, to the weakly or strongly aggregated dispersions.

5.4.2. Rheometry

The rheological characterization of the suspensions was performed using a stress-controlled rheometer (Anton-Paar, Physica MCR 501). A cone-and-plate geometry with a radius of 50 mm and a cone angle of 0.04 rad was used for the tests performed at 25 °C, while a parallel plate geometry of 50 mm radius was employed for the investigation of the temperature effect. Actually, the true gap option of the MCR parallel plate geometry allows to monitor the gap and to keep it constant while the temperature of the instrument is changing. The steady-shear viscosity was measured by applying stepwise shear rate-decreasing ramps from 25 to 10^{-3} s^{-1}. Linear viscoelastic measurements were conducted at a fixed strain of 0.005, which is below the limits of linearity, γ^0, for all suspensions. The limits of linearity were determined, at a frequency of 6.28 $rad.s^{-1}$, as the strain at which *G'* deviates from its plateau value by 10 %. To ensure controlled initial microstructures (Mobuchon *et al.* 2007), all the dynamic measurements were preceded by a pre-shearing at a defined shear rate $\dot{\gamma}_i$ until steady state was reached, and then followed by a rest time of 5400 s. For the stepwise shear rate measurements, the data were considered after a period of 0.04 s, time required to

reach the specified shear rate within an error of less than 2 %. The standard deviation on the rheological data was estimated to be less than ± 9%. Investigations using various gaps and different roughness values for the parallel plates ruled out slip or wall effects for the two suspensions. However, flow instabilities with sample fracture localized in the middle of the gap was observed for clay volume fractions above 0.005 and 0.03 for the polar and non-polar suspensions, respectively, prepared by solution mixing (this phenomenon was never observed for the non-polar suspension prepared by ultrasonication). The same phenomenon was observed for non-polar suspensions based on low viscosity polybutene mixtures (0.2 and 2 Pa.s) and prepared by ultrasonication. The fracture was observed independently of the gap used and for the entire shear rate range investigated (from 25 to 10^{-3} s^{-1}). At low shear rates, the occurrence of fracture was inferred from the measured stresses, which were smaller than the value for the suspending fluid alone. The identification of the mechanisms leading to sample fracture is beyond the scope of this article, but one may argue that the high elasticity of theses suspensions drives this phenomenon. Hence, all results reported for samples prepared by solution mixing are for volume fractions smaller than the critical values for sample fracture.

5.4.3. Optical measurements

a) Confocal laser scanning microscopy (CLSM)

The large-scale structures of the clay suspensions were directly observed using a confocal laser scanning microscope (Zeiss, Axioplan 2 & LSM 510 META) equipped with a commercial optical shear cell (Linkam Scientific Instruments, CSS450). The homogeneity of the imposed shear flow through the gap was established with a long working distance lens (Leica, 20×/0.33 numerical aperture, n.a.). Higher resolutions oil immersion 40×/1.3 n.a. lens of 0.2 mm working distance (Carl-Zeiss, Plan-Neofluar), and water immersion 40×/1.2 n.a. lens of 0.29 mm working distance (Carl-Zeiss, C-Apochromat) were used to observe the suspension microstructures. The original top plate of the shear cell is not compatible with a low working distance lens due to the thickness of its fixed parallel quartz disc. It was therefore necessary to replace it by a homemade lid with a glass cover of 160 μm depth that acted as the fixed parallel plate. The Safranine-O was excited at 488 nm, and its fluorescence was detected at wavelengths λ above 560 nm through a filter system. The lateral and focal plane resolutions were estimated to be about 0.17 ($\approx 0.4\lambda$/n.a.) and 0.46 ($\approx 1.4\lambda$/n.a.^{2}) μm (Pawley 2006), respectively. The spatial resolution of the images was chosen above the lateral resolution of the CLSM and the dynamic range of their intensity was 8 bits. The time resolution of the CLSM turned out to be enough to acquire images under flow at shear rates up to 0.1 s^{-1} and during relaxation. The real-space images were

quantitatively analyzed to extract their characteristic length scale and to assess their isotropy (Kaufman *et al.* 2005, Lin *et al.* 2007). The image processing consisted firstly in a binarization of gray scale images with the threshold defined by their mean intensity, and pixels with intensity above the threshold were considered to be part of the clay particles. A two-dimensional median filtering using 2-by-2 neighborhoods was then applied to remove "salt and pepper" noise (isolated pixels). The distances, ξ, between nearest neighbors of pixels above the threshold were then determined within each row (x) and column (y). Their distribution, $P(\xi)$, along these directions follows an exponential decay: $P(\xi) \propto \exp\{-2\ \xi/\ \xi_0\}$, where ξ_0 represents an average measure of the spatial correlation at the micro-scale. The same row and column distributions, $P(\xi)$, and density distribution are expected in the case of an isotropic image. Finally, the ratio of the number of pixels above the threshold with the total number of pixels was used to estimate the amount, A, of surface occupied by the clay particles.

5.5. Results and discussion

5.5.1. Scaling behavior with flow history

As previously reported (Mobuchon *et al.* 2007), the linear viscoelastic properties of layered silicate suspensions are strongly correlated with the flow history. This behavior is illustrated in Figure 5.1 for the non-polar suspension prepared by ultrasonication for ϕ = 0.01 (ω = 126.5 rad.s^{-1}). Upon cessation of the steady-shear flow, the storage

modulus, G', is shown to grow from an initial value G'_i to a time invariant value G'_∞ following an exponential form adapted by Mobuchon *et al.* (2007) from Dullaert and Mewis (2005):

$$G'(t) = G'_i + (G'_\infty - G'_i)\left(1 - \exp\left[-\left(\frac{t}{\tau}\right)^m\right]\right) \tag{5.8}$$

with m the stretching exponent, and τ the characteristic time. The values of G'_i and G'_∞ resulting from the data of Figure 5.1 are shown in Figure 5.2a (unfilled and filled circles, respectively) to significantly decrease from high to low plateau values for increasing pre-shearing rate, $\dot{\gamma}_i$. Therefore the non-equilibrium structures under flow, characterized by G'_i, evolve at rest towards different metastable structures with larger elastic modulus G'_∞ values. The effect of the flow history is observed to hold for a wide range of conditions: the initial modulus G'_i and time invariant modulus G'_∞ are reported in Figure 5.2a for various clay volume fractions (0.01 and 0.04), temperatures (25 and 40 °C) and methods of preparation. In order to compare the flow history dependency for these various conditions, the moduli have been normalized using the data of Figure 5.1 (measured for a volume fraction of $\phi = 0.01$ and $T = 25$ °C). The normalized moduli are plotted in Figure 5.2a as functions of the pre-shearing rate, expressed in terms of the initial Peclet number, $Pe_i = \dot{\gamma}_i/D_r$, where $\dot{\gamma}_i$ is the pre-shearing rate and D_r the rotary diffusion coefficient. The rotary diffusion coefficient (Ren *et al.* 2003) of the clay layers is given by $D_r = 3k_BT/4\eta d^3$, where k_B is the Boltzmann constant, T is the absolute temperature, η is the viscosity of the suspension

at high shear rate (Moan *et al.* 2003) and d is the particle diameter. The smaller volume fraction (0.01) is close to the fluid- to solid-like transition of the suspension (shown later), while the higher temperature (40 °C) leads to an increase by almost three times of D_r. Nevertheless, the flow history dependency of G'_i and G'_∞ shows no significant qualitative differences for this range of parameters, while the same trend is observed for the non-polar suspension prepared by solution mixing (triangular symbols). In a similar fashion, the linear viscoelastic properties of the polar suspension (Figure 5.2b) are sensitive to the flow history, but differ in the extent of the structural recovery that tends to vanish as the pre-shearing amplitude decreases. It is noteworthy to mention that a similar flow history dependency was also observed for organo-modified suspensions prepared by ultrasonication with synthetic layer silicates of different aspect ratios, p, (results not shown): a hectorite with $p \approx 50$ (Lucentite SANS, CBC Co.) and a fluoromica with $p \leq 6000$ (Somasif MAE, CBC Co). This behavior appears to be a universal feature of strongly concentrated attractive colloidal suspensions.

As a consequence of the flow history dependency, the polar and non-polar suspensions undergo a fluid- to solid-like transition due to pre-shearing. The transition is depicted in Figure 5.3 where their linear viscoelastic properties as a function of frequency are reported after different initial shear rates $\dot{\gamma}_i$. The low frequency elastic modulus of the non-polar (Figure 5.3a, $\phi = 0.04$) and polar suspensions (Figure 5.3b, $\phi = 0.003$), measured after a 5400 s rest time, is actually shown to evolve from a liquid-like behavior for high pre-shearing rates towards a non-terminal flow behavior (i.e. nearly

independent of ω) as the initial shear rate is decreased. Note that the volume fraction of the polar suspension is about 9 times smaller than that of the non-polar one. Despite the large dependence of the low frequency elastic modulus on the pre-shearing rate (more than two fold increases for the polar suspension), the elastic and loss moduli of the non- and polar suspensions can be respectively scaled in two single master curves (Figure 5.3c). For each suspension, an excellent superposition of the viscoelastic data of Figure 5.3a and Figure 5.3b is achieved when a shift factor, κ, is used to reduce the modulus and the frequency (not shown). This shift factor, κ, is defined as the ratio of G'_0 and a reference modulus, G'_{0r}, following a pre-shear rate, $\dot{\gamma}_{ir}$. For these suspensions, G'_0 reflects the elasticity induced by the presence of the clay particles since the suspending fluids are inelastic. Then, the crossover frequency, ω_{0r}, (i.e. where both moduli are equal) and G'_{0r} are used to make single master curves as reported in Figure 5.3c. This scaling behavior suggests strong similarities between the metastable microstructures induced by different pre-shear rates and between those of the polar and non-polar suspensions

5.5.2. Scaling behavior with volume fraction

Figure 5.4a shows the frequency dependence of the elastic modulus at various volume fractions, ϕ, ranging from 0.0075 to 0.04 for the non-polar suspension prepared by ultrasonication. Prior to all measurements, the samples were systematically pre-sheared at a low initial Peclet number ($Pe_i < 1$, $\dot{\gamma}_i = 10^{-3}\ s^{-1}$), and then allowed to rest during

5400 s to ensure similar flow history. As the volume fraction increases, the elastic modulus becomes significantly larger and displays a wider plateau at low frequencies, characterized by G'_0. The dependence of the plateau value, G'_0, on ϕ will be discussed further in relation to the nature of the clay network. An excellent superposition of the linear viscoelastic properties with the volume fraction is obtained, based on the scaling factor κ as shown in Figure 5.4b. In this case, κ is defined as the ratio of G'_0 and a reference modulus, G'_{0r}, corresponding to a volume fraction, ϕ_{ref}, arbitrarily chosen equal as 0.02. This scaling is similar to that reported by Hobbie *et al.* (2007) for concentrated nanotube suspensions. It is also in agreement with the universal scaling behavior of weakly attractive particles discussed by Trappe *et al.* (2000; 2001). Figure 5.5 shows that the scaling behavior applies for all the data obtained under various pre-shearing rates, preparation methods and different suspensions. For the non-polar suspension ($\phi_{ref} = 0.02$), the superposition of the data following a pre-shearing at a high initial Peclet number, $Pe_i > 1$ ($\dot{\gamma}_i = 0.3\ s^{-1}$), only differs at low frequencies compared to the case at the low Peclet number, $Pe_i < 1$ ($\dot{\gamma}_i = 10^{-3}\ s^{-1}$), with G' going towards a lower G'_0, in agreement with the results of Figure 5.3. Also, for the non-polar suspension with $Pe_i < 1$, the preparation method based on solution mixing ($\phi_{ref} = 0.02$) leads to a larger G'_0 in comparison with the preparation method based on ultrasonication. Rather surprisingly, the reduced storage modulus of the polar suspension shows a similar behavior than that of the non-polar suspensions, while the reference volume fraction is

nearly ten times smaller ($\phi_{ref} = 0.003$). Note that for the fluorescent suspensions used in CLSM, the low-frequency data of G' are unaffected by the presence of Safranine-O (Figure 5.5), suggesting that it does not perturb the interaction potential between the clay platelets.

Finally, a scaling is proposed for the steady-state data (stress vs. shear rate), this time suggested by the Bingham equation and based on the apparent yield stress. Actually, the behavior of the layered silicate suspensions is typical of a yield stress material, as described by the Bingham equation: $\sigma = \sigma_0 + \mu_0\dot{\gamma}$, where σ, σ_0 and μ_0 are the steady stress, the apparent yield stress and the high-shear rate viscosity of the suspension, respectively. The shift factor, $\zeta = \sigma_0/\sigma_{0|\phi_{ref}}$ where $\sigma_{0|\phi_{ref}}$ is the apparent yield stress for the reference volume fraction, is applied to reduce the steady stress σ and the shear rate $\dot{\gamma}$. Figure 5.6 shows that the scaling reduce effectively the data of the non-polar suspensions prepared by ultrasonication and by solution mixing in single master curves ($\phi_{ref} = 0.02$). On the other hand, the yield stress for the polar suspensions was not well defined and it was deduced from the scaling procedure itself. A similar scaling behavior was observed for concentrated nanotube suspensions by Hobbie and Fry (2007) and is expected for other Bingham fluids (Trappe and Weitz 2000). The values of the plateau storage modulus G'_0 and of the yield stresses σ_0 used to calculate the shift factors, κ and ζ, are plotted in Figure 5.7a as functions of the clay volume fraction, while Figure 5.7b presents the limit of linearity γ^0 of the two suspensions. The

similarity within the behavior of these suspensions is discussed in the scope of the microstructure in Section 4.

5.5.3. Scaling behavior with temperature

The significant effect of temperature, T, on the non-equilibrium structures of the non-polar suspension prepared by ultrasonication ($\phi = 0.04$) and the polar suspension ($\phi = 0.003$) is illustrated in Figure 5.8. The stress, σ, reduced by contribution of the suspending fluids, σ_m, is plotted at different temperatures as a function of the Peclet number. Since the suspending fluids are Newtonian, the reduced stresses correspond to the contributions of the clay structures. The Peclet number was selected since it allows comparing reduced stresses at different temperatures for the same ratio of the hydrodynamic ($\dot{\gamma}\eta$) and Brownian ($3k_BT/4d^3$) forces. The hydrodynamic contributions vary considerably over the temperature range covered experimentally. This is principally due to the viscosity changes of the suspending fluids with temperature (multiplied by ~8 and ~5 for the non- and polar suspensions, respectively, when the temperature is decreased from 65 to 15 °C), while the Brownian force is only slightly affected. The non-superposition of the reduced stresses brings out the strong temperature dependency of the interaction potential between the clay platelets. The yield stress, and hence, the attraction potential (Trappe *et al.* 2001) are shown to increase with decreasing temperature for both suspensions. In the same manner than for the volume fraction, the shift factor ζ based on yield stress allows to superpose the flow

curves at different temperatures (filled symbols in Figure 5.7 with T_{ref} = 40 °C and 65 °C for the non- and polar suspensions, respectively). It will be shown below that, remarkably, the shift factors ζ of the non- and polar suspensions follow the same exponential decay dependency with temperature.

To investigate the effect of temperature on the metastable structures, the frequency dependency of the elastic modulus was measured in the same temperature range as the stress measurements and the results are reported in Figure 5.9. All the dynamic measurements were preceded by a pre-shearing followed by a 5400 rest time. For the non-polar suspension, two pre-shearing amplitudes were tested with initial Peclet numbers equal to 1 and 10^3, while a pre-shearing at $Pe_i < 1$ with $\dot{\gamma}_i = 10^{-3}$ s^{-1} was used for the polar suspension. The variation of G' induced by the temperature dependency of the suspending fluid was taken into account by applying time-temperature superposition. For that reason, the data were horizontally shifted with the respective factors a_T of the suspending fluids, relative to the reference temperature, T_{ref}, of 25 °C. The non-superposition of the plateau storage modulus, G'_0, at low frequencies shown in Figure 5.9a for both suspensions reflects structure differences with temperature. However, in Figure 5.9b the data are shown to scale in single master curves using the shift factors a_T of the suspending fluids and κ. The shift factors κ for the non-polar suspension following a pre-shearing at high ($Pe_i = 10^3$) and low Peclet ($Pe_i = 1$) number and for the polar suspensions ($Pe_i < 1$) are reported in Figure 5.10, along with the shift factors ζ used for the non-equilibrium structures (used in Figure 5.8). Both shift factors

are shown to follow the same exponential decay dependency with temperature within measurement accuracy, but they are not equal for all conditions investigated. Nevertheless, the temperature dependencies of the polar and non-polar suspensions as well as the temperature dependencies of the equilibrium and non-equilibrium structures are similar. The main difference between the polar and non-polar suspensions lays in the fact that the polar suspensions exhibit a non-reversible behavior with temperature. This is illustrated in Figure 5.9a for the G' data obtained after measurements performed at 45 and 65 °C (labelled respectively as "after 45'' and "after 65''). Following these measurements, a second pre-shearing at 25 °C was applied at the same Peclet number. We observe a significant decrease of the elastic modulus with respect to the initial 25 °C measurements. We note that the storage modulus remains at the same level as observed after pre-shearing at higher temperature, suggesting the persistence of the structures induced at high temperature. This behavior is unexplained. In contrast for the non-polar suspensions, the resulting storage modulus remains at the same level as observed after the first pre-shearing. Finally, it should be pointed out that under static conditions, i.e. when the temperature is just held at 65 °C without shearing after the first at 25 °C, the same suspension was observed to be reversible (results not shown).

5.5.4. Correlation between rheological properties and microstructure

The power-law dependencies of G'_0 and of the apparent yield stress, σ_0, on the volume fraction depicted in Figure 5.7a suggest that the microstructures of the polar and non-

polar suspensions are fractal in nature. The scaling exponents n for G'_0 and t for σ_0 of the two suspensions do not differ much within their determination accuracy (see Table 5.1). Note that the two different pre-shearing conditions (low and high Pe_i) lead to similar exponents n. The limit of linearity of γ^0 for the two suspensions is also shown to follow a power-law relationship with the volume fraction (Figure 5.7b) with a negative exponent B (Table 5.1). As mentioned earlier, the limit of linearity was established according to the variation of G' with strain. Above γ^0, while G' decreased continuously, G'' exhibited a maximum (results not shown). This behavior was reported by Yziquel *et al.* (1999) for fumed silica suspensions and by Page *et al.* (2002) for coating colors. The maximum (overshoot) was observed to strongly decrease with increasing frequency and decreasing volume fraction. It allows classifying the nonlinear viscoelastic behavior of these suspensions to type III or weak strain overshoot, according to Hyun *et al.* (2002). From the fractal scaling theory of Shih *et al.* (1990), a decrease of γ^0 with increasing volume fraction indicates that the elasticity of the system is ruled by the intra-microscopic elasticity K_{ξ_c}, which is lower than the inter-microscopic elasticity K_l. However, in the case of our suspensions the volume fraction dependency of γ^0 is weak, which suggests mutual contributions of the two levels of elasticity. Actually, the theory of Shih *et al.* (1990), which only considers K_{ξ_c} in the strong-link regime, fails by predicting an unphysical negative value for the fractal dimension x of the clusters in the case of our suspensions. On the other hand, the

scaling model of Wu and Morbidelli (2001) takes into account the two levels of elasticity with a parameter α ranging from 0 to 1 for the strong-link and the opposite weak-link regime, respectively. The determined power-law exponents n and B lead for the two suspensions to $\alpha \gtrsim 0.4$ if a realistic value of the fractal dimension x is considered (in the range of 1 to 1.3 for a colloidal gel). Consequently, the two suspensions belong to the transition regime for which both levels of elasticity contribute significantly to the overall elasticity. The values of the fractal dimensionalities D_f of the two suspensions derived from Equations 5.5 and 5.6 are close to 2 (see Table 5.1). This supports the fact that their structures are similar. They are also in good agreement with the predictions only based on yield stress (Equation 5.7 and Table 5.1).

Real space observations of the microstructures of the non- and polar suspensions were done using confocal laser scanning microscopy (CLSM). Figure 5.11 shows microstructural images from CLSM when no pre-shearing, except a slight squeezing flow to insert the sample within the CLSM holder gap, was imposed prior to their acquisition. The areas rich in fluorescent layered silicate appear bright in the micrographs. The dense regions in layered silicate within the non-polar suspensions prepared either by ultrasonication (Figure 5.11a, ϕ = 0.02) or by solution mixing (Figure 5.11b, ϕ = 0.02), and the polar suspension (Figure 5.11e, ϕ = 0.003), form a continuous network with an overall appearance similar to those reported for polymer gels (Bremer *et al.* 1993, Crompton *et al.* 2005, Firoozmand *et al.* 2007, Hirokawa *et*

al. 1999). The space-filling networks are consistent with the fractal structures inferred previously. At the micro-scale, these networks were shown to be static over the time scale of observation (~ 60 min), indicating the dominance of prevailing attraction forces over Brownian forces. It is also noteworthy to mention that the non-polar suspension based on the more polar organomodified montmorillonite (Cloisite 30B) did not exhibit such networks (Figure 5.11d). At the same volume fraction $\phi = 0.02$, the microstructure of the non-polar suspension prepared by ultrasonication (Figure 5.11a) is shown to contain some large agglomerates in contrast to the suspension prepared by solution mixing (Figure 5.11b). The clay platelets contained within these agglomerates do not contribute to the network, which explains the weaker rheological properties reported previously for this suspension (Figure 5.5 & Figure 5.6). By considering Equation 5.5 with the low plateau value of the storage modulus G'_0 given in Figure 5.5 (with $Pe_i < 1$) and assuming the same fractal dimensionality D_f and similar β (Table 5.1) for both suspensions, the network induced by ultrasonication is expected to include only approximately one half of the total clay volume fraction. Consequently, and due to its fractal nature, it should have a characteristic length scale, ξ_0, larger than that of the network prepared by solution mixing (Equation 5.1, assuming ξ_0 proportional to ξ_c (Gefen *et al.* 1981)). Its coarser microstructure observed by CLSM (Figure 5.11a vs. Figure 5.11b) qualitatively confirmed this trend, but this should be considered with care since the two preparation methods involve different flow histories. In the next paragraph, the microstructure characteristic size ξ_0 is actually observed to depend on

the pre-shearing rate. Similarly, a more open network is seen when the volume fraction of the non-polar suspension is decreased by half to 0.01 (Figure 5.11c compared to Figure 5.11b). In contrast, the polar suspension exhibits the same behavior when the volume fraction is decreased from 0.003 (Figure 5.11e) to 0.0015 (Figure 5.11f). Figure 5.12 presents the distance distribution function, $P(\xi)$, used to quantify the network characteristic length scale ξ_0 of the CLSM images of Figure 5.11. The observable isotropy of the quiescent microstructures is confirmed by the similarity of the ξ distributions along the x- and y-directions. The corresponding characteristic length scales, ξ_0, (shown in the legends of Figure 5.12a & Figure 5.12b) are in agreement with the main concept of fractal scaling theories described by Equation 5.1. Actually, according to this equation and the mass-fractal dimensionalities, D_f, given in Table 5.1, an increase by a factor of two of the volume fraction would result in a decrease of ξ_0 by a factor of 0.5 and 0.6 for the polar- and non-polar suspensions prepared by solution mixing, respectively. These theoretical factors are in close agreement with their corresponding experimental factors equal to 0.5 ± 0.05 for the two suspensions. In addition, the order of magnitude of the characteristic length scales, ξ_0, of the non-polar and polar suspensions are similar while the volume fraction range for the polar suspension is one decade smaller. The differences in the range of volume fractions result in different sizes a_{eff} of the compact building blocks of the clusters, as calculated from Equation 5.1. This equation predicts that the compact building blocks of the non-

polar suspension are almost three times larger than those of the polar suspension (ratio of Equation 5.1 for the non- and polar suspensions estimated from ξ_0 of Figure 5.12 and the fractal dimensions from Table 5.1). This is attributed to differences in the nanoscale interactions between the particles during the solution mixing step in preparing the suspension. Actually, it has been shown that the organomodified clay in toluene forms tactoids of three to six platelets whereas the natural clay is fully exfoliated in deionized water (Ho *et al.* 2001, Ho *et al.* 2002, Ho and Glinka 2003). Finally, the comparable rheological properties of these suspensions observed on different volume fraction ranges are explained by differences in the elastic constant *K*. From Equation 5.5 and using the scaling exponents and fractal dimensions given in Table 5.1, one obtains the elastic constant *K* for the polar suspension nearly one hundred times larger than for the non-polar suspension. Assuming that the elasticity is governed by the interaction potential between particles and clusters (Pantina and Furst 2006), the interaction potential level within the polar suspension is therefore much higher than that within the non-polar suspension.

Figure 5.13 reports micrographs for the metastable microstructures of the non-polar suspension prepared by solution mixing (ϕ = 0.02) and polar suspension (ϕ = 0.003) following various pre-shearing rates $\dot{\gamma}_i$ from 10 to 10^{-2} s^{-1}. Their elasticity is given by G'_∞ in Figure 5.2. These metastable microstructures reflect their corresponding non-equilibrium microstructures, since no overall structural recovery at the micro-scale was observed in CLSM upon cessation of steady shear flow. Therefore, the structure build-

up at rest resulting in the increase of G' from G'_i to G'_∞ depicted in Figure 5.1 is due to local rearrangements at smaller length scales. The lack of micro-structural recovery towards a single equilibrium structure outlines the high interparticle attraction energy (> 20 k_BT), a characteristic of strongly aggregated systems. On the shear rate range investigated, from 10^{-2} to 10 s^{-1}, the metastable microstructures of the polar suspensions display no apparent anisotropy, while for the non-polar suspension a slight one along the vorticity direction is distinguishable, with the difference in the ξ distributions along the x- and y-directions. A constant surface coverage by the structure was also observed on the shear rate range explored, with A (described in the optical measurement section) equal to 0.48 ±0.02 and 0.39 ±0.02 for the non- and polar suspensions, respectively. The metastable structures and, hence, the non-equilibrium structures differ essentially from each other by their characteristic length scale, ξ_0, which tends to decrease for increasing pre-shearing rate amplitude $\dot{\gamma}_i$ as revealed quantitatively in Figure 5.14. A comparable aggregation process was recently reported by Rahatekar *et al.* (2006) for a carbon nanotube suspension in epoxy. The dependency of the rheological properties with the pre-shearing and shearing amplitudes (Figure 5.2, Figure 5.3 & Figure 5.8) results consequently from the shear-controlled characteristic length scale of the microstructure, as supported by the strong correlation between G'_∞ (Figure 5.2) and ξ_0 (Figure 5.14). This structural dependency is attributed to a reversible shear-induced aggregation. As a result, ξ_0 follows a power-law dependency at intermediate shear rates with a power exponent m = - 0.22 for the non-polar suspension and m = - 0.42 for the

polar suspension. Sonntag and Russel (1986; 1987) have reported a value of m = - 0.35 for their dilute flocculated suspensions (polystyrene lattices). These values are within the limits of - 0.23 and - 0.5 determined by Potanin (1993) using computer simulations. The low limit is related to the non-central components of the particle attraction potential (function of the angle between adjacent bonds), while the high limit belongs to the purely central component (function of the distance between the centers of neighboring particles).

The shear-induced aggregation has been directly visualized during stepwise reductions in shear rate from 10 to 10^{-2} s^{-1}. Figure 5.15 reports the resulting transient stress response, σ^-, and characteristic length scale, ξ_0, as a function of strain for the polar suspension (ϕ = 0.003). The first decrease in σ^- at short times, corresponding to the viscoelastic response of the suspension (stress relaxation), is followed by a monotonic increase as ξ_0 starts to increase due to the shear-induced aggregation. The transient stress response at large deformations is therefore shown to be governed by a structural evolution at the micro-scale. Similar observations have been made for the non-polar suspensions.

5.6. Concluding remarks

Motivated by the jamming phase diagram for attractive particles proposed by Trappe *et al.* (2001), we have investigated the scaling behavior of the viscoelastic properties of

non-aqueous layered silicate suspensions with flow history (stress), volume fraction, and temperature (interaction energy). Single master curves of their linear and nonlinear viscoelastic properties have been obtained using respectively a shift factor κ based on low frequency plateau values of the elastic modulus G'_0, and a shift factor ζ derived from the yield stress σ_0. The scaling is established for both the non- and polar aqueous layered silicate suspensions.

The power-law dependencies of the shift factors with the volume fraction have been interpreted in light of the fractal nature of the suspensions. Fractal dimensions close to 2 were estimated using the scaling model of Wu and Morbidelli (2001). Direct observations of the microstructures using confocal laser scanning microscropy (CLSM) confirmed the presence of fractal networks with fractal dimensions ~2. As far as we are aware, such CLSM observations for colloidal suspensions under shear flow have never been reported. The similar rheological properties of the non-polar and polar suspensions, while the volume fraction range for the polar suspension was ten times smaller, was explained to arise from differences in particle interaction potential.

The attraction potential responsible for the fractal networks was clarified owing to its temperature dependency. The exponential decay of the shift factors with temperature was shown to be similar for the two suspensions. Nevertheless, the polar suspension differs from the non-polar suspensions by its non-reversible temperature behavior under flow.

By increasing the shearing amplitude, the characteristic length scale of the non-equilibrium microstructures was shown to decrease from high to low plateau values. This structural variation with the shearing amplitude was attributed to a reversible shear-induced aggregation. Upon cessation of flow, no overall structural recovery at the micro-scale was observed in CLSM, leading to metastable microstructures with the same characteristic length scale than their non-equilibrium counterparts. Consequently, the thixotropic behavior of these suspensions is due to local rearrangements at the nano-scale and its physical interpretation should be elucidated using wide-angle scattering techniques. Based on these findings, the rheological dependency on the flow history is attributed to the shear-controlled characteristic length scale of the microstructure.

5.7. Acknowledgements

The authors are most grateful to Dr. N. Tran-Khanh and Dr. M. Thibault for their precious help with CLSM experiments. We also thank Professor M. Bousmina for the use of the shear cell facility. One of the authors (C.M.) is thankful to Alcan Inc. for a scholarship. Southern Clay Products kindly provided materials used in this study. Finally, financial support from NSERC (Natural Science and Engineering Research Council of Canada) and from FQRNT (Fonds Québécois de Recherche en Nature et Technologies) is gratefully acknowledged.

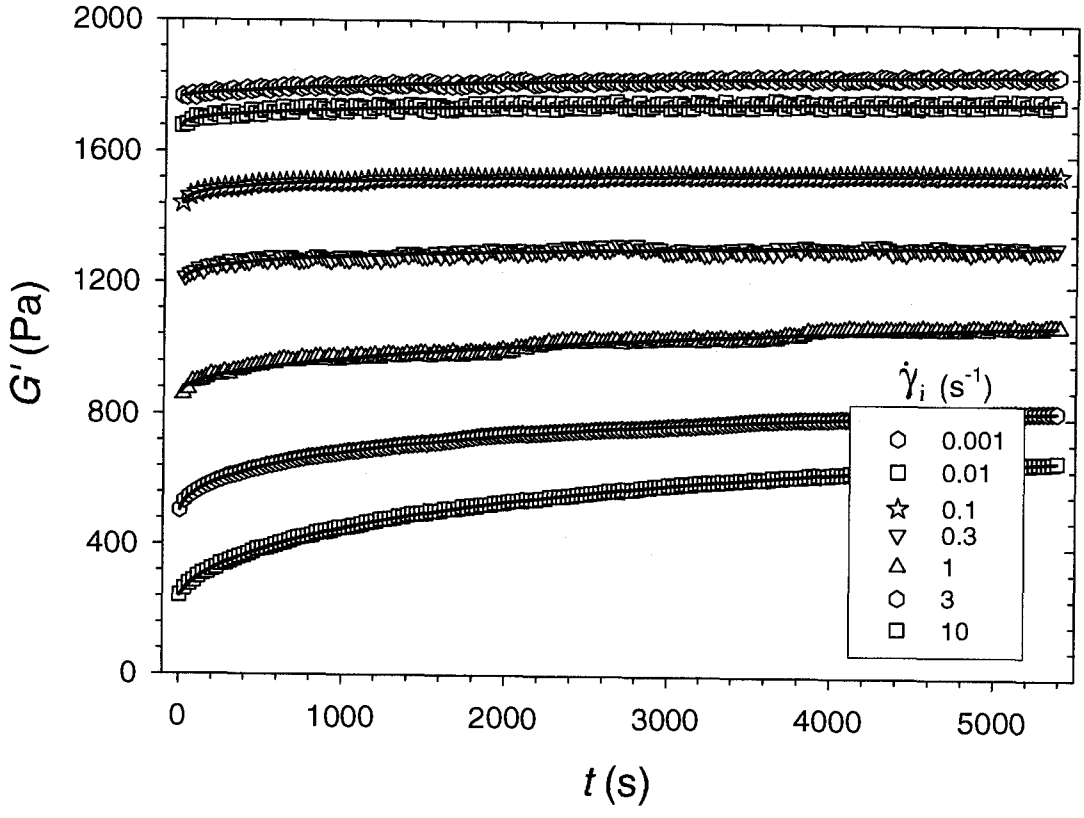

Figure 5.1 : Thixotropic behavior of the non-polar suspension prepared by ultrasonication for ϕ = 0.01. G' as a function of time, t, measured at a frequency of 125.6 rad.s^{-1} upon cessation of steady shear flow. Symbols indicate the values of the initial shear rate $\dot{\gamma}_i$ of steady shear flow; the solid lines represent best fits using Equation 5.8.

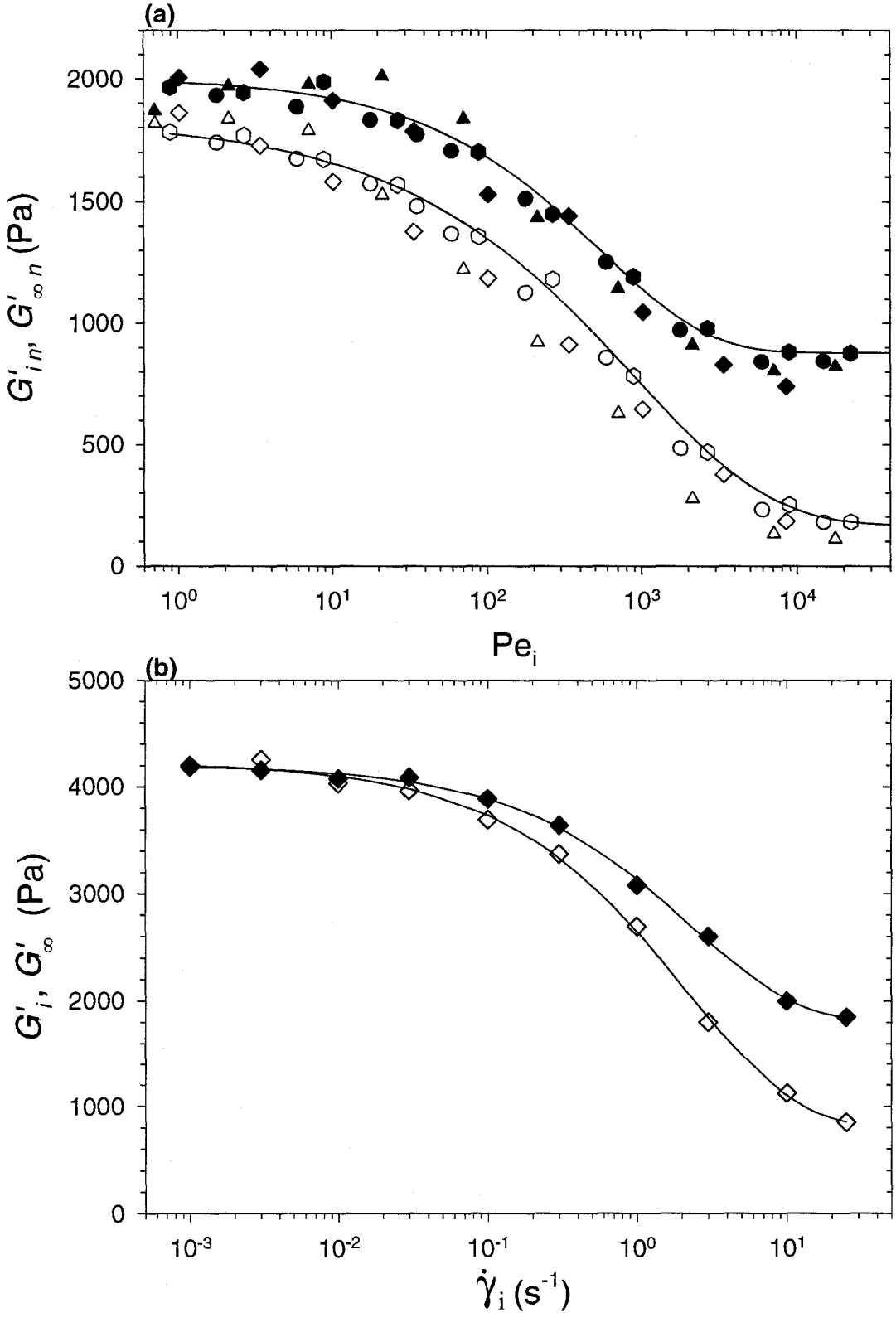
(a)
2000
1500
1000
500
0
G'_{in}, $G'_{\infty n}$ (Pa)
10^0
10^1
10^2
10^3
10^4
Pe_i
(b)
5000
4000
3000
2000
1000
0
G'_i, G'_∞ (Pa)
10^{-3}
10^{-2}
10^{-1}
10^0
10^1
$\dot{\gamma}_i$ (s^{-1})

Figure 5.2 : Dependence of G'_i (unfilled symbols) and G'_∞ (filled symbols) on the pre-shearing amplitude (normalized data). Non-polar suspension (a) prepared by ultrasonication for $\phi = 0.01$ and $T = 25\ ^{o}C$ (circle, taken as reference), $\phi = 0.04$ and $T = 25^{o}C$ (hexagon), $\phi = 0.04$ and $T = 40\ ^{o}C$ (diamond) and prepared by solution mixing with $\phi = 0.02$ and $T = 25\ ^{o}C$ (triangle). Polar suspension prepared by solution mixing (b) with $\phi = 0.003$. All measurements were done at 126.5 $rad.s^{-1}$. The solid lines are drawn to guide the eyes.

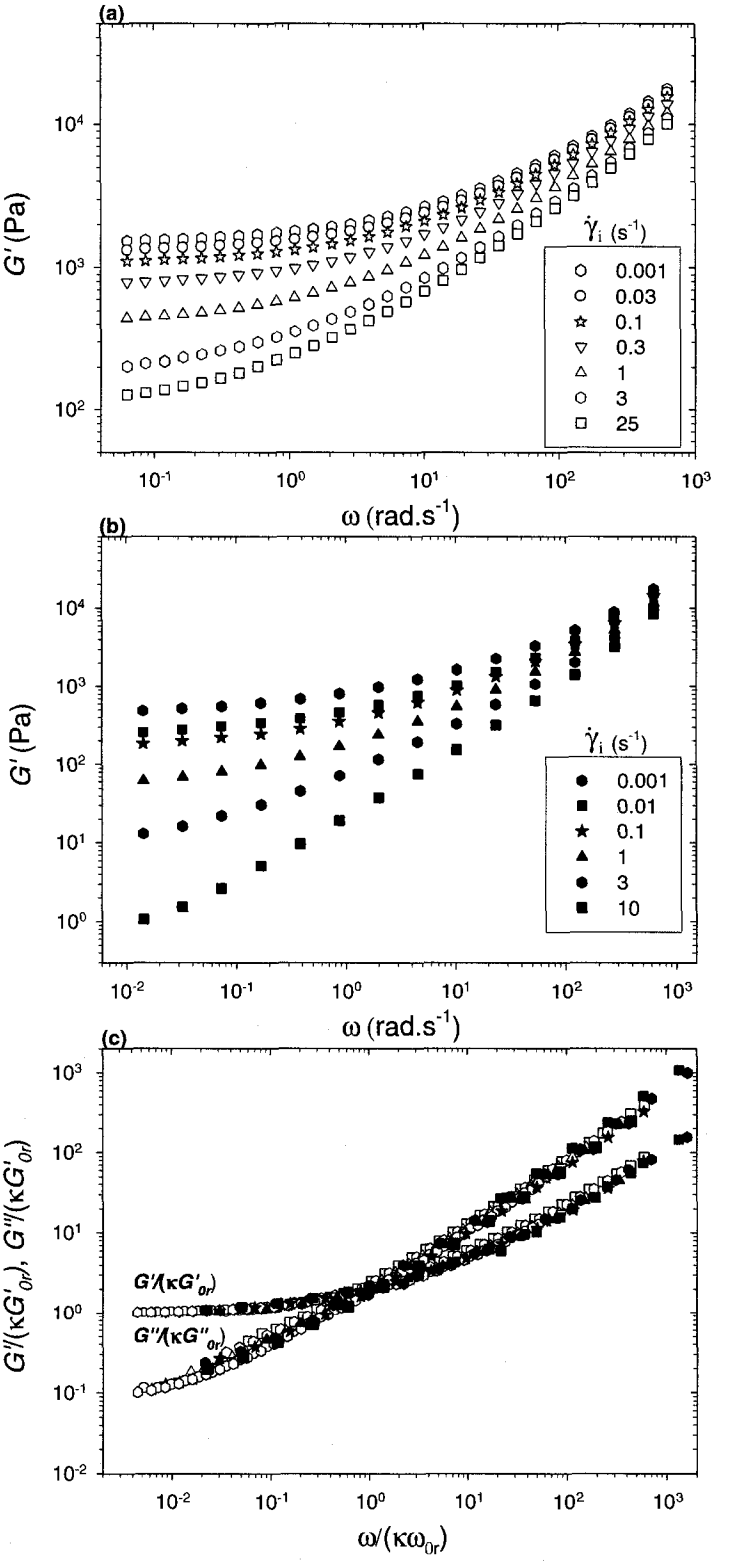
(a)
G' (Pa)
ω (rad.s-1)
γ̇i (s-1)
0.001
0.03
0.1
0.3
1
3
25
(b)
G' (Pa)
ω (rad.s-1)
γ̇i (s-1)
0.001
0.01
0.1
1
3
10
(c)
G'/(κG'0r), G''/(κG'0r)
G'/(κG'0r)
G''/(κG''0r)
ω/(κω0r)

Figure 5.3 : Flow history dependency of linear dynamic moduli (a & b) and their scaling behavior (c). Non-polar suspension prepared by ultrasonication for $\phi = 0.04$ (unfilled symbols) and polar suspension prepared by solution mixing for $\phi = 0.003$ (filled symbols). $T = 25\ ^{o}C$.

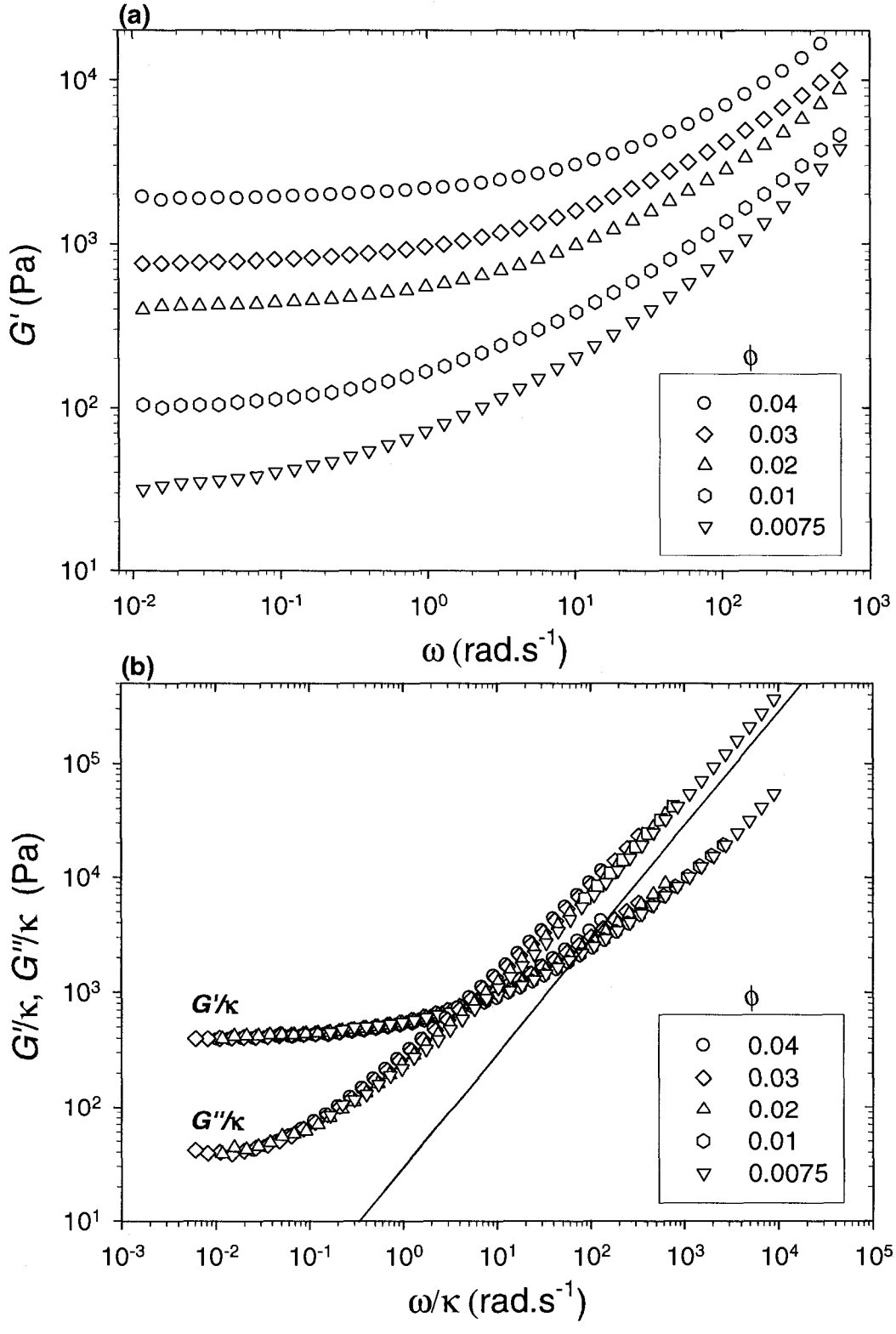
(a)
G' (Pa)
ω (rad.s-1)
ϕ
0.04
0.03
0.02
0.01
0.0075
(b)
G''/κ, G''/κ (Pa)
G'/κ
G''/κ
ω/κ (rad.s-1)
ϕ
0.04
0.03
0.02
0.01
0.0075

Figure 5.4 : Viscoelastic properties of the non-polar suspension prepared by ultrasonication for different volume fractions ϕ. G' as a function of ω (a) and scaled moduli, G'/κ and G''/κ, as a function of the scaled frequency, ω/κ (b) ($\phi_{ref} = 0.02$ and $Pe_i < 1$). The solid line in the bottom figure represents the loss modulus of the suspending fluid. $T = 25\ ^{o}C$.

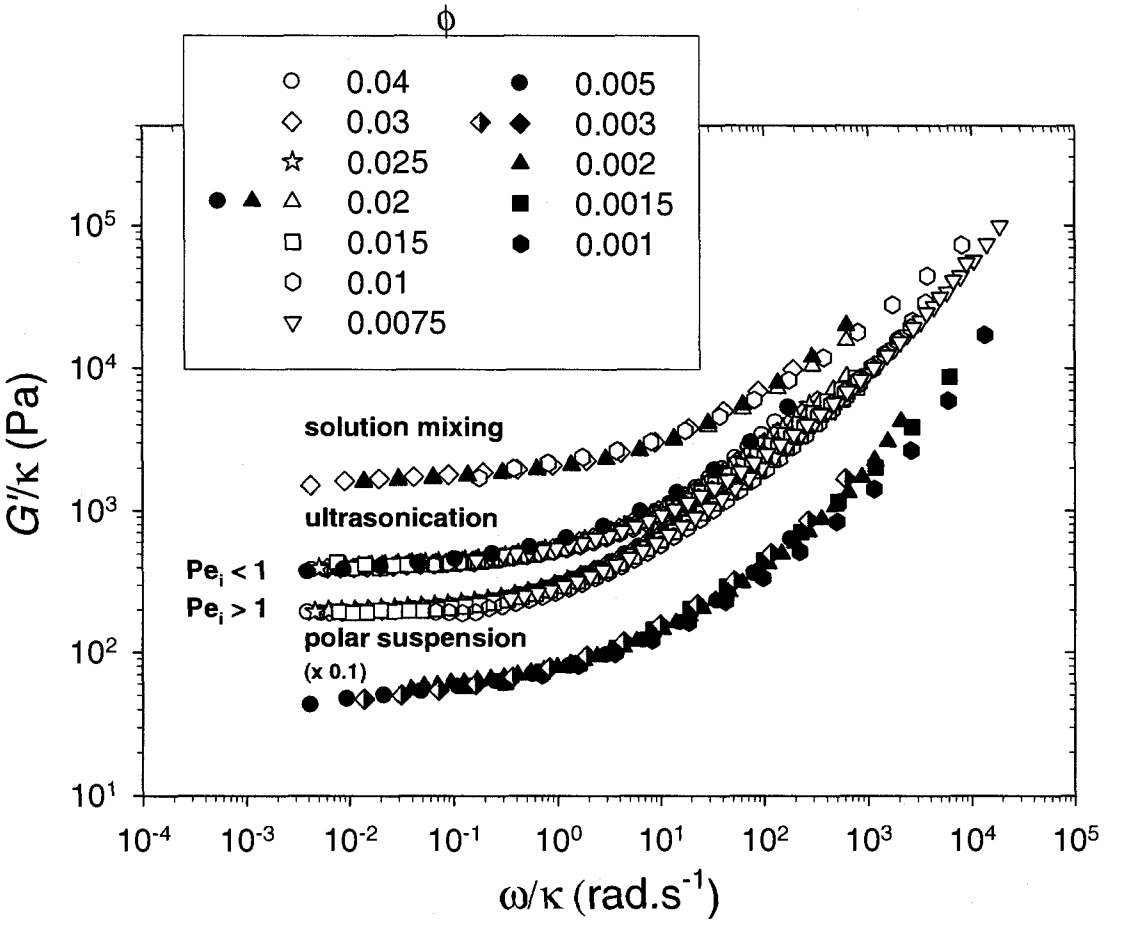

Figure 5.5 : Scaling behavior of G' as a function of scaled frequency ω/κ as ϕ is varied for the polar suspension (ϕ_{ref} = 0.003) and the two non-polar suspensions prepared by solution mixing and ultrasonication (ϕ_{ref} = 0.02). Fluorescent suspensions (with Safranine-O) are indicated with the following symbols: [●] non-polar suspension prepared by ultrasonication with ϕ= 0.02; [▲] non-polar suspension prepared by solution mixing for ϕ = 0.02; [◆] polar suspension for ϕ = 0.003.

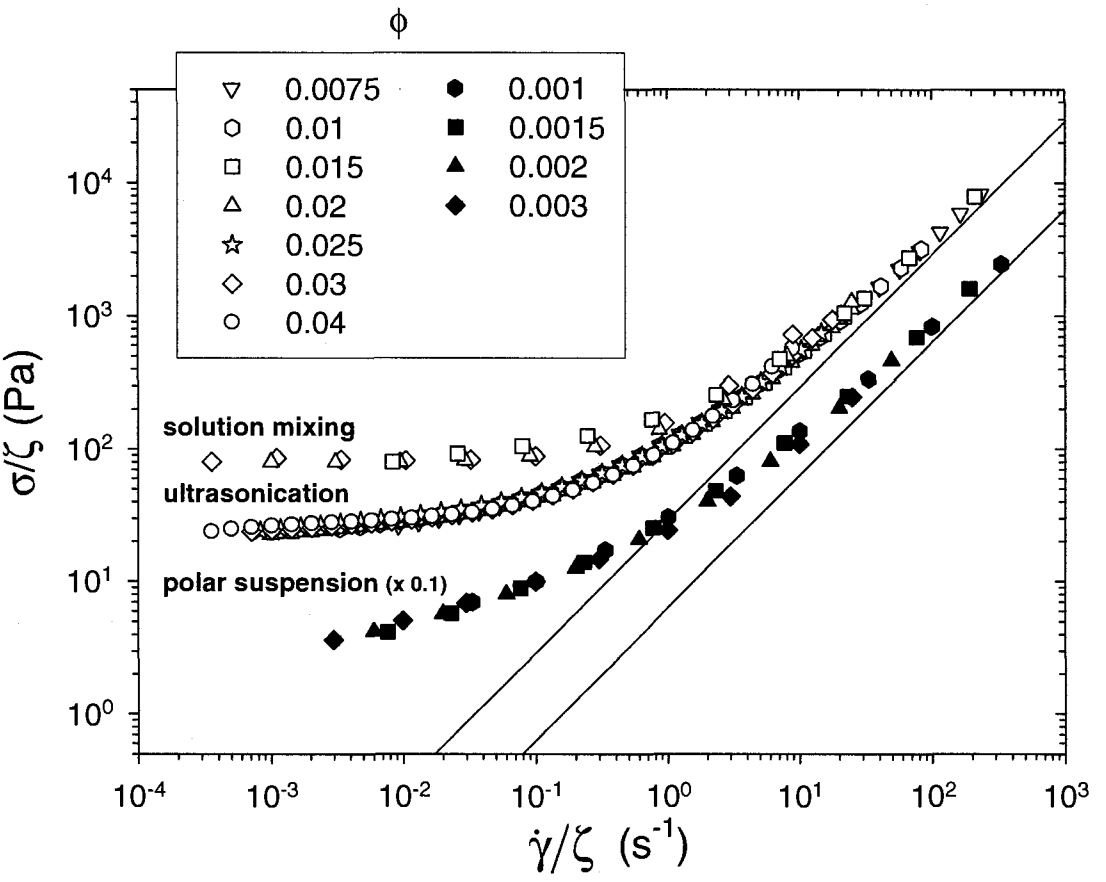

Figure 5.6 : Scaling behavior of σ as a function of scaled shear rate $\dot{\gamma}/\zeta$ as ϕ is varied for the polar suspension (ϕ_{ref} = 0.003; filled symbols) and the two non-polar suspensions (unfilled symbols) prepared by solution mixing and ultrasonication (ϕ_{ref} = 0.02). The solid lines represent the shear stress of the suspending fluids.

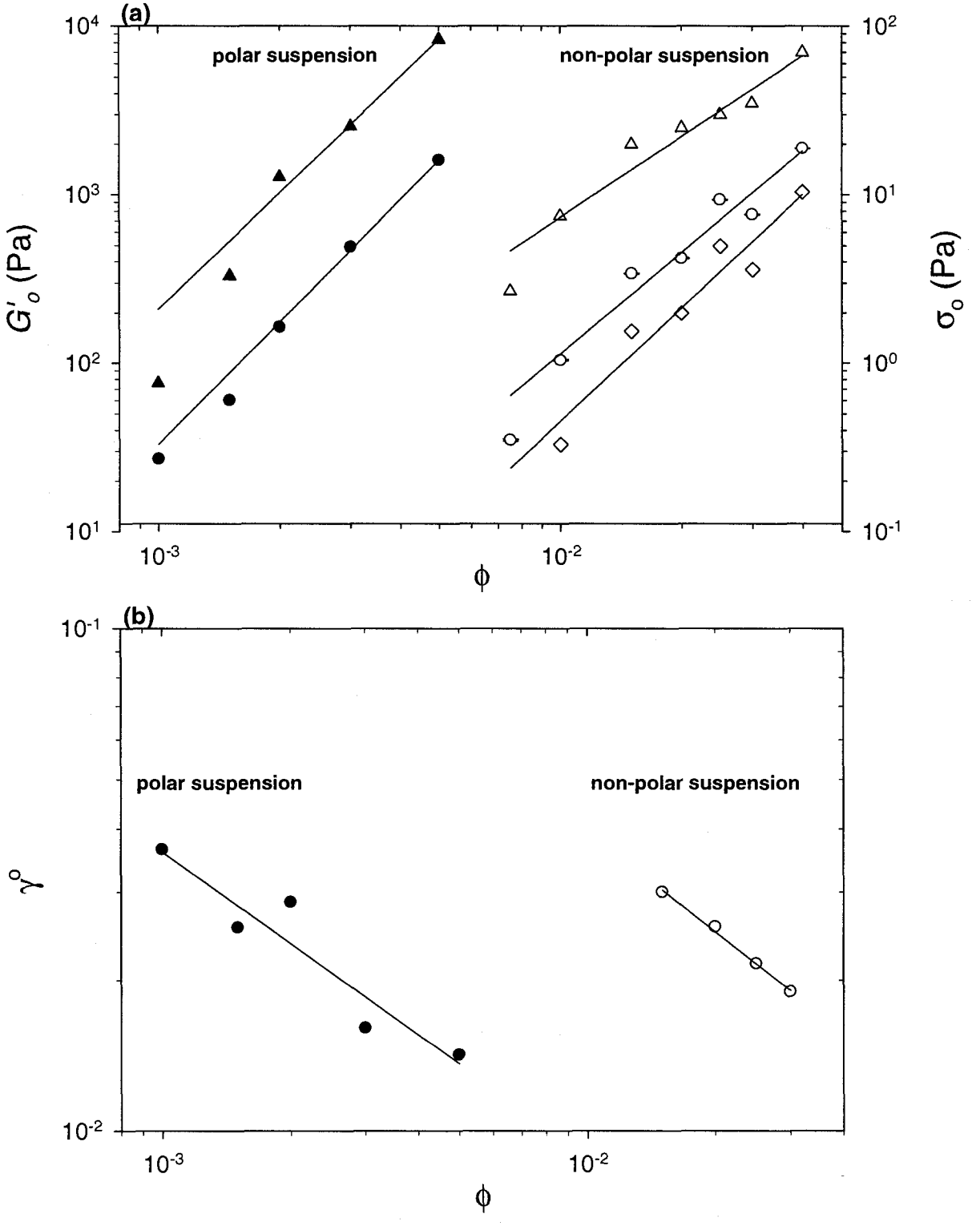
(a)
polar suspension
non-polar suspension
G'_o (Pa)
σ_o (Pa)
10^4
10^3
10^2
10^1
10^2
10^1
10^0
10^{-1}
10^{-3}
10^{-2}
ϕ
(b)
polar suspension
non-polar suspension
γ^o
10^{-1}
10^{-2}
10^{-3}
10^{-2}
ϕ

Figure 5.7 : Volume fraction dependence of G'_0 (circle: $Pe_i < 1$ and diamond: $Pe_i > 1$) and σ_0 (triangle) (a) and of γ^0 (b) for the non-polar suspension prepared by ultrasonication (unfilled symbols) and the polar dispersion (filled symbols).

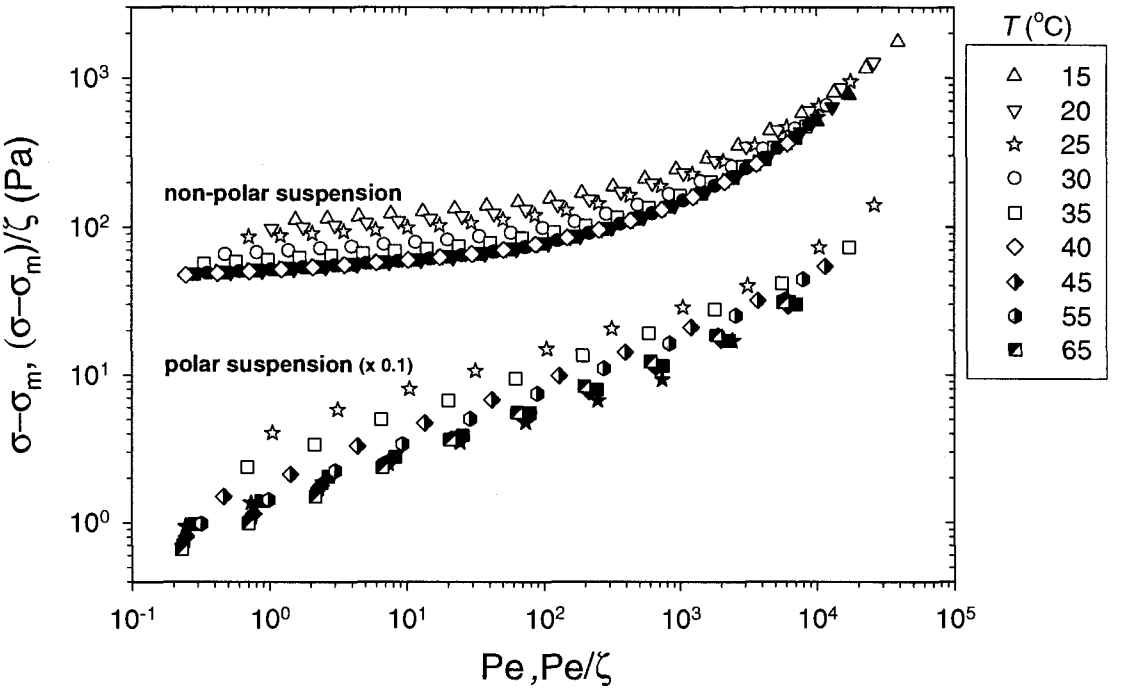

Figure 5.8 : Temperature dependency of σ-σ_m (unfilled and semi-filled symbols) and its scaling behavior (filled symbols) for the non-polar suspension prepared by ultrasonication ($\phi = 0.04$) and the polar suspension ($\phi = 0.003$).

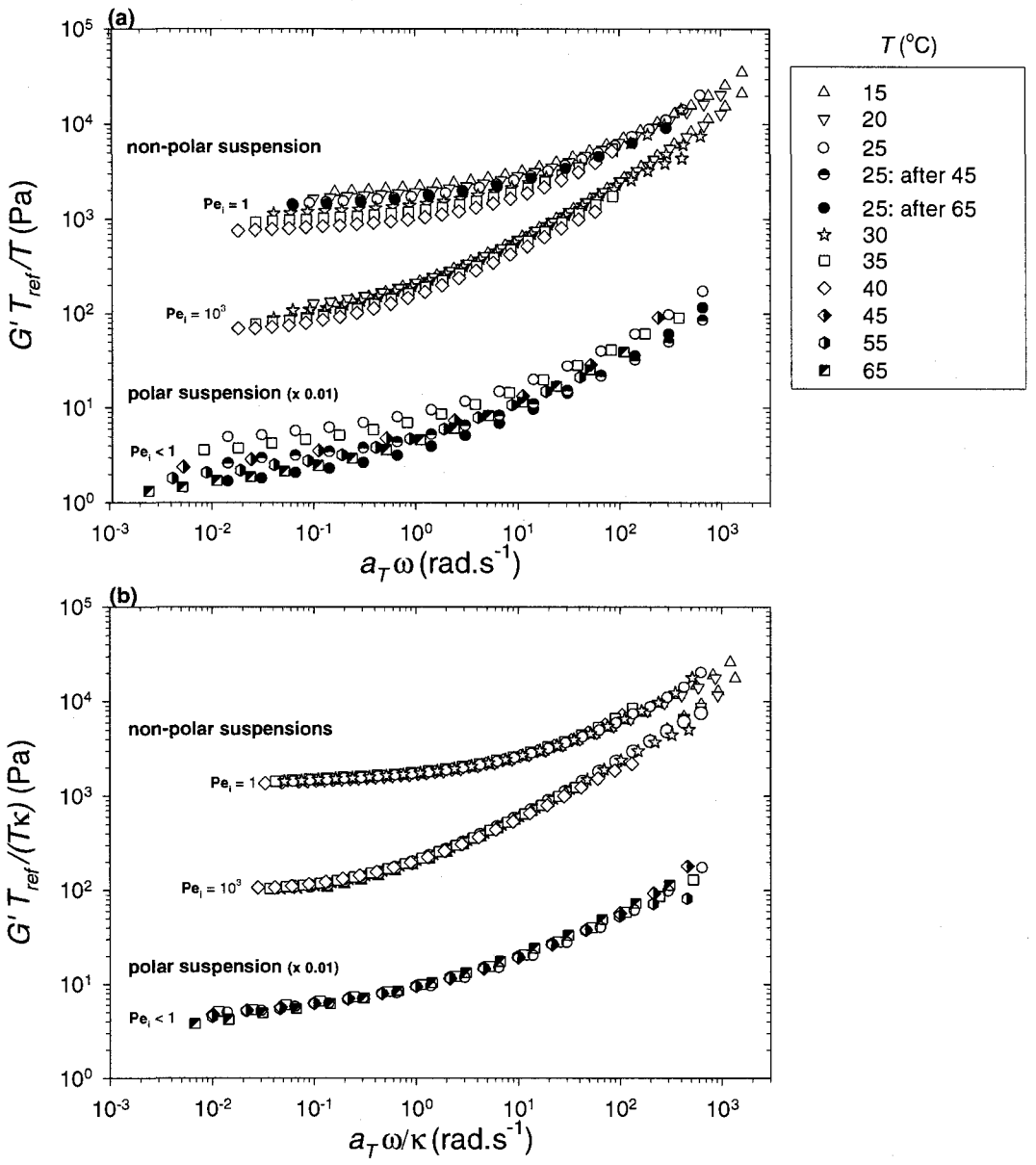

Figure 5.9 : Temperature dependency of G' (a) and its scaling behavior (b) for the non-polar suspension prepared by ultrasonication ($\phi = 0.04$) and the polar suspension ($\phi = 0.003$).

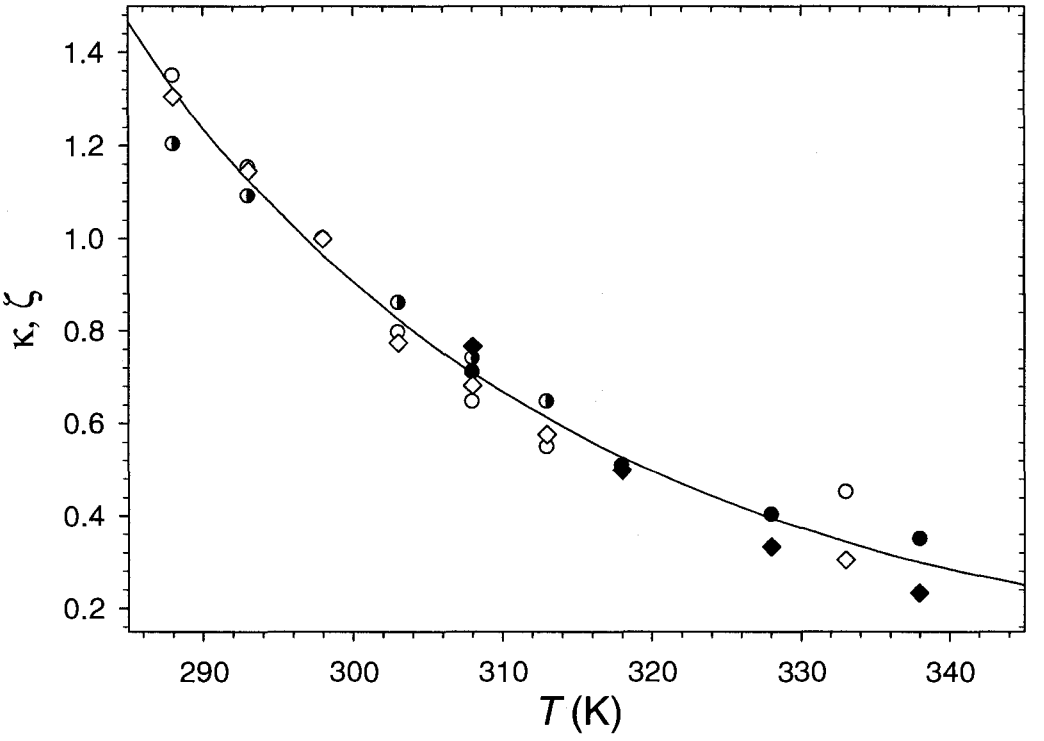

Figure 5.10 : Temperature dependency of the shift factors κ (circles) and ζ (diamonds) for the non-polar suspension prepared by ultrasonication (Pe = 1: unfilled symbols; Pe = 1000: semi filled symbols - $\phi = 0.04$) and the polar suspension (filled symbols - $\phi = 0.003$).

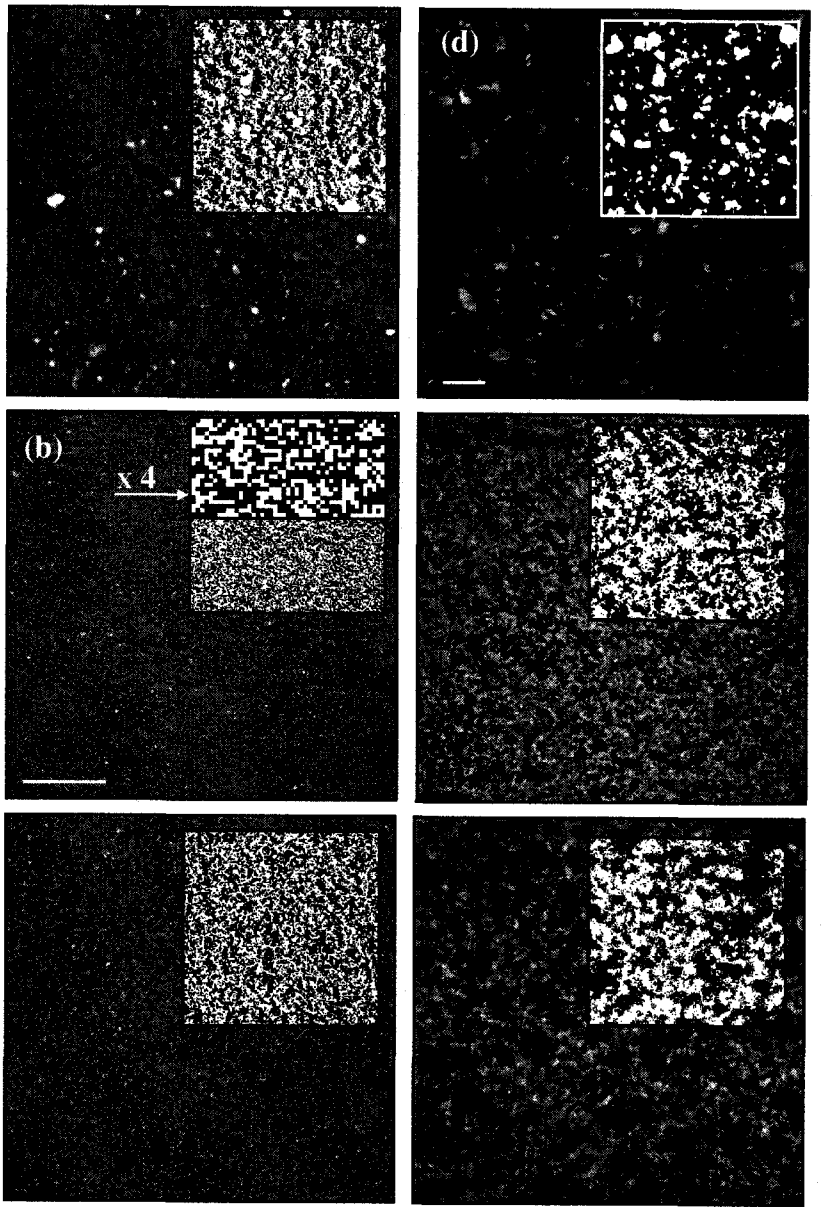
(d)
(b)
x 4

Figure 5.11 : Confocal scanning laser microscopy images of the quiescent microstructures of the layered silicate suspensions. Non-polar suspensions prepared by ultrasonication (a) 2 vol. %, by solution mixing (b) 2 vol. %, (c) 1 vol. %, (d) 2 vol. % (Cloisite 30B), and polar suspension prepared by solution mixing (e) 0.3 vol. %, (f) 0.15 vol. %. White areas are rich in layered silicate. The scale bars represent 50 μm. The insets show the corresponding image part after binarization. The images were taken at room temperature (about 23 ^{o}C).

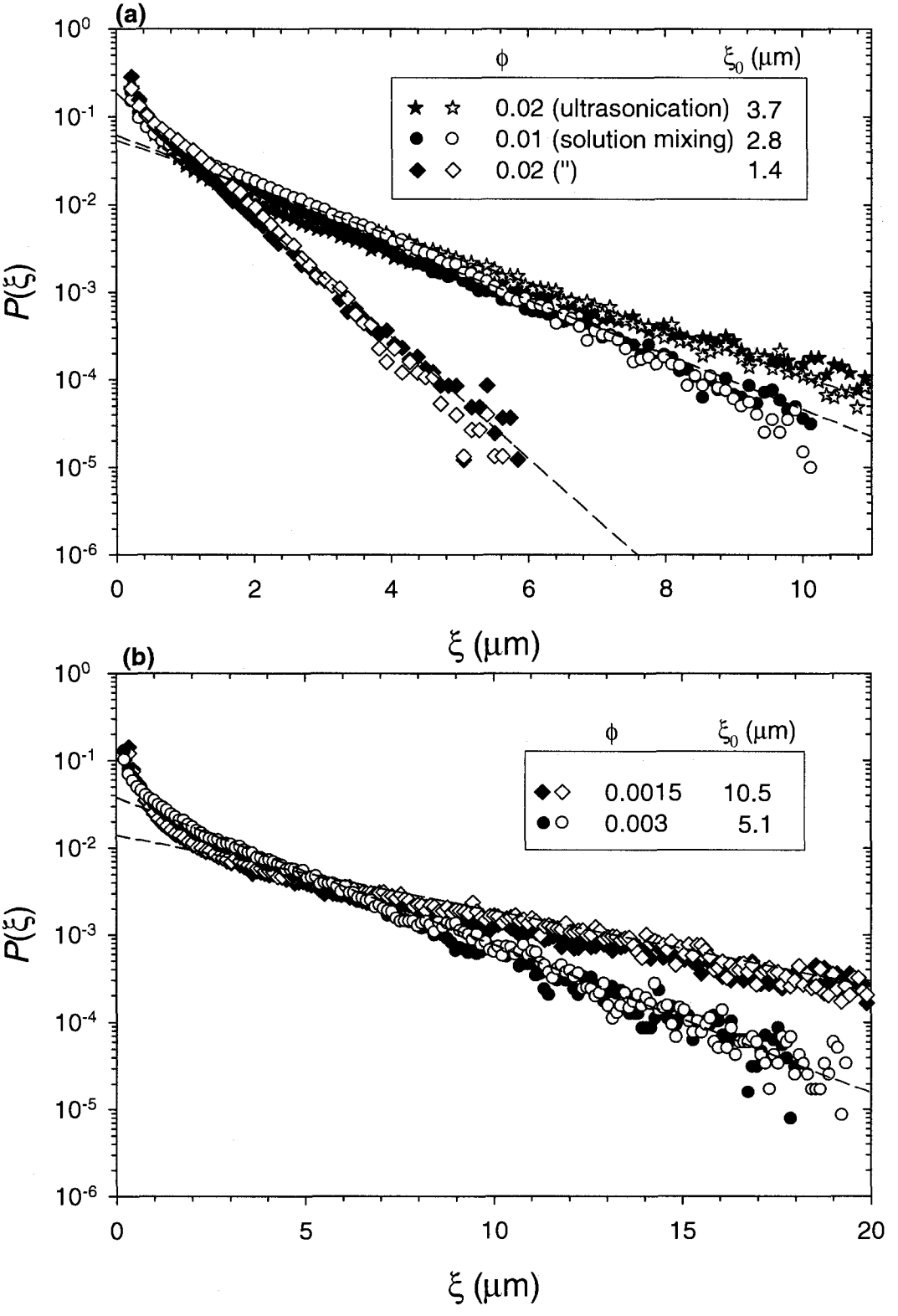
(a)
ϕ
ξ0 (μm)
0.02 (ultrasonication) 3.7
0.01 (solution mixing) 2.8
0.02 (") 1.4
P(ξ)
ξ (μm)
(b)
ϕ
ξ0 (μm)
0.0015 10.5
0.003 5.1
P(ξ)
ξ (μm)

Figure 5.12 : ξ distributions along *x*- (unfilled symbols) and *y*- (filled symbols) directions for the non-polar suspensions (a) and polar suspensions (b). The dashed lines represent log-linear regressions.

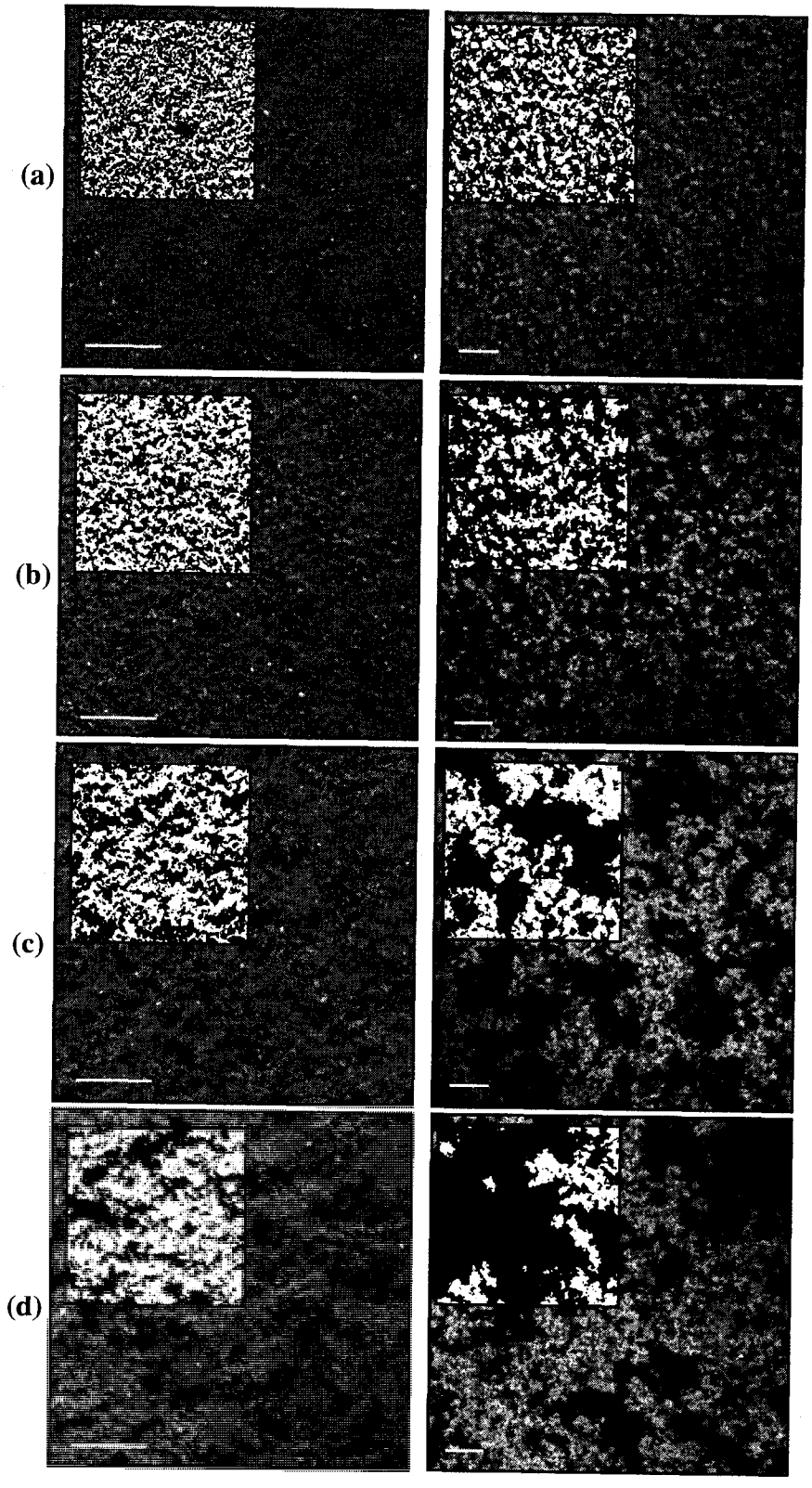
(a)
(b)
(c)
(d)

Figure 5.13 : Effect of the pre-shearing amplitude on the flow-induced metastable microstructures of the layered silicate suspensions. Non-polar (right, 2 vol. %) and polar (left, 0.3 vol. %) suspensions prepared by solution mixing (a) 10 s^{-1}, (b) 1 s^{-1}, (c) 0.1 s^{-1}, (d) 0.01 s^{-1}. The scale bars represent 25 μm. The pre-shearing direction is from bottom to top. The insets show the corresponding image part after binarization. The images were taken at room temperature (about 23 °C).

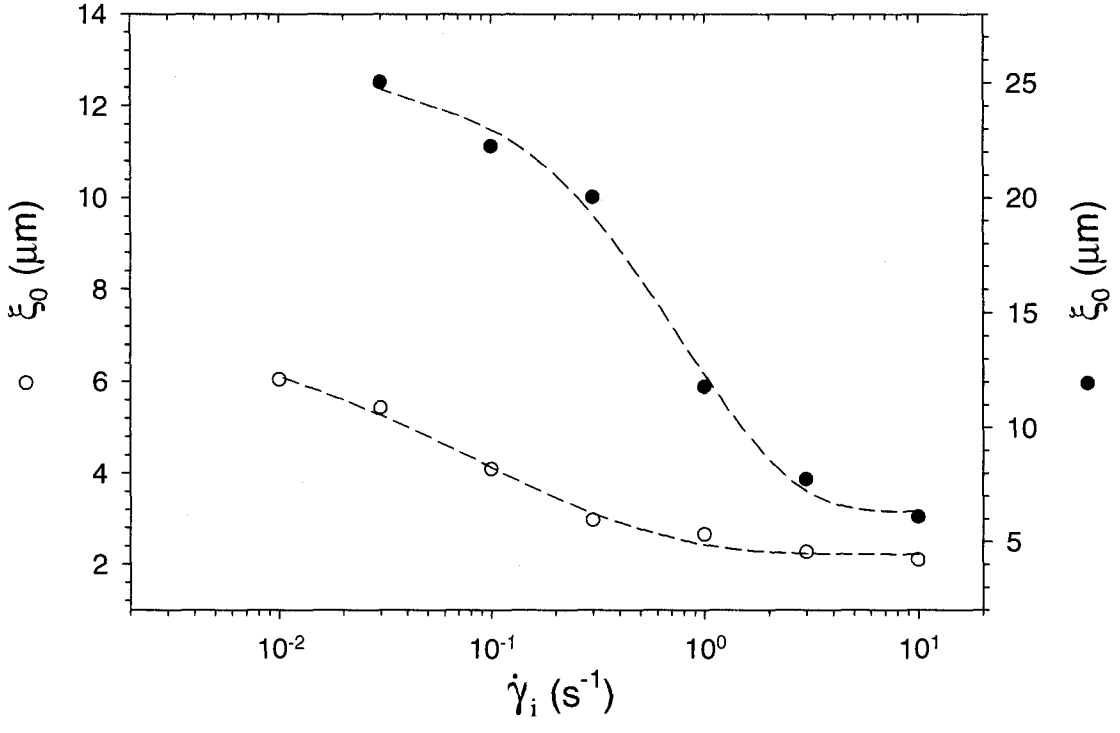

Figure 5.14 : Dependence of the characteristic length scale ξ_0 with the pre-shearing amplitude $\dot{\gamma}_i$ of the non-polar (unfilled symbols) and polar suspension (filled symbols) metastable structures. The dashed lines are drawn to guide the eyes

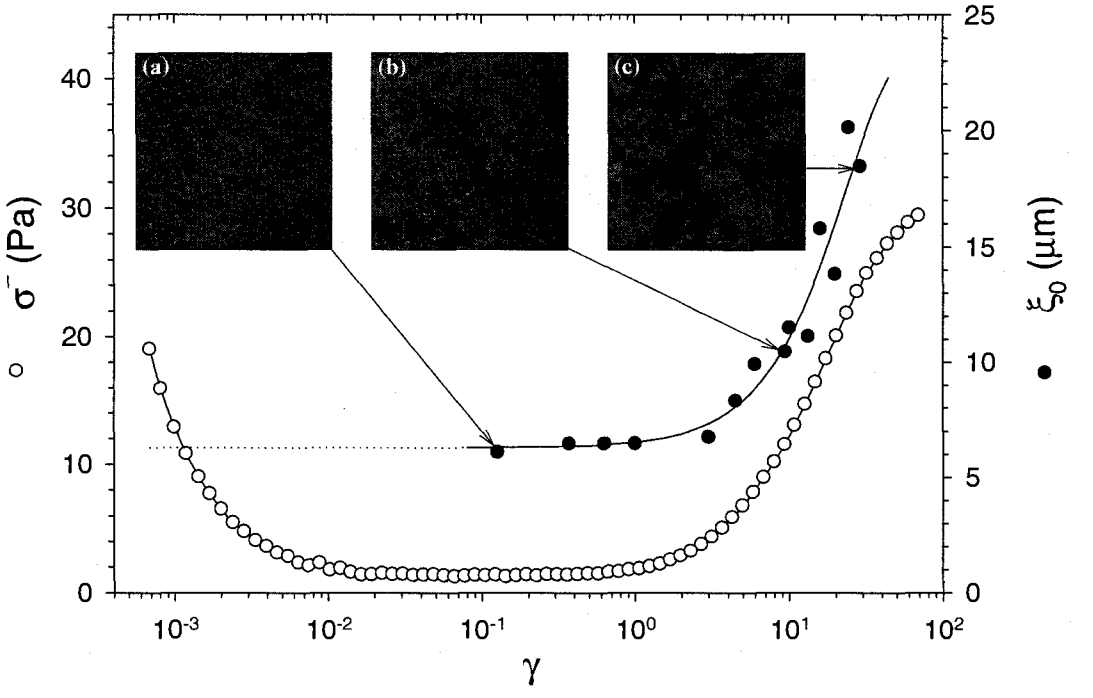

Figure 5.15 : σ^- (unfilled symbols) and ξ_0 (filled symbols) as a function of γ after a stepwise reduction in shear rate from 10 to 10^{-2} s^{-1} for the polar suspension ($\phi = 0.003$). The insets show CLSM images at different deformations: (a) 0.13, (b) 10 and (c) 29. The solid line is drawn to guide the eyes.

Table 5.1 : Values of the scaling exponents n, B, β, and t and fractal dimensions D_f of non- and polar suspensions; [a] non-polar suspension prepared by ultrasonication, [b] D_f derived from Equation 7.

Sample		n	B	D_f	β	t (D_f[b])
non-polar suspension[a]	$Pe_i < 1$	2.2	-0.7	1.7	2.8	1.7 (1.8)
	$Pe_i > 1$	2.6	-	-	-	-
polar suspension	$Pe_i < 1$	2.6	-0.6	2	2.6	2.3 (2.1)

[a] non-polar suspension prepared by ultrasonication.

[b] D_f derived from Equation 5.7.

CHAPITRE 6 - DISCUSSION GÉNÉRALE ET CONCLUSION

Les nombreuses études publiées sur le comportement rhéologique des nanocomposites polymère/phyllosilicate interprètent leur comportement rhéofluidifiant et thixotrope sous la seule perspective de l'évolution d'orientation de leurs feuillets ou d'empilements de feuillets tandis que la percolation de ces derniers est évoquée pour expliquer leur comportement pseudo-solide. La contribution majeure de cette thèse est de considérer non seulement l'évolution de la distribution d'orientation mais également l'évolution de la distribution spatiale des feuillets lors de l'analyse de leur comportement rhéologique, et d'appuyer leur description par des techniques de mesures inédites.

La première contribution originale a été de mettre en évidence l'influence de l'histoire d'écoulement sur les propriétés viscoélastiques linéaires et non linéaires de suspensions polaires et non-polaires de phyllosilicate. La conséquence la plus frappante au niveau de leurs propriétés viscoélastiques linéaires est leur transition d'un comportement pseudo-liquide à un comportement pseudo-solide avec la diminution de l'amplitude du pré-cisaillement. Elle témoigne de l'existence de structures métastables dont la compréhension de leur origine et la description de leur nature ont motivé la suite de ce travail.

La nature microscopique et les propriétés auto-similaires des structures métastables ont été déduites de l'analyse fractale de leurs propriétés viscoélastiques linéaires et du

profil d'intensité de leurs clichés de diffusion de lumière en deux dimensions. La microscopie confocale à balayage laser a permis d'observer directement les microstructures métastables et de confirmer leur nature fractale par la mesure de leur distance caractéristique à différentes fractions volumiques. Le comportement pseudo-solide de ces suspensions est donc attribué à la présence d'un réseau d'agrégats de feuillets de nature fractale en masse.

Sous écoulement, des mesures de dichroïsme ont permis de suivre l'anisotropie développée dans les plans de vorticité et du gradient de cisaillement. Dans le plan de vorticité, la structure s'oriente progressivement selon la direction d'écoulement avec l'augmentation de la vitesse de cisaillement. Une fois le plateau de viscosité atteint, l'évolution de la distribution spatiale des agrégats s'accompagne d'une augmentation de l'anisotropie dans le plan du gradient de cisaillement. Suite à un pré-cisaillement, l'absence de relaxation de l'anisotropie induite par écoulement est explicitement montrée avec des mesures de 2D-SAOS. Les microstructures métastables ont par conséquent la même nature anisotrope que leur contrepartie sous écoulement. Toutefois, l'anisotropie reste faible comme le suggère les clichés de diffusion de lumière, et comme l'attestent les observations directes par microscopie confocale à balayage laser. Les structures métastables diffèrent en fait principalement par leur distance caractéristique. Elle diminue avec la vitesse de cisaillement d'une haute à une faible valeur au plateau. L'évolution structurelle est attribuée à une agrégation réversible induite par écoulement. Suite à un pré-cisaillement, aucune relaxation

structurelle à l'échelle microscopique n'a été observée en microscopie confocale à balayage laser. Le comportement thixotrope de ces suspensions implique alors des réarrangements à l'échelle nanoscopique. Les microstructures sous écoulement ont donc la même distance caractéristique que leur microstructure métastable subséquente. Le comportement rhéofluidifiant de ces suspensions découle ainsi de l'évolution de la distribution spatiale des feuillets. A la connaissance de l'ensemble de ces résultats, l'influence de l'histoire d'écoulement est expliquée par la persistance des distances caractéristiques contrôlées par la vitesse de cisaillement.

Bien que les tendances affichées par les propriétés viscoélastiques linéaires et non linéaires de ces suspensions aient été généralisées en étudiant le comportement d'échelle avec la température, la fraction volumique, et l'histoire d'écoulement, elles ne représentent qu'une description partielle de ces systèmes limitée au cas d'un potentiel d'attraction fort entre les feuillets. À l'image des travaux de Trappe *et al.* (2001), leur connaissance approfondie nécessiterait d'établir leur diagramme de phase (liquide/solide) en fonction de la contrainte, de la fraction volumique, et du potentiel d'attraction entre les feuillets. Une description multi-échelle des phases accompagnée de leur caractérisation rhéologique permettrait de réellement évaluer le potentiel de la rhéologie comme technique d'étude de l'état de dispersion des suspensions non-aqueuses de phyllosilicate.

CHAPITRE 7 - PERSPECTIVES

Les travaux présentés mériteraient d'être étendus dans la perspective du diagramme de phase de Trappe *et al.* (2001), et tout particulièrement pour différentes amplitudes du potentiel d'attraction entre les feuillets. Une diminution du potentiel d'attraction des particules colloïdales en suspension dans un solvant organique est le plus souvent observée avec la température. Il serait alors intéressant d'étendre l'étude en température de la suspension non-polaire à de plus hautes températures voisines de celles rencontrées lors de la mise en forme des nanocomposites à base de thermoplastique. Pour le système polaire, l'amplitude du potentiel d'interaction pourrait être variée en jouant notamment sur le poids moléculaire du polyalkyléene glycol adsorbé à sa surface. Une caractérisation précise des propriétés physiques des composants des suspensions (indice de réfraction, constante diélectrique, paramètres de solubilité, poids moléculaire, etc.) permettrait une approche plus rationnelle du potentiel d'interaction. Il serait également profitable d'étendre la mesure de leurs propriétés viscoélastiques linéaires à de plus faibles fréquence selon les méthodes de Wyss *et al.* (2007) et de Helgeson *et al.* (2006).

La caractérisation de l'état de dispersion à l'échelle du nanomètre par diffraction des rayons X permettrait d'identifier les réarrangements responsables du comportement thixotrope des suspensions. De plus, elle renseignerait sur les mécanismes de rupture observée à de faibles déformations lors des démarrages à vitesse imposée.

RÉFÉRENCES

Aubry, T., T. Razafinimaro, and P. Mederic, "Rheological investigation of the melt state elastic and yield properties of a polyamide-12 layered silicate nanocomposite," *J. Rheol.* 49, 425-440 (2005).

Ayyer, R. K., and A. I. Leonov, "Comparative rheological studies of polyamide-6 and its low loaded nanocomposite based on layered silicates," *Rheol. Acta* 43, 283-292 (2004).

Bafna, A., G. Beaucage, F. Mirabella, and S. Mehta, "3D hierarchical orientation in polymer-clay nanocomposite films," *Polymer* 44, 1103-1115 (2003).

Balazs, A. C., C. Singh, and E. Zhulina, "Modeling the interactions between polymers and clay surfaces through self-consistent field theory," *Macromolecules* 31, 8370-8381 (1998).

Balazs, A. C., C. Singh, E. Zhulina, and Y. Lyatskaya, "Modeling the phase behavior of polymer/clay nanocomposites," *Am. chem. soc.* 32, 651-657 (1999).

Barnes, H. A., "Thixotropy - a review," *J. Non-Newtonian Fluid Mech.* 70, 1-33 (1997).

Batchelor, P., G. H. Meeten, and G. C. Maitland, "Linear birefringence and dichroism measurements on polytetrafluorethylene dispersions," *J. Colloid and Interface Sci.* 117, 360-365 (1987).

Bihannic, I., L. J. Michot, B. S. Lartiges, D. Vantelon, J. Labille, F. Thomas, J. Susini, M. Salome, and B. Fayard, "First direct visualization of oriented mesostructures in clay gels by synchrotron-based X-ray fluorescence microscopy," *Langmuir* 17, 4144-4147 (2001).

Bousmina, M., "Study of Intercalation and Exfoliation Processes in Polymer Nanocomposites," *Macromolecules* 39, 4259-4263 (2006).

Bremer, L. G. B., B. H. Bijsterbosch, P. Walstra, and T. Vanvliet, "Formation, Properties and Fractal Structure of Particle Gels," *Adv. Colloid Interface Sci.* 46, 117-128 (1993).

Bremer, L. G. B., T. Vanvliet, and P. Walstra, "Theoretical and Experimental-Study of the Fractal Nature of the Structure of Casein Gels," *J. Chem. Soc. - Faraday Trans.* I 85, 3359-3372 (1989).

Buscall, R., P. D. A. Mills, J. W. Goodwin, and D. W. Lawson, "Scaling Behavior of the Rheology of Aggregate Networks Formed from Colloidal Particles," *J. Chem. Soc. Faraday Trans.* 84, 4249-4260 (1988).

Bushell, G. C., Y. D. Yan, D. Woodfield, J. Raper, and R. Amal, "On techniques for the measurement of the mass fractal dimension of aggregates," *Adv. Colloid Interface Sci.* 95, 1-50 (2002).

Cadene, A., S. Durand-Vidal, P. Turq, and J. Brendle, "Study of individual Na-montmorillonite particles size, morphology, and apparent charge," *J. Colloid and Interface Sci.* 285, 719-730 (2005).

Crassous, J. J., R. Regisser, M. Ballauff, and N. Willenbacher, "Characterization of the viscoelastic behavior of complex fluids using the piezoelastic axial vibrator," *J. Rheol.* 49, 851-863 (2005).

Crompton, K. E., R. J. Prankerd, D. M. Paganin, T. F. Scott, M. K. Horne, D. I. Finkelstein, K. A. Gross, and J. S. Forsythe, "Morphology and gelation of thermosensitive chitosan hydrogels," *Biophys. Chem.* 117, 47-53 (2005).

Cumming, A., P. Wiltzius, F. S. Bates, and J. H. Rosedale, "Light-scattering experiments on phase-separation dynamics in binary fluid mixtures," *Phys. Rev. A* 45, 885-897 (1992).

D'Haene, P., J. Mewis, and G. G. Fuller, "Scattering Dichroism Measurements of Flow-Induced Structure of a Shear Thickening Suspension," *J. Colloid and Interface Sci.* 156, 350-358 (1993).

De Cleyn, G., and J. Mewis, "Constitutive equation for polymer liquids: application to shear flow," *J. Non-Newtonian Fluid Mech.* 9, 91-105 (1987).

Degroot, J. V., C. W. Macosko, T. Kume, and T. Hashimoto, "Flow-Induced Anisotropic Sals in Silica-Filled Pdms Liquids," *J. Colloid and Interface Sci.* 166, 404-413 (1994).

Dhont, J. K. G., and N. J. Wagner, "Superposition rheology," *Phys. Rev. E* 63, 021406 (2001).

Di, Y., S. Iannace, E. Di Maio, and L. Nicolais, "Nanocomposites by melt intercalation based on polycaprolactone and organoclay," *J. of Polym. Sci., Part B: Polymer Physics* 41, 670-678 (2003).

Dullaert, K., and J. Mewis, "A model system for thixotropy studies," *Rheol. Acta* 45, 23-32 (2005a).

Dullaert, K., and J. Mewis, "Stress jumps on weakly flocculated dispersions: Steady state and transient results," *J. Colloid and Interface Sci.* 287, 542-551 (2005b).

Durmus, A., A. Kasgoz, and C. W. Macosko, "Linear low density polyethylene (LLDPE)/clay nanocomposites. Part I: Structural characterization and quantifying clay dispersion by melt rheology," *Polymer* 48, 4492-4502 (2007).

Eslami, H., M. Grmela, and M. Bousmina, "A mesoscopic rheological model of polymer/layered silicate nanocomposites," *J. of Rheol.* 51, 1189-1222 (2007).

Firoozmand, H., B. S. Murray, and E. Dickinson, "Fractal-Type Particle Gel Formed from Gelatin + Starch Solution," *Langmuir* 23, 4646-4650 (2007).

Flory, P. J., *Principles of Polymer Chemistry* (Cornell University Press,Ithaca et London, 1953).

Fornes, T. D., P. J. Yoon, D. L. Hunter, H. Keskkula, and D. R. Paul, "Effect of organoclay structure on nylon 6 nanocomposite morphology and properties," *Polymer* 43, 5915-5933 (2002).

Frattini, P. L., and G. G. Fuller, "Dynamic of dilute colloidal suspensions subject to time-dependent flow fields by conservative dichroism," *J. Colloid and Interface Sci.* 100, 506-518 (1984).

Fuller, G. G., *Optical rheometry of complex fluids* (Oxford university press,New York, 1995).

Galgali, G., S. Agarwal, and A. Lele, "Effect of clay orientation on the tensile modulus of polypropylene-nanoclay composites," *Polymer* 45, 6059-6069 (2004).

Galgali, G., C. Ramesh, and A. Lele, "Rheological study on the kinetics of hybrid formation in polypropylene nanocomposites," *Macromolecules* 34, 852-858 (2001).

Gefen, Y., A. Aharony, B. B. Mandelbrot, and S. Kirkpatrick, "Solvable Fractal Family, and Its Possible Relation to the Backbone at Percolation," *Phys. Rev. Lett.* 47, 1771-1774 (1981).

Gendelman, O. V., L. I. Manevitch, and O. L. Manevitch, "Solitonic mechanism of structural transition in polymer-clay nanocomposites," *J. Chem. Phys.* 119, 1066-1069 (2003).

Ginzburg, V. V., and A. C. Balazs, "Calculating phase diagrams of polymer-platelet mixtures using density functional theory: implications for polymer/clay composites," *Macromolecules* 32, 5681-5688 (1999).

Ginzburg, V. V., and A. C. Balazs, "Calculating phase diagrams for nanocomposites: the effect of adding end-functionalized chains to polymer/clay mixtures," *Adv. Mat.* 12, 1805-1809 (2000).

Ginzburg, V. V., O. V. Gendelman, and L. I. Manevitch, "Simple "kink" model of melt intercalation in polymer-clay nanocomposites," *Phys. Rev. Lett.* 86, 5073-5075 (2001).

Ginzburg, V. V., C. Singh, and A. C. Balazs, "Theoretical phase diagrams of polymer/clay composites: the role of grafted organic modifiers," *Macromolecules* 33, 1089-1099 (2000).

Götze, W., *Aspects of structural glass transitions* (Elsevier, Les Houches, 1991).

Grim, R. E., *Clay mineralogy*. McGraw-Hill Book Company: New York, St. Louis, San Francisco, Toronto, London, Sydney, 1968; p 596.

Gupta, V. K., R. Krishnamoorti, Z.-R. Chen, J. A. Kornfield, S. D. Smith, M. M. Satkowski, and J. T. Grothaus, "Dynamics of shear alignment in a lamellar diblock copolymer: interplay of frequency, strain amplitude, and temperature," *Macromolecules* 29, 875 (1996).

Hanley, H. J. M., C. D. Muzny, D. L. Ho, and C. J. Glinka, "A small-angle neutron scattering study of a commercial organoclay dispersion," *Langmuir* 19, 5575-5580 (2003).

Helgeson, M. E., N. J. Wagner, and D. Vlassopoulos, "Viscoelasticity and shear melting of colloidal star polymer glasses," *J. Rheol.* 51, 297-316 (2007a).

Helgeson, M. E., N. J. Wagner, and D. Vlassopoulos, "Viscoelasticity and shear melting of colloidal star polymer glasses," *J. Rheol.* 51, 297-316 (2007b).

Hirokawa, Y., H. Jinnai, Y. Nishikawa, T. Okamoto, and T. Hashimoto, "Direct Observation of Internal Structures in Poly(N-isopropylacrylamide) Chemical Gels," *Macromolecules* 32, 7093-7099 (1999).

Ho, D. L., R. M. Briber, and C. J. Glinka, "Characterization of organically modified clays using scattering and microscopy techniques," *Chem. Mater.* 13, 1923-1931 (2001).

Ho, D. L., R. M. Briber, and C. J. Glinka, *Studies of organically modified clays by scattering techniques* (Oxford University Press, San Francisco, 2002).

Ho, D. L., and C. J. Glinka, "Effects of solvent solubility parameters on organoclay dispersions," *Chem. Mater.* 15, 1309-1312 (2003).

Hobbie, E. K., and D. J. Fry, "Rheology of concentrated carbon nanotube suspensions," *J. Chem. Phys.* 126, 124907 (2007).

Hobbie, E. K., H. S. Jeon, H. Wang, H. Kim, D. J. Stout, and C. C. Han, "Shear-induced structure in polymer blends with viscoelastic asymmetry," *J. Chem. Phys.* 117, 6350-6359 (2002).

Hobbie, E. K., S. Lin-Gibson, H. Wang, J. A. Pathak, and H. Kim, "Ubiquity of domain patterns in sheared viscoelastic fluids," *Phys. Rev. E* 69, (2004).

Hoekstra, H., J. Mewis, T. Narayanan, and J. Vermant, "Multi length scale analysis of the microstructure in sticky sphere dispersions during shear flow," *Langmuir* 21, 11017-11025 (2005).

Hoekstra, H., J. Vermant, and J. Mewis, "Flow-induced anisotropy and reversible aggregation in two-dimensional suspensions," *Langmuir* 19, 9134-9141 (2003).

Hoffmann, B., C. Dietrich, R. Thomann, C. Friedrich, and R. Mülhaupt, "Morphology and rheology of polystyrene nanocomposites based upon organoclay," *Macromol. Rapid Commun.* 21, 57-61 (2000a).

Hoffmann, B., J. Kressler, G. Stöppelmann, C. Friedrich, and G.-M. Kim, "Rheology of nanocomposites based on layered silicates and polyamide-12," *Colloid Polym. Sci.* 278, 0629 - 0636 (2000b).

Hsieh, A. J., P. Moy, F. L. Beyer, P. Madison, E. Napadensky, J. Ren, and R. Krishnamoorti, "Mechanical response and rheological properties of polycarbonate layered-silicate nanocomposites," *Polym. Eng. Sci.* 44, 825-837 (2004).

Hyun, K., S. H. Kim, K. H. Ahn, and S. J. Lee, "Large amplitude oscillatory shear as a way to classify the complex fluids," *J. Non-Newtonian Fluid Mech.* 107, 51-65 (2002).

Isichenko, M. B., "Percolation, statistical topography, and transport in random media," *Rev. Modern phys.* 64, 961-1043 (1992).

Jin, L., and P. O. James, "The effect of free surfactant and grafted surfactant surface coverage on the rheology of organoclay dispersions," *J. Rheol.* 50, 729-747 (2006).

Jogun, S., and C. F. Zukoski, "Rheology of dense suspensions of platelike particles," *J. Rheol.* 40, 1211-1232 (1996).

Jogun, S. M., and C. F. Zukoski, "Rheology and microstructure of dense suspensions of plate-shaped colloidal particles," *J. Rheol.* 43, 847-871 (1999).

Johnson, S. J., P. L. Frattini, and G. G. Fuller, "Simultaneous dichroism and birefringence measurements of dilute colloidal suspensions in transient shear flow," *J. Colloid and Interface Sci.* 104, 440-455 (1985).

Johnson, S. J., and G. G. Fuller, "Optical anisotropy of sheared hematite suspensions," *J. Colloid and Interface Sci.* 124, 441-451 (1988).

Johnson, S. J., A. J. Salem, and G. G. Fuller, "Dynamics of colloidal particles in sheared, non-Newtonian fluids," *J. Non-Newtonian Fluid Mech.* 34, 89-121 (1990).

Jones, T. R., "The properties and uses of clays which swell in organic solvents," *Clay Minerals* 18, 399-410 (1983).

Kantor, Y., and I. Webman, "Elastic properties of random percolating systems," *Phys. Rev. Lett.* 52, 1891-1894 (1984).

Kaufman, L. J., C. P. Brangwynne, K. E. Kasza, E. Filippidi, V. D. Gordon, T. S. Deisboeck, and D. A. Weitz, "Glioma Expansion in Collagen I Matrices: Analyzing Collagen Concentration-Dependent Growth and Motility Patterns," *Biophys. J.* 89, 635-650 (2005).

Khan, S. A., and N. J. Zoeller, "Dynamic rheological behavior of flocculated fumed silica suspensions," *J. Rheol.* 37, 1225-1235 (1993).

Kim, J. L., D. H. Kim, K. S. Cho, K. H. Ahn, and S. J. Lee, *Rheological behavior of polypropylene/clay nanocomposites under uniaxial extensional flow* (Seoul, Korea, 2004).

King, H. E., S. T. Milner, M. Y. Lin, J. P. Singh, and T. G. Mason, "Structure and rheology of organoclay suspensions," *Phys. Rev. E* 75, 21403 (2007).

Kitano, T., T. Kataoka, and Y. Nagatsuka, "Shear flow rheological properties of vinylon-and glass fiber reinforced polyethylene melts," *Rheol. Acta* 23, 20-30 (1984).

Kojima, Y., A. Usuki, M. Kawasumi, A. Okada, T. Kurauchi, and O. Kamigaito, "Synthesis of nylon 6-clay hybrid by montmorillonite intercalated with ε-caprolactam," *J. of Polym. Sci., Part A: Polym. Chem.* 31, 983-986 (1993).

Kojima, Y., A. Usuki, M. Kawasumi, A. Okada, T. Kurauchi, O. Kamigaito, and K. Kaji, "Fine structure of nylon-6-clay hybrid," *J. of Polym. Sci., Part B: Polym. Phys.* 32, 625-630 (1994).

Kojima, Y., A. Usuki, M. Kawasumi, A. Okada, T. Kurauchi, O. Kamigaito, and K. Kaji, "Novel preferred orientation in injection-molded nylon 6-clay hybrid," *J. of Polym. Sci., Part B: Polym. Phys.* 33, 1039 (1995).

Koo, C. M., H. T. Ham, S. O. Kim, K. H. Wang, I. J. Chung, D.-C. Kim, and W.-C. Zin, "Morphology evolution and anisotropic phase formation of the maleated polyethylene-layered silicate nanocomposites," *Macromolecules* 35, 5116-5122 (2002).

Koo, C. M., M. J. Kim, M. H. Choi, S. O. Kim, and I. J. Chung, "Mechanical and rheological properties of the maleated polypropylene-layered silicate nanocomposites with different morphology," *J. Appl. Polym. Sci.* 88, 1526-1535 (2003).

Kotsilkova, R., "Rheology-structure relationship of polymer/layered silicate hybrids," *Mechanics Time-Dependent Mat.* 6, 283-300 (2002).

Krall, A. H., and D. A. Weitz, "Internal Dynamics and Elasticity of Fractal Colloidal Gels," *Phys. Rev. Lett.* 80, 778-781 (1998).

Krishnamoorti, R., and E. P. Giannelis, "Rheology of end-tethered polymer layered silicate nanocomposites," *Macromolecules* 30, 4097-4102 (1997).

Krishnamoorti, R., and E. P. Giannelis, "Strain hardening in model polymer brushes under shear," *Langmuir* 17, 1448-1452 (2001).

Krishnamoorti, R., J. Ren, and A. S. Silva, "Shear response of layered silicate nanocomposites," *J. Chem. Phys.* 114, 4968-4973 (2001).

Krishnamoorti, R., and R. A. Vaia, *Polymer Nanocomposites: Synthesis, Characterization, and Modeling* (American Chemical Society,Washington, 2002).

Krishnamoorti, R., and K. Yurekli, "Rheology of polymer layered silicate nanocomposites," *Curr. Opin. Colloid Interface Sci.* 6, 464-470 (2001).

Kroon, M., W. L. Vos, and G. H. Wegdam, "Structure and formation of a gel of colloidal disks," *Phys. Rev. E* 57, 1962-1970 (1998).

Kwak, S.-Y., and K. S. Oh, "Effect of thermal history on structural changes in melt-intercalated poly (ε-caprolactone)/organoclay nanocomposites investigated by dynamic viscoelastic relaxation measurements," *Macromol. Mater. Eng.* 288, 503-508 (2003).

Lagaly, G., "Interactions of alkylamines with different types of layered compounds," *Solid State Ionics* 22, 43-51 (1986).

Lan, T., P. D. Karivatna, and T. J. Pinnavaia, "Mechanism of clay tactoid exfoliation in epoxy-clay nanocomposites," *Chem. Mater.* 2, 2144-2150 (1995).

Langat, J., S. Bellayer, P. Hudrlik, A. Hudrlik, P. H. Maupin, S. J. W. Gilman, and D. Raghavan, "Synthesis of imidazolium salts and their application in epoxy montmorillonite nanocomposites," *Polymer* 47, 6698-6709 (2006).

Le Pluart, L. *Nanocomposites epoxyde/amine/montmorillonite : rôle des interactions sur la formation, la morphologie au différents niveaux d'échelle et les propriétés mécaniques des réseaux*. Institut national des sciences appliquées de Lyon, Lyon, 2002.

Lee, J. D., J. H. So, and S. M. Yang, "Rheological behavior and stability of concentrated silica suspensions," *J. Rheol.* 43, 1117-1140 (1999).

Lee, K. M., and C. D. Han, "Effect of hydrogen bonding on the rheology of polycarbonate/organoclay nanocomposites," *Polymer* 44, 4573-4588 (2003).

Lele, A., M. Mackley, C. Ramesh, and G. Galgali, "In situ rheo-x-ray investigation of flow-induced orientation in layered silicate-syndiotactic polypropylene nanocomposite melt," *J. Rheol.* 46, 1091-1110 (2002).

Lepoittevin, B., M. Devalckenaere, N. Pantoustier, M. Alexandre, D. Kubies, C. Calberg, R. Jerome, and P. Dubois, "Poly (ε-caprolactone)/clay nanocomposites prepared by melt intercalation: mechanical, thermal and rheological properties," *Polymer* 43, 4017-4023 (2002).

Letwimolnun, W., B. Vergnes, G. Ausias, and P. J. Carreau, "Stress overshoots of organoclay nanocomposites in transient shear flow," *J. Non-Newtonian Fluid Mech.* 141, 167-179 (2007).

Li, J., C. Zhou, G. Wang, and D. Zhao, "Study on rheological behavior of polypropylene/clay nanocomposites," *J. Appl. Polym. Sci.* 89, 3609-3617 (2003).

Lim, S. T., C. H. Lee, H. J. Choi, and M. S. Jhon, "Solidlike transition of melt-intercalated biodegradable polymer/clay nanocomposites," J. *of Polym. Sci., Part B: Polym. Phys.* 41, 2052-2061 (2003).

Lim, Y. T., and O. O. Park, "Rheological evidence for the microstructure of intercalated polymer/layered silicate nanocomposites," *Macromol. Rapid Commun.* 21, 231-235 (2000).

Lim, Y. T., and O. O. Park, "Phase morphology and rheological behavior of polymer/layered silicate nanocomposites," *Rheol. Acta* 40, 220-229 (2001).

Lin-Gibson, S., J. A. Pathak, E. A. Grulke, H. Wang, and E. K. Hobbie, "Elastic Flow Instability in Nanotube Suspensions," *Phys. Rev. Lett.* 92, 048302 (2004).

Lin, Y. C., G. H. Koenderink, F. C. MacKintosh, and D. A. Weitz, "Viscoelastic Properties of Microtubule Networks," *Macromolecules* 40, 7714-7720 (2007).

Liu, L., Z. Qi, and X. Zhu, "Studies on nylon 6/clay nanocomposites by melt-intercalation process," *J. Appl. Polym. Sci.* 71, 1133-1138 (1999).

Liu, T., W. C. Tjiu, C. He, S. S. Na, and T.-S. Chung, "A processing-induced clay dispersion and its effect on the structure and properties of polyamide 6," *Polymer Int.* 53, 392-399 (2004).

Lyatskaya, Y., and A. C. Balazs, "Modeling the phase behavior of polymer-clay composites," *Macromolecules* 31, 6676-6680 (1998).

Ma, A., M. Mackley, and S. Rahatekar, "Experimental observation on the flow-induced assembly of Carbon nanotube suspensions to form helical bands," *Rheol. Acta* 46, 979-987 (2007).

Mackay, M. E., C. H. Liang, and P. J. Halley, "Instrument effects on stress jump measurements," *Rheol. Acta* 31, 481-489 (1992).

Maiti, P., "Influence of miscibility on viscoelasticity, structure, and intercalation of oligo-poly(caprolactone)/layered silicate nanocomposites," *Langmuir* 19, 5502-5510 (2003).

Mason, T. G., and D. A. Weitz, "Linear Viscoelasticity of Colloidal Hard Sphere Suspensions near the Glass Transition," *Phys. Rev. Lett.* 75, 2770-2773 (1995).

Medellin-Rodriguez, F. J., C. Burger, B. S. Hsiao, B. Chu, R. Vaia, and S. Phillips, "Time-resolved shear behavior of end-tethered Nylon 6-clay nanocomposites followed by non-isothermal crystallization," *Polymer* 42, 9015-9023 (2001).

Meincke, O., B. Hoffmann, C. Dietrich, and C. Friedrich, "Viscoelastic properties of polystyrene nanocomposites based on layered silicates," *Macromol. Chem. Phys.* 204, 823-830 (2003).

Meissner, J., and J. Hostettler, "New elongational rheometer for polymer melts and other highly viscoelastic liquids," *Proceedings of the Eleventh International Congress on Rheology - Theoretical and Applied Rheology*, Aug 17-21 1992

Mellema, M., J. W. M. Heesakkers, J. H. J. van Opheusden, and T. van Vliet, "Structure and Scaling Behavior of Aging Rennet-Induced Casein Gels Examined by Confocal Microscopy and Permeametry," *Langmuir* 16, 6847-6854 (2000).

Mering, J., and J. Pedro, "Discussion à propos des critères de classification des phyllosilicates 2/1," *Bull. groupe français argiles* 21, 1-30 (1969).

Mewis, J., "Thixotropy-a general review," *J. Non-Newtonian Fluid Mech.* 6, 1-20 (1979).

Mewis, J., and G. Schoukens, "Mechanical spectroscopy of colloidal dispersions," *Faraday Discuss. Chem. Soc.* 65, 58-64 (1978).

Michot, L. J., I. Bihannic, K. Porsch, S. Maddi, C. Baravian, J. Mougel, and P. Levitz, "Phase diagrams of wyoming Na-montmorillonite clay. Influence of particle anisotropy," *Langmuir* 20, 10829-10837 (2004).

Mitchell, C. A., and R. Krishnamoorti, "Rheological properties of diblock copolymer/layered-silicate nanocomposites," *J. Polym. Sci.* 40, 1434-1443 (2002).

Moan, M., T. Aubry, and F. Bossard, "Nonlinear behavior of very concentrated suspensions of plate-like kaolin particles in shear flow," *J. Rheol.* 47, 1493-1504 (2003).

Mobuchon, C., P. Carreau, and M.-C. Heuzey, "Effect of flow history on the structure of a non-polar polymer/clay nanocomposite model system," *Rheol. Acta* 46, 1045-1056 (2007).

Mohraz, A., and M. J. Solomon, "Orientation and rupture of fractal colloidal gels during start-up of steady shear flow," *J. Rheol.* 49, 657-681 (2005).

Moldenaers, P., and J. Mewis, "On the nature of viscoelasticity in polymeric liquid crystals," *J. Rheol.* 37, 367-380 (1993).

Montesi, A., A. A. Pena, and M. Pasquali, "Vorticity alignment and negative normal stresses in sheared attractive emulsions," *Phys. Rev. Lett.* 92, 058303 (2004).

Morgan, A. B., and J. W. Gilman, "Characterization of polymer-layered silicate (clay) nanocomposites by transmission electron microscopy and X-ray diffraction: A comparative study," *J. Appl. Polym. Sci.* 87, 1329-1338 (2003).

Morvan, M., D. Espinat, J. Lambard, and T. Zemb, "Ultrasmall-Angle and Small-Angle X-Ray-Scattering of Smectite Clay Suspensions," *Colloids and Surf. A* 82, 193-203 (1994).

Moses, E., T. Kume, and T. Hashimoto, "Shear Microscopy of the Butterfly Pattern in Polymer Mixtures," *Phys. Rev. Lett.* 72, 2037-2040 (1994).

Mourchid, A., A. Delville, J. Lambard, E. Lecolier, and P. Levitz, "Phase-Diagram of Colloidal Dispersions of Anisotropic Charged-Particles - Equilibrium Properties, Structure, and Rheology of Laponite Suspensions," *Langmuir* 11, 1942-1950 (1995).

Okada, A., M. Kawasumi, T. Kurauchi, and O. Kamigaito, *Synthesis and characterization of a nylon 6-clay hybrid* (Div of Polymer Chemistry Inc, Newark, NJ, USA, New Orleans, LA, USA, 1987).

Okamoto, M., P. H. Nam, P. Maiti, T. Kotaka, N. Hasegawa, and A. Usuki, "A house of cards structure in polypropylen/clay nanocomposites under elongational flow," *Nano Letters* 1, 295-298 (2001).

Onsager, L., "The effects of shapes on the interaction of colloidal particles," *Ann. N.Y. Acad. Sci.* 51, 627 (1949).

Page, A., P. J. Carreau, M. Moan, and M. C. Heuzey, "Rheological behavior of coating colors: Influence of thickener," *Can. J. of Chem. Eng.* 80, 1181-1188 (2002).

Pantina, J. P., and E. M. Furst, "Colloidal Aggregate Micromechanics in the Presence of Divalent Ions," *Langmuir* 22, 5282-5288 (2006).

Patel, H. A., R. S. Somani, H. C. Bajaj, and R. V. Jasra, "Nanoclays for polymer nanocomposites, paints, inks, greases and cosmetics formulations, drug delivery vehicle and waste water treatment," *Bulletin of Mater. Sci.* 29, 133-145 (2006).

Pawley, J. B., *Handbook of biological confocal microscopy* (Springer,Madison, 2006).

Pellens, L., J. Vermant, and J. Mewis, "Deviations from the stress-optical rule in telechelic associative polymer solutions," *Macromolecules* 38, 1911-1918 (2005).

Philipse, A. P., and A. Vrij, "Preparation and properties of nonaqueous model dispersions of chemically modified, charged silica spheres," *J. Colloid and Interface Sci.* 128, 121-136 (1989).

Piau, J. M., M. Dorget, and J. F. Palierne, "Shear elasticity and yield stress of silica-silicone physical gels: Fractal approach," *J. Rheol.* 43, 305-314 (1999).

Pignon, F., A. Magnin, and J.-M. Piau, "Thixotropic colloidal suspensions and flow curves with minimum: identification of flow regimes and rheometric consequences," *J. Rheol.* 40, 573-587 (1996).

Pignon, F., A. Magnin, and J.-M. Piau, "Thixotropic behavior of clay dispersions: combinations of scattering and rheometric techniques," *J. Rheol.* 42, 1349-1373 (1998).

Pignon, F., A. Magnin, J.-M. Piau, B. Cabane, P. Lindner, and O. Diat, "Yield stress thixotropic clay suspension: investigations of structure by light, neutron, and x-ray scattering," *Phys. Rev. E* 56, 3281-3289 (1997a).

Pignon, F., A. Magnin, and J. M. Piau, "Butterfly light scattering pattern and rheology of a sheared thixotropic clay gel," *Phys. Rev. Lett.* 79, 4689-4692 (1997b).

Potanin, A. A., "On the Computer Simulation of the Deformation and Breakup of Colloidal Aggregates in Shear Flow," *J. Colloid and Interface Sci.* 15, 399-410 (1993).

Potanin, A. A., S. M. Shrauti, D. W. Arnold, A. M. Lane, and J. Mellema, "Testing the structure of magnetic paints with and without superimposed shear," *J. Rheol.* 41, 1337-1347 (1997).

Rahatekar, S. S., K. K. K. Koziol, S. A. Butler, J. A. Elliott, M. S. P. Shaffer, M. R. Mackley, and A. H. Windle, "Optical microstructure and viscosity enhancement for an epoxy resin matrix containing multiwall carbon nanotubes," *J. Rheol.* 50, 599-610 (2006).

Ramsay, J. D. F., and P. Lindner, "Small-Angle Neutron-Scattering Investigations of the Structure of Thixotropic Dispersions of Smectite Clay Colloids," *J. Chem. Soc.-Farad. Trans.* 89, 4207-4214 (1993).

Ramsay, J. D. F., S. W. Swanton, and J. Bunce, "Swelling and Dispersion of Smectite Clay Colloids - Determination of Structure by Neutron-Diffraction and Small-Angle Neutron-Scattering," *J. Chem. Soc. Faraday Trans.* 86, 3919-3926 (1990).

Ray, S. S., K. Okamoto, and M. Okamoto, "Structure-property relationship in biodegradable poly(butylene succinate)/layered silicate nanocomposites," *Macromolecules* 36, 2355-2367 (2003).

Ray, S. S., and M. Okamoto, "Polymer/layered silicate nanocomposites: A review from preparation to processing," *Prog. Polym. Sci.* 28, 1539-1641 (2003).

Ren, J., B. F. Casanueva, C. A. Mitchell, and R. Krishnamoorti, "Disorientation kinetics of aligned polymer layered silicate nanocomposites," *Macromolecules* 36, 4188-4194 (2003).

Ren, J., and R. Krishnamoorti, "Nonlinear viscoelastic properties of layered-silicate-based intercalated nanocomposites," *Macromolecules* 36, 4443-4451 (2003).

Ren, J., A. S. Silva, and R. Krishnamoorti, "Linear viscoelasticity of disordered polystyrene-polyisoprene block copolymer based layered-silicate nanocomposites," *Macromolecules* 33, 3739-3746 (2000).

Rossman, F. G., and J. v. O. Carel, *Colloid and surface properties of clays and related minerals* (Marcel Dekker,New York, 2002).

Rueb, C. J., and C. F. Zukoski, "Viscoelastic properties of colloidal gels," *J. Rheol.* 41, 197-218 (1997).

Russel, W. B., *The dynamics of colloidal systems* (University of Wisconsin Press,Madison, 1987).

Russel, W. B., D. A. Saville, and W. R. Schowalter, *Colloidal dispersions* (Cambridge University Press,cambridge, 1989).

Ruzicka, B., L. Zulian, and G. Ruocco, "More on the phase diagram of laponite," *Langmuir* 22, 1106-1111 (2006).

Saint-Michel, F., F. Pignon, and A. Magnin, "Fractal behavior and scaling law of hydrophobic silica in polyol," *J. Colloid and Interface Sci.* 267, 314-319 (2003).

Segrè, P. N., V. Prasad, A. B. Schofield, and D. A. Weitz, "Glasslike Kinetic Arrest at the Colloidal-Gelation Transition," *Phys. Rev. E* 86, 6042-6045 (2001).

Seong, D. G., and J. R. Youn, *Rheological behavior of polymer based nanocomposites with different dispersion of nanoclays* (Seoul, Korea, 2004).

Sepehr, M., P. J. Carreau, M. Moan, and G. Ausias, "Rheological properties of short fiber model suspensions," *J. Rheol.* 48, 1023-1048 (2004).

Shalkevich, A., A. Stradner, S. K. Bhat, F. Muller, and P. Schurtenberger, "Cluster, glass, and gel formation and viscoelastic phase separation in aqueous clay suspensions," *Langmuir* 23, 3570-3580 (2007).

Shih, W.-H., W. Y. Shih, S.-I. Kim, J. Liu, and I. A. Aksay, "Scaling behavior of the elastic properties of colloidal gels," *Phys. Rev. A* 42, 4772-4779 (1990).

Simmons, J. M., "A servo-controlled rheometer for measurement of the dynamic modulus of viscoelastic liquids," *J. Sci. Inst.* 43, 887-892 (1966).

Solomon, M. J., A. S. Almusallam, K. F. Seefeldt, A. Somwangthanaroj, and P. Varadan, "Rheology of polypropylene/clay hybrid materials," *Macromolecules* 34, 1864-1872 (2001).

Sonntag, R. C., and W. B. Russel, "Structure and breakup of flocs subjected to fluid stresses: I. Shear experiments," *J. Colloid and Interface Sci.* 113, 399-413 (1986).

Sonntag, R. C., and W. B. Russel, "Structure and breakup of flocs subjected to fluid stresses: II. Theory," *J. Colloid and Interface Sci.* 115, 378-389 (1987).

Tanaka, H., S. Jabbari-Farouji, J. Meunier, and D. Bonn, "Kinetics of ergodic-to-nonergodic transitions in charged colloidal suspensions: Aging and gelation," *Phys. Rev. E* 71, 021402 (2005).

Tanaka, H., J. Meunier, and D. Bonn, "Nonergodic states of charged colloidal suspensions: Repulsive and attractive glasses and gels," *Phys. Rev. E* 69, 031404 (2004).

Tanoue, S., L. A. Utracki, A. Garcia-Rejon, P. Sammut, M.-T. Ton-That, I. Pesneau, M. R. Kamal, and J. Lyngaae-Jorgensen, "Melt compounding of different grades of polystyrene with organoclay. Part 2: rheological properties," *Polym. Eng. Sci.* 44, 1061-1076 (2004).

Thompson, D. W., and J. T. Butterworth, "The nature of laponite and its aqueous dispersions," *J. Colloid and Interface Sci.* 151, 236-243 (1992).

Tombacz, E., and M. Szekeres, "Colloidal behavior of aqueous montmorillonite suspensions: the specific role of pH in the presence of indifferent electrolytes," *Appl. Clay Sci.* 27, 75-94 (2004).

Trappe, V., V. Prasad, L. Cipelletti, P. N. Segre, and D. A. Weitz, "Jamming phase diagram for attractive particles," *Nature* 411, 772-775 (2001).

Trappe, V., and P. Sandkuhler, "Colloidal gels--low-density disordered solid-like states," *Curr. Opin. Colloid Interface Sci.* 8, 494-500 (2004).

Trappe, V., and D. A. Weitz, "Scaling of the viscoelasticity of weakly attractive particles," *Phys. Rev. Lett.* 85, 449-452 (2000).

Vaia, R. A., and E. P. Giannelis, "Lattice model of polymer melt intercalation in organically-modified layered silicates," *Macromolecules* 30, 7990-7999 (1997a).

Vaia, R. A., and E. P. Giannelis, "Polymer melt intercalation in organically-modified layered silicates: Model predictions and experiment," *Macromolecules* 30, 8000-8009 (1997b).

Vaia, R. A., and W. Liu, "X-ray powder diffraction of polymer/layered silicate nanocomposites: Model and practice," *J. of Polym. Sci., Part B: Polym. Phys.* 40, 1590-1600 (2002).

van de Ven, T. G. M., *Colloidal hydrodynamics* (Academic Press,London, 1989).

Varadan, P., and M. J. Solomon, "Shear-induced microstructural evolution of thermoreversible colloidal gel," *Langmuir* 17, 2918-2929 (2001).

Varlot, K., E. Reynaud, M. H. Kloppfer, G. Vigier, and J. Varlet, "Clay-reinforced polyamide: Preferential orientation of the montmorillonite sheets and the polyamide crystalline lamellae," *J. of Polym. Sci., Part B: Polym. Phys.* 39, 1360-1370 (2001).

Verduin, H., B. J. deGans, and J. K. G. Dhont, "Shear induced structural changes in a gel-forming suspension studied by light scattering and rheology," *Langmuir* 12, 2947-2955 (1996).

Vermant, J., S. Ceccia, M. K. Dolgovskij, P. L. Maffettone, and C. W. Macosko, "Quantifying dispersion of layered nanocomposites via melt rheology," *J. Rheol.* 51, 429-450 (2007).

Vermant, J., P. Moldenaers, J. Mewis, M. Ellis, and R. Garritano, "Orthogonal superposition measurements using a rheometer equipped with a force rebalanced transducer," *Rev. Sci. Intruments* 68, 4090-4096 (1997).

Vermant, J., and M. J. Solomon, "Flow-induced structure in colloidal suspensions," *J. Phys.: Condens. Matter* 17, R187-R216 (2005).

Vermant, J., L. Walker, P. Moldenaers, and J. Mewis, "Orthogonal versus parallel superposition measurements," *J. Non-Newt. Fluid Mech.* 79, 173-189 (1998).

Wagener, R., and T. J. G. Reisinger, "A rheological method to compare the degree of exfoliation of nanocomposites," *Polymer* 44, 7513-7518 (2003).

Wagner, N. J., G. G. Fuller, and W. B. Russel, "The dichroism and birefringence of a hard-sphere suspension under shear," *J. Chem. Phys.* 89, 1580-1587 (1988).

Walker, L. M., J. Vermant, P. Moldenaers, and J. Mewis, "Orthogonal and parallel superposition measurements on lyotropic liquid crystalline polymers," *Rheol. Acta* 39, 26-37 (2000).

Wang, K. H., M. H. Choi, C. M. Koo, M. Xu, I. J. Chung, M. C. Jang, S. W. Choi, and H. H. Song, "Morphology and physical properties of polyethylene/silicate nanocomposite prepared by melt intercalation," *J. of Polym. Sci., Part B: Polym. Phys.* 40, 1454-1463 (2002).

Wilhelm, M., "Fourier-transform rheology," *Macromol. Mater. Eng.* 287, 85-105 (2002).

Wilhelm, M., D. Maring, and H.-W. Spiess, "Fourier-transform rheology," *Rheol. Acta* 37, 399-405 (1998).

Wilhelm, M., P. Reinheimer, and M. Ortseifer, "High sensitivity Fourier-transform rheology," *Rheol. Acta* 38, 349-356 (1999).

Wu, H., and M. Morbidelli, "Model relating structure of colloidal gels to their elastic properties," *Langmuir* 17, 1030-1036 (2001).

Wyss, H. M., K. Miyazaki, J. Mattsson, Z. B. Hu, D. R. Reichman, and D. A. Weitz, "Strain-rate frequency superposition: A rheological probe of structural relaxation in soft materials," *Phys. Rev. Lett.* 98, (2007).

Yoonessi, M., H. Toghiani, T. L. Daulton, J.-S. Lin, and C. U. Pittman Jr, "Clay delamination in clay/poly(dicyclopentadiene) nanocomposites quantified by small angle neutron scattering and high-resolution transmission electron microscopy," *Macromolecules* 38, 818-831 (2005).

Yoonessi, M., H. Toghiani, W. L. Kingery, and C. U. Pittman, "Preparation, characterization, and properties of exfoliated/delaminated organically modified clay/dicyclopentadiene resin nanocomposites," *Macromolecules* 37, 2511-2518 (2004).

Yziquel, F., and P. J. Carreau, "Non-linear viscoelastic behavior of fumed silica suspensions," *Rheol. Acta* 38, 14-25 (1999).

Yziquel, F., P. J. Carreau, M. Moan, and P. A. Tanguy, "Rheological modeling of concentrated colloidal suspensions," *J. Non-Newt. Fluid Mech.* 86, 133-155 (1999).

Zaccarelli, E., G. Foffi, K. A. Dawson, F. Sciortino, and P. Tartaglia, "Mechanical properties of a model of attractive colloidal solutions," *Phys. Rev. E* 63, 031501 (2001).

Zeegers, J., D. Ende, C. Blom, E. G. Altena, G. J. Beukema, and J. Mellema, "A sensitive dynamic viscometer for measuring the complex shear modulus in a steady shear flow using the method of orthogonal superposition," *Rheol. Acta* 34, 606-621 (1995).

Zhong, Y., and S.-Q. Wang, "Exfoliation and yield behavior in nanodispersions of organically modified montmorillonite clay," *J. Rheol.* 47, 483-495 (2003).

Zhulina, E., C. Singh, and A. C. Balazs, "Attraction between surfaces in a polymer melt containing telechelic chains: Guidelines for controlling the surface separation in intercalated polymer-clay composites," *Langmuir* 15, 3935-3943 (1999).

ANNEXE A – MODÈLE STRUCTURAL

Au regard du portrait rhéologique des suspensions non-aqueuses de phyllosilicate dressé lors de cette étude, un modèle phénoménologique inspiré des travaux d'Yziquel *et al.* (1999) est proposé. L'objectif premier lors de sa formulation est d'être à même de prendre en compte l'influence de l'histoire d'écoulement. Il a pour base le modèle de Jeffreys :

$$\frac{\delta}{\delta t}\left[\frac{\sigma}{G(\xi)}\right] + \frac{\sigma}{\eta(\xi)} = \left(1 + \frac{\eta_\infty}{\eta(\xi)}\right)\dot{\gamma} + \eta_\infty \frac{\delta}{\delta t}\left(\frac{\dot{\gamma}}{G(\xi)}\right) \quad \text{(A.1)}$$

avec η_∞ la viscosité en l'absence de structure, et G le module élastique et η la viscosité définis selon les travaux d'Yziquel *et al.* (1999) :

$$G(\xi) = G_0\xi + G_\infty \quad \text{(A.2)}$$

$$\eta(\xi) = \frac{\eta_0}{f(\xi)} \quad \text{(A.3)}$$

avec η_0 une viscosité caractéristique, G_∞ le module élastique en l'absence de structure, et $G_0 + G_\infty$ le modules élastique pour le plus haut niveau de structure. Une nouvelle fonction de structure f est posée de façon à obtenir tout comme Yziquel *et al.* (1999) une viscosité selon une loi de puissance avec une viscosité limite aux hauts taux de cisaillement en régime permanent :

$$f(\xi) = \left[\left(\frac{1}{\xi} - 1\right)\right]^{\frac{(1-n)}{(1+n)-1/w}} \quad \text{(A.4)}$$

avec n l'indice de la loi de puissance, et w un indice lié à l'exposant m de la dépendance de ξ_0 avec $\dot{\gamma}_i$ donnée à la figure 5.14.

Conceptuellement, on différencie l'évolution de structure à l'échelle microscopique induite par cisaillement de celle présente aux plus petites échelles. Le paramètre de structure, ξ, est pour cela dissocié en une contribution dite microscopique, ξ_m, et une autre dite locale, ξ_l :

$$\xi = \xi_m + \xi_l \tag{A.5}$$

Une équation cinétique est écrite pour chacune des contributions :

$$\frac{\partial \xi_m}{\partial t} = k_1(1-\xi_m)|\dot{\gamma}|^{\frac{1}{w}}\lambda_0^{\frac{1-w}{w}} - k_2\frac{\lambda_0}{\eta_0}\xi_m|\sigma{:}\dot{\gamma}| \tag{A.6}$$

$$\frac{\partial \xi_l}{\partial t} = \frac{k_3}{\lambda_0}\left(\frac{(1-\xi_m)}{\alpha} - \xi_l\right) - k_4\frac{\lambda_0}{\eta_0}\xi_l|\sigma{:}\dot{\gamma}| \tag{A.7}$$

avec λ_0 un temps caractéristique, et k_1, k_2, k_3, k_4 des constantes cinétiques. La perte de structure due aux forces hydrodynamiques est supposée fonction du taux d'énergie dissipée (Yziquel *et al.* 1999). Elle peut également être considérée dépendante de la vitesse de cisaillement. La fonction de structure f et les équations cinétiques s'écrivent alors respectivement de la façon suivante :

$$f(\xi) = \left[\left(\frac{1}{\xi} - 1\right)\right]^{\frac{(1-n)}{(2-w)}} \tag{A.8}$$

$$\frac{\partial \xi_m}{\partial t} = k_1(1-\xi_m)|\dot{\gamma}|^{\frac{1}{w}}\lambda_0^{\frac{1-w}{w}} - \frac{k_2}{\lambda_0}\xi_m(\lambda_0\dot{\gamma})^2 \tag{A.9}$$

$$\frac{\partial \xi_l}{\partial t} = \frac{k_3}{\lambda_0}\left(\frac{(1-\xi_m)}{\alpha} - \xi_l\right) - \frac{k_4}{\lambda_0}\xi_m(\lambda_0\dot{\gamma})^2 \tag{A.10}$$

Finalement, elle est supposée fonction des contraintes normales, et imposer la formulation suivante :

$$f(\xi) = \left[\left(\frac{1}{\xi} - 1\right)\sqrt{(G_0\xi + G_\infty)}\right]^{\frac{w(1-n)}{2(w-1)}} \tag{A.11}$$

$$\frac{\partial \xi_m}{\partial t} = k_1(1-\xi_m)|\dot{\gamma}|^{\frac{1}{w}}\lambda_0^{\frac{1-w}{w}} - \frac{k_2}{\lambda_0}\xi_m\sqrt{\frac{|I_\sigma|}{2G(\xi)}} \quad \text{(A.12)}$$

$$\frac{\partial \xi_l}{\partial t} = \frac{k_3}{\lambda_0}\left(\frac{(1-\xi_m)}{\alpha} - \xi_l\right) - \frac{k_4}{\lambda_0}\xi_m\sqrt{\frac{|I_\sigma|}{2G(\xi)}} \quad \text{(A.13)}$$

Dans tous les cas, ξ_m représente l'agrégation induite par cisaillement, et il est directement lié à ξ_0. ξ_l quant à lui permet de tenir compte de la thixotropie des suspensions, et ainsi des réarrangements à l'échelle nanoscopique responsables de l'évolution de *G'* suite à un pré-cisaillement. Le modèle se réduit à celui d'Yziquel *et al.* (1999) en l'absence de structuration à l'échelle microscopique.

La réponse du modèle selon le taux d'énergie dissipée lors d'un cisaillement en régime permanent est illustrée à la Figure A.1 avec les paramètres donnés à la Table A.1. Le paramètre de structure est donné sous écoulement (indiqué par $\dot{\gamma}$) et au repos (indiqué par $\dot{\gamma}_i$). Il suit bien qualitativement l'évolution du module élastique donnée à la figure 5.1b.

Tableau A.1 : Paramètres du modèle considérés à la Figure A.1

G'_0 (Pa)	G'_∞ (Pa)	k_1	k_2	k_3	k_4	λ_0	η_∞ (Pa.s)	n	w Pa.s^n	α
0.9	0.1	1	1	1	1	1	1	0	2	4

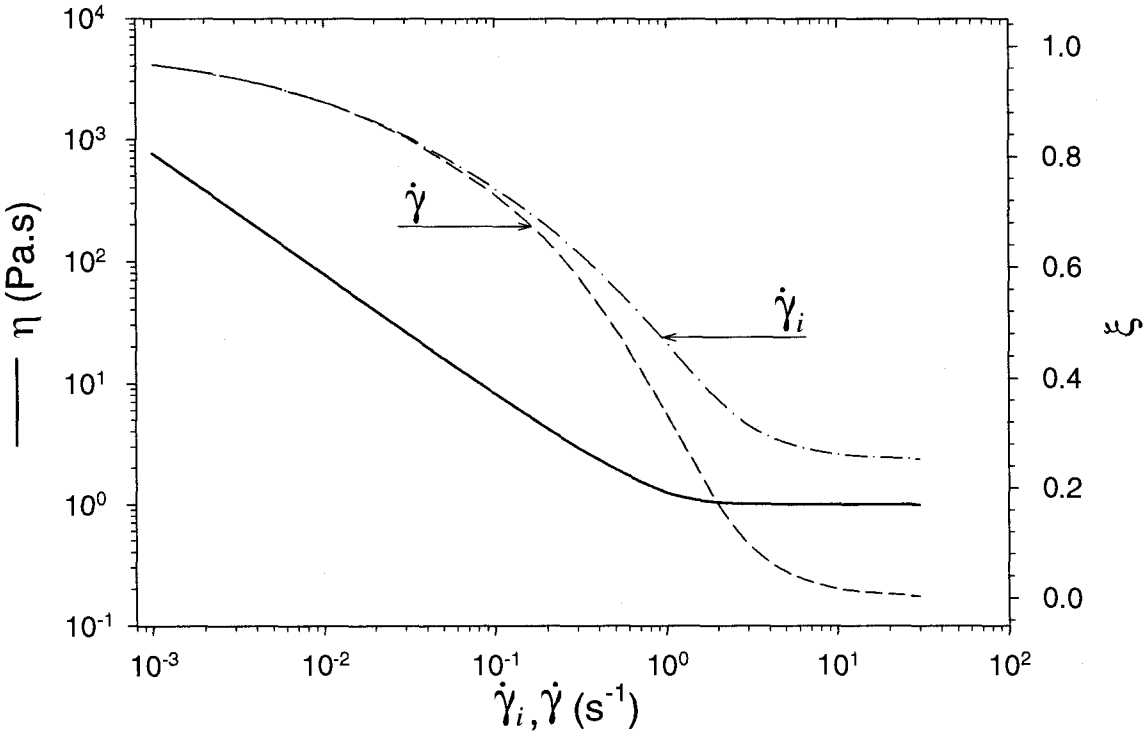

Figure A.1: Viscosité η en fonction du taux de cisaillement $\dot{\gamma}$, et fonction de structure ξ en fonction du taux de cisaillement $\dot{\gamma}$ et du taux de pré-cisaillement $\dot{\gamma}_i$ (lignes discontinues).